A hybrid MoM/PO technique with large element PO

by

Siyanda Nazo

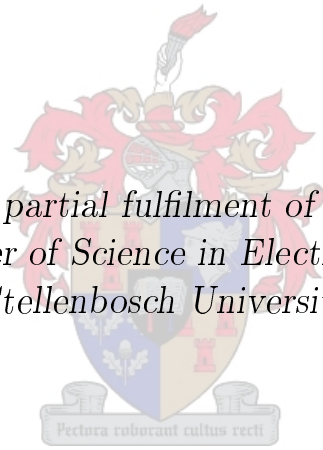

Thesis presented in partial fulfilment of the requirements for the degree of Master of Science in Electronic Engineering at Stellenbosch University

Department of Electrical and Electronic Engineering,
University of Stellenbosch,
Private Bag X1, Matieland 7602, South Africa.

Supervisor: Prof. D.B. Davidson, Mr. J.C. Smit

March 2012

Declaration

By submitting this thesis electronically, I declare that the entirety of the work contained therein is my own, original work, that I am the owner of the copyright thereof (unless to the extent explicitly otherwise stated) and that I have not previously in its entirety or in part submitted it for obtaining any qualification.

Signature: .....
S. Nazo

Date: 2012/03/08 .....

Abstract

A hybrid MoM/PO technique with large element PO

S. Nazo

Department of Electrical and Electronic Engineering,
University of Stellenbosch,
Private Bag X1, Matieland 7602, South Africa.

Thesis: MScEng (Elec)

March 2012

Radar Cross Section (RCS) is an important parameter in radar engineering. Often, electrically large structures are of interest in RCS analysis due to the high operating frequencies of radar systems. Simulation of these problems can be more efficient than measurement due to the cost associated with measurement. The Method of Moments/Physical Optics (MoM/PO) hybrid method combines the advantages of the MoM and PO, making it suited to solving electrically large problems that may contain some small complex detail. The requirement for high meshing resolution when analysing some electromagnetic problems, however, significantly increases memory requirements. As a result, the hybrid MoM/PO becomes computationally expensive for electrically large problems. In this work, a linear phase term is introduced into the RWG basis function formulation of the MoM/PO hybrid. The addition of the linear phase term allows the use of large triangular mesh elements in the PO region, resulting in the analysis of electrically large problems. The benefit of this formulation is that it allows a reduction in computational cost whilst maintaining the accuracy of the hybrid MoM/PO. This improved hybrid is tested on various planar test cases and results show that it attains the same level of accuracy as the original MoM/PO hybrid.

Uittreksel

("A hybrid MoM/PO technique with large element PO")

S. Nazo

Tesis: MScIng (Elec)

Maart 2012

Radardeursnit is 'n belangrike parameter in radaringenieurswese. As gevolg van die hoë frekwensies wat deur baie radarstelsels gebruik word, is elektries-groot probleme dikwels van belang in die berekening van die radardeursnit van teikens. Die modellering en berekening van die radardeursnit van teikens kan meer kostedoeltreffend as metings wees, as gevolg van die beduidende koste van radardeursnitmetings. Die hibriede Moment-Metode/Fisiese-Optika tegniek kombineer die voordele van die twee tegnieke, wat dit geskik maak vir elektries-groot probleme met klein, komplekse detail. Indien die gewone benadering egter gevolg word om 'n hoë resolusie faset-model te gebruik, bly dit berekeningsintensief met groot rekenaar geheuevereistes vir elektries-groot probleme. In hierdie studie word 'n lineêre fase term ingesluit in die formulering van die Rao-Wilton-Glisson (RWG) basisfunksies vorm van die hibriede Moment-Metode/Fisiese-Optika tegniek. Die toevoeging van die lineêre fase term maak dit moontlik om groot driehoekfasette in die Fisiese-Optika gebied te gebruik, wat beteken dat elektries-groot probleme makliker opgelos kan word. Die voordeel van hierdie nuwe formulering is dat die berekeningslas en -tyd verminder word terwyl die akkuraatheid van die oorspronklike hibriede Moment-Metode/Fisiese-Optika tegniek behou word. Hierdie verbeterde hibriede tegniek word getoets aan die hand van verskeie platvlak toetsgevalle en die resultate dui daarop dat die akkuraatheid vergelykbaar is met die van die oorspronklike hibriede Moment-Metode/Fisiese-Optika tegniek.

Acknowledgements

I would like to acknowledge and thank the people who contributed to this work.

Firstly, I would like to thank my supervisors Prof. David B. Davidson (Stellenbosch University) and Mr. Johan C. Smit (CSIR) for their continued guidance and support throughout my work. Without them, this work would not have been possible. I would also like to thank Evan Lezar, Renier Marchand and the rest of the CEMAGG group at Stellenbosch University for the support they offered me throughout this work.

To the team at EMSS, thank you for your support when I was stuck trying to make sense of some of my results.

To the CSIR Radar Applications team, thank you for the generous assistance while working to finish this thesis.

To my family, thank you for your constant love and never-ending support throughout my life. To Kgala, thank you as well for your support, patience and motivation, especially during those times I couldn't see the light.

Lastly, I would like to say *Enkosi* to all who contributed in making this thesis a success.

Dedications

This thesis is dedicated to the memory of my late father, Vuyani Nazo.

Contents

List of Figures

List of Tables

Nomenclature

Constants

c =	2.99×10^8	[m/s]

Variables

$\hat{x}$	Coordinate	[m]
σ	Radar Cross Section	[dBsm]
θ	Rotation angle	[deg]
J	Current Density	[A/m]
k	Vector wave number	[rad/m]

List of Abbreviations

AMMM	Adaptive Multiscale Method of Moments
APE	Asymptotic Phase Extraction
AIM	Adaptive Integral Method
EFIE	Electric Field Integral Equation
FEM	Finite Elements
GO	Geometric Optics
GTD	Geometric Theory of Diffraction
LP	Linear Phase
MFIE	Magnetic Field Integral Equation
MoM	Method of Moments
PO	Physical Optics
PTD	Physical Theory of Diffraction
RCS	Radar Cross Section
RWG	Rao Wilton Glisson
STD	Spectral Theory of Diffraction

Chapter 1

Introduction

Radar Cross Section (RCS) is a parameter that indicates the EM reflectivity/backscatter of an object. This is an important parameter in the design of radar systems. The RCS of electrically large structures is of particular interest in radar because radar systems, specifically tracking radars, operate at high frequencies. This is the case due to the high resolution and accuracy levels required of tracking radars. Often, it is desirable to predict the RCS of objects of interest. This can be achieved through RCS measurement or simulation using RCS prediction software. The advantage of measurement is that accurate results are obtained. The disadvantage of this process, however, is that it can be expensive and/or impractical, especially when complete coverage of the scattering pattern of an object is required. Simulation provides a cost effective and more flexible alternative for obtaining acceptable results for many applications.

Electromagnetic scattering problems can be divided into approximately three categories [1]:

- In the low frequency region, the object is significantly smaller than a wavelength and the coupling between all parts of the body should be taken into consideration.
- In the resonant region, the object is between 1λ and 10λ in size and all parts of the body interact with each other.
- In the high frequency region, the total size of the object is greater than 10λ in size (electrically large) and the scattering mechanisms are mostly highly localised. In this high frequency region, the elements of the body are independent of one another but the object can also incorporate some electrically small complex details.

The field of computational electromagnetics (CEM) incorporates those methods that approximate solutions to Maxwell's equations. Two classes of methods exist in the field of CEM, namely full wave (also known as exact methods) and asymptotic methods. The full wave methods constitute a body of well

established methods. These methods consist of integral equation (for example the Method of Moments) and differential equation methods (for example the Finite Difference Time Domain method) which approximate solutions to the integral and differential form of Maxwell's equations respectively. These methods typically subdivide the problem of interest into a grid where each element of the grid is stored in a matrix. These methods hence become computationally expensive as the electrical size of the object is increased, largely due to an increase in the frequency of the incident wave. As a result, this places increased requirements on computer storage and calculation time. As an example, if N represents the number of unknowns in a Method of Moments (MoM) implementation, the memory required to store the elements of the matrix is of order N^2. For an arbitrary geometry composed of surfaces and wires the memory requirement increases with frequency in the order of f^4.

The asymptotic methods assume an asymptotic representation of the solution in the form of a series of inverse powers of the wave number k, where typically the first term is retained. This underlying assumption inherently implies that these methods work well when the dimensions of the scatterer are large in comparison to the wavelength. These methods are invalid for electrically small objects. These methods can be divided into the field based methods (such as Geometric Optics) and current based methods (such as Physical Optics).

Modelling of electrically large structures can be complicated by the presence of an electrically small, complex detail in the structure. This can prevent the calculation of an accurate result using either the full wave or asymptotic methods independently because of the shortcomings of the methods in addressing this type of problem. The numerical methods would be limited by the large requirements placed by electrically large problems on computer memory. Similarly, the asymptotic methods would fail to obtain the solution for the electrically small complex detail. This leads to the definition of the problem to be addressed in this work.

1.1 Problem Statement

In order to solve electrically large problems with electrically small, complex detail it would be desirable to take advantage of the benefits offered by both the full wave and asymptotic methods. In this way, the full wave technique would be applied to the electrically small detail in order to obtain a rigorous solution for this portion of the problem. Similarly, the asymptotic technique would be used to obtain the solution for the electrically large part of the problem, assuming the appropriate technique is applied to this portion.

Various techniques exist that are used to solve electrically large problems with small details. Hybrid methods are widely used because these combine the advantages of full wave methods and asymptotic methods. Current based hybrid methods make use of both current based full wave and asymptotic

methods. One such hybrid technique is the Method of Moments/Physical Optics (MoM/PO). A strength of this technique is that it provides seamless hybridisation because both the Method of Moments (MoM) and Physical Optics (PO) are current based. The geometry of the problem of interest can also be modelled with surface basis functions. In this technique, one region of the body of interest is set to the MoM whilst the other is set to the PO. The coupling between the two regions is taken into account via the scattered fields as a result of the currents on the surfaces.

The hybrid MoM/PO makes use of the Rao Wilton Glisson (RWG) basis function developed in [2]. This basis function has desirable properties but means that the problem of interest has to be modelled using uniform triangular mesh elements of size $\lambda/10$, the standard MoM meshing requirement. In the PO region, the same basis functions are used and the same meshing restrictions are placed in this region. The PO region can be very large when modelled with the RWG function and this meshing requirement places additional memory requirements on computational resources to store the mesh. Various techniques have been developed by other researchers in order to address this problem. These have included iterative techniques and the development of alternative basis functions. Convergence problems are often encountered in iterative techniques and the desirable properties of the RWG function are often lost when alternative basis functions are defined.

The aim of the work presented in this dissertation is to develop a MoM/PO hybrid technique that allows the problem of interest to be modelled with a non-uniform mesh containing large mesh elements in the PO region. The technique should be in the form of a closed form equation and it should maintain the accuracy of the MoM/PO hybrid.

1.2 Approach

In order to develop a hybrid MoM/PO that utilises a non-uniform mesh, the following approach will be followed:

- Techniques presented in the literature to solve electrically large problems with small detail will be studied. The techniques most suited to this work will be identified and discussed in detail.
- The MoM/PO hybrid technique will be developed and tested with a simple example. This test will verify the validity of the technique.
- Using insights obtained from the development of the MoM/PO hybrid, the hybrid technique will be extended to produce an improved hybrid MoM/PO hybrid technique. The improved hybrid will allow the incorporation of larger triangular mesh elements in the Physical Optics region of the body of interest.

- Various test simulations will be conducted to evaluate the performance of this improved hybrid against that of the original MoM/PO hybrid. Planar surfaces will be used to model the test cases.

1.3 Significance

Various current based hybrid methods exist to solve electrically large problems with small details. These methods will be presented in the literature overview in Chapter 2. A selection of some of these hybrid techniques make use of the RWG basis function and require that the body of interest is meshed at the MoM requirement of $\lambda/10$. When RWG functions are not utilised, iterative techniques and alternative basis functions are used. The hybrid MoM/PO in [3] presents a closed form equation for the hybrid. In this work, modified RWG basis functions are used in the closed form solution equation of the MoM/PO hybrid, allowing the use of a non-uniform mesh to model geometry.

1.4 Chapter Overviews

In this chapter, an introduction to the problem addressed in this work was presented. The approach to be followed in developing a technique to solve electrically large problems with small detail was also presented. Finally, the significance of this work was discussed.

In Chapter 2, literature pertaining to the solution of electrically large problems with small detail is given. Chapter 3 presents the theoretical formulation of both the Method of Moments and Physical Optics. In Chapter 4, the development of the MoM/PO hybrid technique is presented. The mathematical theory of the extension of this hybrid to include non-uniform meshes is also presented. Chapter 5 presents numerical results obtained from simulations which show the accuracy of the developed technique. A discussion of the numerical results and applicability of the developed technique is also presented in this section. Finally, a summary of the insights gained in this work is given in Chapter 6.

Chapter 2

Literature

2.1 Introduction

Various techniques exist to approximate solutions to electromagnetic (EM) scattering from electrically large bodies. The electrical size of any body is determined using the wavelength of the incident wave. For higher frequencies of the incident wave, the wavelength will be shorter. The EM scatter of electrically large bodies is of interest to radar engineers; due to the high operating frequencies of radar systems and the requirement to predict the radar reflectivity characteristics of a wide variety of bodies [1]. Several techniques exist that consider solutions for electrically large bodies [4], [5].

The current study is concerned with techniques which are used to model the EM scattering of electrically large bodies with geometric details smaller than several wavelengths. This is important due to the fact that established high frequency asymptotic techniques are not able to encapsulate all the scattering characteristics and EM behaviour at higher frequencies for small structures. At higher frequencies, the scattering mechanisms are highly localized and elements of the body act independent of one another; at the low frequencies, long wavelengths, the electromagnetic coupling between parts of the body is strong and RCS slightly depends on shape.

Two classes of computational methods exist to solve the electromagnetic scattering of large bodies, namely full wave, low frequency, and asymptotic, high frequency, methods. The full wave techniques consist of integral equation methods and differential equation methods [6]. These methods are well established, but limited in usefulness as the electrical size of the body is increased, typically over the 10 wavelength limit. These techniques place excessive demands on computing power due to either the mesh size required to model the problem or the proportional increase in the number of unknowns. The asymptotic methods, however, work well when the dimensions of the smallest geometrical detail of the scattering structure are large in comparison to the wavelength, typically greater than 10 wavelengths [1]. The suitability of these

methods to objects of different electrical size is illustrated in Figure 2.1. These methods consist of ray based and current based methods.

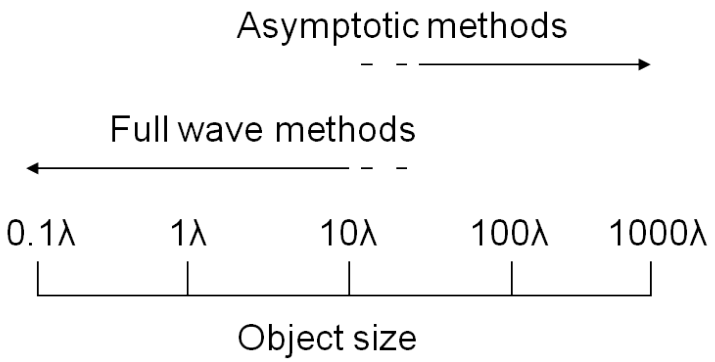

Figure 2.1: Methods applicable to EM scattering

In the following section, literature regarding the Method of Moments (MoM), a prominent full wave method, will be reviewed.

2.2 Method of Moments

The Method of Moments (MoM) is a mature full wave technique employed to solve EM field problems. This technique attempts to solve the integral equation formulations of Maxwell's equations. The representation of a linear functional equation with a linear matrix equation is a mathematical technique that has been explored since the 1800s, Galerkin developed his technique in 1915 [7]; it was not utilised because it did not have a firm mathematical basis [8]. Pocklington derived an integral equation and proposed a solution for the problem [6]. These methods were also not popular, before the advent of high-speed computing, because of the tedious computation required for their use.

Schwinger et al. [8] attempted to solve microwave electromagnetic problems at the M.I.T. Radiation laboratory with variational methods and researchers in the field started using these methods for practical problems. The 1960s saw the use of numerical methods to solve electromagnetic field problems with the advent of high computational power. Sub sectional and point-matching procedures were explored by Mei and Van Bladel for rectangular cylinders [9]. Harrington [7] recognized that Galerkin's method was equivalent to the Rayleigh-Ritz variational method and questioned whether the numerical techniques that were used at the time were not variational methods. He later coined the term "method of moments" after an extensive literature search for the most appropriate wording for the method that utilises the same expansion and testing functions. It must be noted that this is what is now known as the Galerkin method of moments formulation.

The two most important aspects of the method of moments formulation are the division of the problem into smaller elements and the approximation of the current with a basis function. A widely used technique was developed by Rao et al. to solve the scattering from arbitrary three dimensional bodies using the method of moments [2]. They developed what is now known as the Rao-Wilton-Glisson (RWG) basis function to approximate the current on a surface.

The triangular method of moments is not suited to electrically large problems, because the computer memory requirements increase in the order of n^2, with n the number of unknowns in the matrix equation. This translates into large storage requirements for a dense matrix, resulting from an electrically large problem. Researchers in the field have attempted to obtain a sparse method of moments matrix through various matrix compression techniques that are discussed in the following sections.

2.2.1 Multilevel Fast Multipole Algorithm

The Multilevel Fast Multipole Algorithm (MLFMA) for electromagnetic problems is based on the mathematical fast multipole method. The method was developed by Rokhlin for acoustic scattering problems. Early developments of this technique for electromagnetic modeling were explored by Engheta et al. in [10]. They made use of block decomposition and regrouped the far field elements into small low rank blocks. This was later extended to apply the algorithm to electrically large complex bodies in [11]. Recently, accelerations of the technique have been sought in combination with the asymptotic techniques such as the method in [12]. The technique still needs to represent the fastest variation of phase and requires the same number of unknowns as the method of moments.

2.2.2 Multiple Sweep Method of Moments

The Multiple Sweep Method of Moments (MSMM) attempts to improve the computational efficiency of the method of moments in order to find solutions for large problems. Early developments in this technique were performed by Torrungrueng et al. in [13]. In this work, the authors showed that the technique splits the body of interest and solves the currents in a recursive manner. Later, time domain interpretations of this technique were shown in [14], making it useful for wide-band problems.

2.2.3 Characteristic Basis Function Techniques

The Characteristic Basis Function (CBF) technique introduces high-level expansion functions that incorporate the physics of the problem into the basis

function. These basis functions are not bound by the conventional MoM discretisation requirement. This effectively reduces the size of the method of moments matrix. This technique was introduced by Prakash et al. in [15]. Their technique resulted in a reduced matrix, whilst still incorporating mutual coupling effects, unlike the conventional MoM. The technique has been applied to electrically large problems in [16]. The authors demonstrated the use of the characteristic basis function with the spectral domain integral equation method to produce a matrix equation that is not dependent on the size of the scatterer, but only its shape. The derivation of these basis functions follows from the PO solutions or through applications of the conventional MoM [17].

2.2.4 Adaptive Multiscale Method of Moments

The Adaptive Multiscale Method of Moments (AMMM) is suited to problems where, in the conventional method of moments, the matrix solution time exceeds the matrix fill time. The technique is presented in [18], [19], [20]. The method is a hybrid technique that combines the multi grid method with a compression technique. Su et al. demonstrated this technique to be useful for solving perfectly conducting plates in [21]. Su extended this application to arbitrary three dimensional conducting bodies in [22], using the RWG method of moments formulation.

2.2.5 Adaptive Integral Method

The Adaptive Integral Method (AIM) attempts to reduce the storage and solution time of the method of moments. This is achieved through compression of the impedance matrix with the introduction of auxiliary functions. The technique was presented by Bleszynski et al. in [23]. Applications to EM scattering have been presented in [24] where an iterative solver has been used with the AIM. The use of higher order method of moments basis functions with the AIM are presented in [25], [26]. Recent modifications to the technique include the introduction of circulant AIM [27] for cylindrical structures as well as multiple-grid AIM [28].

2.2.6 Iterative Techniques

The iterative techniques are used in conjunction with domain decomposition techniques, to reduce the method of moments computational requirements. A technique to solve the Electric Field Integral Equation (EFIE) formulation of the method of moments is presented in [29]. This technique uses the forward backward algorithm and extends it to solve three dimensional problems.

An improvement of this technique is the Integral Equation Overlapped Domain Decomposition (IE-ODDM) technique. This technique builds on the forward backward buffer region iterative method developed in [29] and is applica-

ble to open and closed bodies. This technique is presented in [30] and provides fast convergence and higher domain decomposition for the matrix equation. The technique has been improved and hybridized with the MLFMA in [31] to improve the computational and memory requirements of the MLFMA. An iterative technique that replaces the method of moments basis functions with macro basis functions, which are defined on larger domains, is presented in [32]. This technique is used with the MLFMA.

2.2.7 Green's Function Modification Techniques

The Green's function techniques modify the Green's function in the MoM formulation in order to reduce the number of unknowns in the MoM matrix. These techniques are presented in [33] and [34]. The technique presented by Umashankar et al. divides the object by invoking the electromagnetic equivalence principle.

2.2.8 Other Matrix Simplification Methods

Some other techniques to simplify the MoM matrix include the wavelet based method of moments formulations [35], the use of other higher order basis functions [36] and techniques used with edge elements [37]. These techniques attempt to define other basis functions that simplify the MoM matrix.

2.3 Asymptotic Methods

The asymptotic methods represent the class of methods that increase in accuracy when the dimensions of the scatterer are large in comparison to the wavelength. These methods present an asymptotic representation of the solution in a series of inverse powers of k, the wave number, where only the first term is retained. The asymptotic representations are based on an ansatz that is the product of a rapidly varying exponential of a phase function and a slowly varying amplitude function. The mathematical ansatz is the assumed form of the equation describing a problem. This form is arrived at through analysis and the expected answer is tested after the equation is applied.

The two solution regions of the asymptotic solutions are the ray field zones and zones where ray field representations are invalid. The ray filed zones are regions where the field is locally similar to a plane wave. Zones in which the field cannot be approximated by a locally plane wave, are located at light-shadow boundaries and near the envelope of rays (caustic). There exist techniques to treat generic caustics, but these techniques fail on singular caustic curves and regions where many boundary layers overlap [38]. It then becomes necessary to calculate the surface scattered field in space through an integration of the currents in these regions. This effectively divides the asymptotic techniques

into ray based and current based techniques. Various asymptotic methods exist to predict various scattering characteristics, but none of these techniques are able to predict the surface travelling wave [1]. These asymptotic methods are discussed in the following sections.

2.3.1 Geometric Optics

Geometric Optics (GO) refers to the ray tracing techniques used in the optical frequency domain. This technique is based on incident, transmitted and reflected rays. Sommerfeld and Runge established a link between Maxwell's equations and ray optics by demonstrating the derivation of geometric optics laws from Helmholtz's scalar wave equation [38]. This was extended to vector fields by Ignatowsky and later formalized by Luneberg and Kline [38]. Luneberg and Kline showed that geometric optics is the first term of an asymptotic series. Their technique was able to account not only for the refraction and reflection at boundary surfaces, but the intensities of the waves as well [39]. Geometric Optics, however, predicts infinite results for flat or singly curved surfaces and does not account for diffraction.

2.3.1.1 Geometric Theory of Diffraction

The Geometric Theory of Diffraction (GTD) is a significant extension of the geometric optics to diffraction problems [4]. This technique was introduced by Keller in [40]. His technique incorporated the diffracted fields into the GO through a generalization of Fermat's principle [38]. This was based on the asymptotic evaluation of diffraction solutions of Maxwell's equations for canonical problems, such as a wedge.

Asymptotic uniform solutions were developed to overcome the limitations of the GTD by Kouyoumjian [4]. These solutions are the uniform theory of diffraction (UTD) of Kouyoumjian and Pathak [39] and the uniform asymptotic theory (UAT) of Lee and Deschamps [38]. The method of equivalent currents (MEC) is an extension of the GTD which removes the caustics of diffracted rays [38]. This technique replaces the diffracted field with equivalent line currents that can be found from the GTD diffraction coefficients.

2.3.2 Physical Optics

Physical Optics (PO) is derived from the Stratton-Chu integral equations [4]. Stratton showed that for open surfaces, additional terms could be added to the equations to account for edge discontinuity. Physical optics overcomes the GO infinite results for flat and singly curved surfaces through an integration of the induced surface fields to obtain the scattered field. The technique assumes that the incident electromagnetic field causes induced surface currents that are proportional to the magnetic field intensity on the illuminated areas of the

scatterer. The drawback of PO is that it does not account for surface currents in shadowed regions and the contributions from surface waves, multiple reflections and edge diffractions are not included. Recently, some PO formulations have been modified to account for these effects with the inclusion of additional terms and/or special currents.

2.3.3 Physical Theory of Diffraction

The Physical Theory of Diffraction (PTD) was developed by Ufimtsev in [41]. He developed this technique during the period in which Keller developed his GTD. PTD improves PO and is a superposition of the PO field and its correction [42].

Ufimtsev introduced the concepts of fringe fields and fringe waves and postulated that the current on the surface of a scatterer can be represented by the sum of uniform and fringe fields. The uniform field is associated with the regular portion of the surface, whilst the fringe field is associated with discontinuities. Ufimtsev used the canonical solution of the scattering by a wedge and retained the approximate physical optics result [4]. Due to GTD's reliance on the solution of this wedge, it is applicable to scattering directions that lie on the Keller cone [4].

This was improved upon by Mitzner with his incremental length diffraction coefficient (ILDC) technique, which extends the applicability of PTD to arbitrary scattering directions. Burton and Ufimtsev improved the formulation of PTD [38], for direct calculation of the fringe wave contribution pertaining to the scalar case. A recent improvement to PTD has been implemented by Ufimtsev in [43]. He proposes to remove the singularity at grazing directions to the edge faces. This technique defines a new uniform component for the surface current.

2.3.4 Shooting and Bouncing Rays

The Shooting and Bouncing Rays (SBR) technique was initially presented by Ling et al. in [44] for the calculation of the interior RCS from open cavities. The SBR is based on ray tracing, using GO laws. The PO is then used to determine the resulting scattered field from each ray. The advantage of this method is that it imposes no restrictions on the shape or material loading of the cavity and allows greater flexibility in geometrical modelling [45].

2.3.5 Spectral Theory of Diffraction

The Spectral Theory of Diffraction (STD) was introduced by Mittra et al. in [46], [47]. This technique represents the solution of diffraction problems with illuminating fields in the form of a spectrum of plane waves. Non-ray fields are presented in the form of a spectrum of plane waves. The technique

is valid in the transition region that contains the lit and shadow areas. The use of the STD to obtain uniform diffraction coefficients is proposed in [38].

2.4 Hybrid Methods

In the previous sections, the method of moments and asymptotic high frequency methods were discussed. The application of the asymptotic methods is sometimes met with difficulties in practice, because some objects contain rapidly varying geometrical features that are electrically too small to be modelled accurately with these methods. On the other hand, the full wave methods place excessive demands on computational power and are limited by the increase in the electrical size of bodies.

The hybrid methods attempt to supplement the limitations of both the full wave and asymptotic methods, through the combination of both types of methods. With these methods, the body is divided into portions that are solved using a full wave method and an asymptotic method. These hybrid techniques can be broadly classified into field-based and current-based hybrids [48], although there are other types of hybrid methods that exist. The field-based hybrids utilize asymptotic methods in the ray field solution regions in combination with a full wave technique. The current-based hybrids utilize a current-based asymptotic technique such as physical optics, with a current based full wave technique. In the following sections, the hybrid methods will be discussed in detail.

2.4.1 Current-based Hybrids

The current-based hybrid methods are based upon two methods that each utilise a current formulation. An important aspect of the current based hybrids is that the ansatz current must be valid in the region that it is applied to [49].

2.4.1.1 Method of Moments/Physical Optics (MoM/PO) Hybrid

The Method of Moments/Physical Optics (MoM/PO) hybrid is one of the most common hybrid methods in use. These two techniques lend themselves to hybridisation, because they are both current based. It is, therefore, possible to model a continuous current flow on the boundary between the two techniques. These techniques divide the scatterer into a MoM region and a PO region. The various formulations pertaining to the method of moments/physical optics hybrid are presented in this section.

Body of Revolution MoM/PO Early work in current hybrid techniques, utilizing both PO and Fock current theory, were presented by Medgyesi-Mitschang and Wang in [50]. Their work incorporated the Fock solution of currents, in

the asymptotic region, into the MoM. They later improved upon this technique in [51] by implementing a PO solution with the MoM for convex Bodies Of Revolution (BOR). A similar work was presented in [52] for dielectric analysis in large problems.

Surface Integral Equation Based Hybrids Integral equations can be derived for problems with currents flowing on surfaces in the same manner as the Pocklington equations [6]. The Electric Field Integral Equation (EFIE) relates the currents flowing on a surface to the incident electric field. The magnetic field integral equation (MFIE) relates the currents on a surface to the incident magnetic field. The EFIE is valid for both open and closed surfaces, while the MFIE is only valid for closed surfaces. In the EFIE hybrid formulations, the MoM solution is derived according to the EFIE. This is used to define the MoM boundary solution for the incident electric field and induced current [7].

Early hybrid formulations were presented by Kim and Rahmat-Samii in [53]. Their work presented a hybrid method utilizing basis functions over the MoM region and the PO region for 3D problems. In their work, they coupled the electric field due to the PO into the MoM and also the magnetic field due to the MoM into the PO solution. They applied this technique to the study of low profile antennas. Similar hybrid methods were presented in [54], [55], [56] and [57]. Some general guidelines for implementing this hybrid method are provided in [55]. Obelleiro's hybrid method in [54] includes complex geometries into the MoM region and implements a slightly different coupling method between the MoM and PO regions.

The MFIE hybrid formulations apply the MFIE to the MoM. One such technique was presented by Bilow in [58]. In his work, Bilow used the MoM/PO hybrid to obtain electric currents for a wedge problem and obtained the current expansion coefficients using the MFIE. This technique was later improved upon by Gong [59], with a modification of the basis functions close to the transition region for wedges. Obelleiro presented a replacement of the PO with an iterative solution of the MFIE for the hybrid in [54]. This technique includes multi-bounce effects in the PO region.

Improved Asymptotic Region Formulations Improvements to the MoM-PO hybrid method introduced in the previous section have been attempted in the literature. These improvements attempt to improve the accuracy of the asymptotic solution of the problem and can be done in various ways.

The technique presented by Wang in [60] improved the accuracy of currents in the PO region for bodies of revolution. In this work, Wang introduced a diffraction current term that improves the modeling of the non-specular effects of surface waves. Jakobus and Landstofer later introduced a fringe wave current term for flat polygonal parts of a scattering body in [3]. Their fringe wave current term incorporates edge effects in the PO region. They

subsequently developed a Fock current approximation for the currents in the asymptotic region without the use of the basis functions in [61]. They have also improved the memory requirements of the MoM/PO hybrid with the inclusion of the UTD, because of the low memory requirements of the UTD in [62]. A linear interpolation of the phase over the PO region is presented in [63], which allows the use of large PO triangles in the hybrid method. Similar asymptotic improvements in the hybrid are presented in [64].

Higher Order Basis Function Formulations Higher order techniques allow the use of basis functions defined on larger triangles, in order to reduce the number of unknowns in the conventional MoM/PO hybrid formulation, resulting in a more efficient method [65].

Jorgensen et al. explored the use of higher order basis functions in [66]. In this technique, they made use of higher order basis functions on higher order quadrilateral patches, in order to reduce the number of unknowns by a factor of 4 in the conventional MoM/PO hybrid method. A similar technique is presented in [67], where different higher order basis functions are defined in both the MoM and PO region. This technique allows the use of both small and large triangular patches in the same mesh. An improvement to this technique is presented in [68]; with an iterative algorithm that employs multiple reflections between PO currents.

Other Techniques Other formulations for the MoM/PO hybrid method include sparse matrix techniques, such as the one presented in [69], [70], Green's function modifications techniques in [71], [72] and a wavelet expansion in [73], to obtain the dominant components of the current.

2.4.1.2 Iterative Current Based Hybrids

Iterative techniques make use of some iterative algorithm in the full wave or asymptotic region of the problem.

MoM/PO Hybrid Iterative Techniques Iterative techniques have been presented by Kim and Thiele in [74]. This technique made use of the method of moments and an asymptotic current derived from the MFIE. This formulation was applied to diffraction problems in and close to the shadow boundary. This was later improved upon by Kaye et al. in [75], where the need for the MoM region is removed.

A combination of the EFIE and MFIE, to model both open and closed surfaces, has been presented in [76] for objects that are represented with wires and metallic surfaces. This technique retains MFIE terms that are usually neglected in the MoM/PO hybrid. This technique was later improved by Garcia et al. in [77]. Their technique made use of macro basis functions and an iterative Krylov approach.

Edlund developed a parallel iterative MoM/PO hybrid in [78]; this technique is based on the Gauss-Seidel process to avoid matrix and storage computations. An iterative asymptotic improvement method is presented in [79]. This technique is used to consider multiple interactions in the PO region of the MoM/PO.

Other Iterative Current Based Methods Other iterative current based methods include the EFIE based formulation in [80], the hybrid finite element method (FEM)/method of moments with PO, GTD and PTD for improved modeling of higher order interactions in 2D reflector antennas in [81]. A purely iterative technique used to solve for the MFIE with the inclusion of Fock and edge diffraction theory is presented in [82].

2.4.2 Field Based Hybrids

The field based hybrid methods make use of a field based ansatz, obtained from the GTD or a modification of the Green's function [83].

2.4.2.1 MoM/GTD Hybrid

The use of the MoM/GTD hybrid usually requires a known diffraction coefficient [48]. The hybrid technique was presented by Thiele et al. [84]. The GTD derived fields form a part of the problem and the rest of the problem geometry is represented with the MoM. The MoM region is represented by equivalent currents. This technique was further improved by Ekelman and Henderson [48], for wire antennas near curved surfaces. These techniques were developed for a variety of wedge diffraction solutions with the use of GO. The use of GTD limits the distance at which a source may be placed from a wedge and this has been addressed by Thiele et al. [48]. Thiele et al. have also developed techniques to combine the MoM with the surface wave diffraction theory and creeping wave theory of the UTD [48].

2.4.2.2 MoM/Green's Function Ansatz

A shortcoming of the MoM/GTD technique is limitations with reference to caustics and the proximity of field and source points [83]. This has been improved with the use of the EFIE formulation by using MoM to obtain a numerical Green's function for a problem. Harrington and Mautz used this approach to find the Green's function for a BOR [48]. This approach was later also used by Glisson and Butler to obtain the Green's function for a wire in the presence of a BOR [48]. Hybrid techniques with numerical Green's functions are highly accurate for complex and moderately large structures. Techniques which utilize this have been presented in [85], [86] and [87]. These techniques have proved useful for efficient parametric studies of antennas.

2.4.2.3 Other Field Based Hybrids

Other field based hybrid techniques include the GTD/MoM hybrid technique developed by Burnside et al. [88]. The difference between this method and the MoM/GTD hybrid is that only the form of the diffracted current away from the diffraction region is required. An improvement to this technique was presented in [89], with a series representation of the diffracted current that is valid at all angles. A similar technique using ray based image methods is presented in [90].

2.4.3 Other Hybrid Methods

Other hybrid methods that attempt to solve electrically large problems with complex detail include the asymptotic hybrid method by Weinmann in [91]. This technique makes use of ray tracing with PO/PTD to reduce the surface integral to ray contributions. Time domain hybrids are presented in [92], [93] and [94]. These time domain hybrids replace the numerical frequency domain based technique with a time domain technique.

2.5 Extraction Methods

The extraction methods are based on the extrapolation of a current distribution to high frequencies from the knowledge of low frequency solutions [95]. Such techniques have been reported to be possible and have been explored in various works [96].

The Asymptotic Phase Extraction (APE) introduced by Kwon et al. in [97] reduces storage and computation. This is done through the extraction of phase front characteristics of surface currents from known current samples at lower frequencies. The use of current modes to extrapolate a PO current has been explored by Catedra et al. in [98]. This technique avoids the use of dense sampling required by some rigorous methods. Sefi and Bergholm have used the PO and MoM to gain insights into the surface currents in order to model some currents in the shadow region in [96]. Their technique models the current based on the incident magnetic field.

2.6 Conclusion

In this work, literature pertaining to modeling of electrically large bodies with some electrically small complex detail was presented. The full wave methods provide exact solutions for electromagnetic wave scattering. These methods, however, place much demand on computing power as the electrical size of the problem is increased. Due to the demands on computational power, these

methods are, given current computing technology, usable for problems up to approximately tens of wavelengths in size.

The asymptotic methods provide an asymptotic series representation of the solution, where some of the first terms are retained. These methods work well when the smallest geometrical dimension of a problem is greater than 10 wavelengths. Various asymptotic techniques exist to model scattering properties such as reflection and diffraction, but few of these techniques are able to model the surface travelling wave. The asymptotic techniques become invalid when an electrically large body with some fine complex detail is modelled.

Attempts to improve the shortcomings of both the full wave and asymptotic methods are made by the hybrid methods. These hybrid methods supplement the shortcomings of both full wave and asymptotic methods. The current based hybrid methods combine a current based full wave method with current based asymptotic methods. The method of moments/physical optics (MoM/PO) hybrid is one of the most widely used current hybrid methods. This hybrid models a continuous current flow in the transition between the full wave and asymptotic region. Techniques that utilize the MoM/PO hybrid include body of revolution, surface integral and iterative techniques. Improvements to the MoM/PO have been made in the asymptotic solution region. Field based hybrid techniques make use of a field based ansatz or a Green's function modification in combination with a full wave method. The MoM/GTD is the earliest hybrid technique developed for field based hybrids. Green's function modifications improve limitations with reference to caustics in the GTD method.

Extraction methods extrapolate the current distribution at low frequencies, where full wave methods are effective, to higher frequency solutions. Methods that utilise extraction techniques reduce storage and computation through the insights gained from low frequency solutions of problems.

The next chapter will discuss the mathematical theory underlying the Method of Moments and the Physical Optics.

Chapter 3

Background

3.1 Introduction

In the previous chapter, an overview of the techniques that are applicable to electromagnetic scattering for electrically large structures was presented. In this chapter, the theory underlying the Method of Moments and the Physical Optics will be discussed.

3.2 Method of Moments

The Method of Moments is a general procedure for solving linear field problems. The technique reduces a functional equation to a matrix equation. Consider the deterministic equation [7]:

$$L(f) = g \tag{3.2.1}$$

where L is a linear operator, g is known and f is unknown. The operator L maps the function g to f. Let f be expanded a series of functions $f_1, f_2, f_3, \cdots$ in the domain of L as

$$f = \sum_n \alpha_n f_n \tag{3.2.2}$$

with α_n constants and f_n expansion functions (also known as basis functions). The summation in (3.2.2) is infinite for exact solutions and finite for approximate solutions. The f_n form a complete set of basis functions for exact solutions. Substitution of (3.2.2) into (3.2.1) results in the residual

$$R = L\sum_n \alpha_n f_n - g. \tag{3.2.3}$$

The residual is the difference between the approximate solution and exact solution. A point-matching procedure forces the residual to zero at N discrete

points. It is better to obtain an average value of the residual over the domain of the problem and set it to zero. This can be done by defining a set of *weighting functions*, or *testing functions*, $w_1, w_2, w_3, \cdots$ in the range of L. If it is assumed that a suitable inner product $< f, g >$ is defined for the problem; the inner product with each w_m results in

$$\sum_n \alpha_n < w_m, Lf_n > = < w_m, g > \tag{3.2.4}$$

with $m = 1, 2, 3, \cdots$. This set of equations can be written in matrix form as

$$[l_{mn}][\alpha_n] = [g_m] \tag{3.2.5}$$

where

$$[l_{mn}] = \begin{bmatrix} < w_1, Lf_1 > & < w_1, Lf_2 > & \cdots \\ < w_2, Lf_1 > & < w_2, Lf_2 > & \cdots \\ \cdots & \cdots & < w_m, Lf_n > \end{bmatrix} \tag{3.2.6}$$

$$[\alpha_n] = \begin{bmatrix} \alpha_1 \\ \alpha_2 \\ \vdots \end{bmatrix} \tag{3.2.7}$$

If the matrix $[I]$ is non-singular then its inverse I^{-1} exists. The α_n coefficients are then given by

$$[\alpha_n] = [I^{-1}_{nm}][g_m] \tag{3.2.8}$$

and the solution for f is given by (3.2.2). For concise expression, define the matrix of functions

$$[\tilde{f}] = [f_1 f_2 f_3 \cdots] \tag{3.2.9}$$

and write

$$f = [\tilde{f}_n][\alpha_n] = [\tilde{f}_n][I^{-1}_{mn}][g_m] \tag{3.2.10}$$

The solution to this equation may be exact or appropriate, depending on the choice of f_n and w_n. When w_n is chosen to be the same as f_n, this is known as *Garlekin's method*. Generally, f_n should be linearly independent and chosen such that some superposition approximates f in (3.2.2) reasonably well. The w_n should also be linearly independent and chosen such that the products $< w_n, g >$ depend on relatively independent properties of g.

3.3 Electric Field Integral Equation (EFIE) Formulation

An integral equation formulation for the surface current on induced on a scattering body is derived from boundary conditions on the electric field as in [2].

Let S denote the surface of an open or closed perfectly conducting scatterer with unit normal $\hat{\boldsymbol{n}}$. $\boldsymbol{E^i}$ is the incident electric field, due to an impressed source in the absence of the scatterer, which induces surface currents $\boldsymbol{J}$ on S. If S is an open surface, $\boldsymbol{J}$ is the vector sum of the surface currents on opposite sides of S; hence the normal components of $\boldsymbol{J}$ must vanish on boundaries of S. The scattered electric field $\boldsymbol{E^s}$ can be computed from the surface current $\boldsymbol{J}$ and charge σ by

$$\boldsymbol{E^s} = -j\omega\boldsymbol{A} - \nabla\Phi \tag{3.3.1}$$

with the magnetic vector potential defined as

$$\boldsymbol{A}(\boldsymbol{r}) = \frac{\mu}{4\pi}\int_S \boldsymbol{J}\frac{e^{-jkR}}{R}\mathrm{d}S' \tag{3.3.2}$$

and the scalar potential as

$$\boldsymbol{\Phi}(\boldsymbol{r}) = \frac{1}{4\pi\epsilon}\int_S \sigma\frac{e^{-jkR}}{R}\mathrm{d}S'. \tag{3.3.3}$$

A harmonic time dependence $\exp(j\omega t)$ is assumed and suppressed, $k = \omega\sqrt{\mu\epsilon} = 2\pi/\lambda$ with λ the wavelength in the homogeneous region exterior to S with permeability μ and permittivity ϵ. $R = \mid \boldsymbol{r} - \boldsymbol{r'} \mid$ is the distance between an arbitrarily located observation point $\boldsymbol{r}$ and a source point $\boldsymbol{r'}$ on S. Both $\boldsymbol{r}$ and $\boldsymbol{r'}$ are defined with respect to a global coordinate origin $\mathcal{O}$. The surface charge density σ is related to the surface divergence of $\boldsymbol{J}$, in the plane of the surface, through current continuity

$$\nabla_S \cdot \boldsymbol{J} = -j\omega\sigma. \tag{3.3.4}$$

An integro-differential equation for $\boldsymbol{J}$ is obtained by enforcing the boundary condition $\hat{\boldsymbol{n}} \times (\boldsymbol{E^i} + \boldsymbol{E^s}) = 0$ on S, resulting in

$$-\boldsymbol{E}^i_{tan} = (-j\omega\boldsymbol{A} - \nabla\Phi)_{tan}, \boldsymbol{r} \text{ on } S. \tag{3.3.5}$$

(3.3.5), with (3.3.2)-(3.3.4), constitute the mixed potential electric field integral equation. The presence of derivates on the current in (3.3.4) and scalar potential (3.3.5) suggest that care be taken in the selection of basis/expansion and testing functions in the method of moments(MoM).

3.3.1 Basis function development

In MoM surface problems, the geometry must be split up into smaller elements and the current on the surface must be approximated by some function. The set of basis functions introduced by Rao, Wilton and Glisson in [2] are suited to triangular patch modeling and for use with the EFIE. The basis functions are

often known as the RWG elements. The basis function is vector in nature and its individual scalar components can be recovered with some manipulation. Current continuity has to be enforced over an *edge* of a triangular patch and this can be achieved with the interpolation function

$$f(n) = \begin{cases} \frac{l_n}{2A_n^+}\boldsymbol{\rho}_n^+, & \boldsymbol{r} \text{ in } T_n^+ \\ \frac{l_n}{2A_n^-}\boldsymbol{\rho}_n^-, & \boldsymbol{r} \text{ in } T_n^- \\ 0, & \text{otherwise.} \end{cases} \tag{3.3.6}$$

The vectors $\boldsymbol{\rho}_n^+$ and $\boldsymbol{\rho}_n^-$ are illustrated in Figure 3.1. These position vectors are defined *relative to the relevant free vertex*. The basis function is associated with an *interior edge* of the patch and vanishes everywhere on S except in the two triangles attached to that edge. Two such triangles are T_n^+ and T_n^- in Figure 3.1. $A_n^{+/-}$ are the areas of triangles $T_n^{+/-}$ respectively. The length of the shared edge is l_n. Points within T_n^+ are designated by the position vector $\boldsymbol{\rho}_n^+$ defined with respect to the free vertex of T_n^+(left hand node); similarly points within T_n^- are defined with respect to the free vertex of T_n^-.

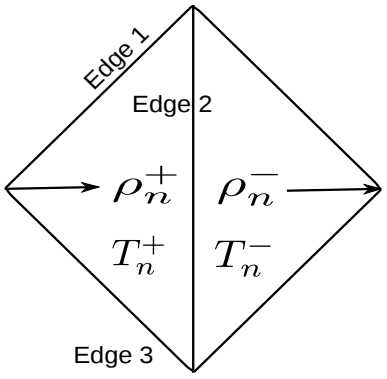

Figure 3.1: The RWG basis function on a common edge between triangles T_n^+ and T_n^-

The basis function $f_n(\boldsymbol{r})$ has no component normal to the boundary (upper and lower sides of either triangle) of the surface formed by the triangles T_n^+ and T_n^-. This means that no line charges will exist along this boundary between these triangles. The component normal to the shared edge is linearly interpolated in the tangential direction (along the edge) and interpolated as a constant normal to (across) the edge [2]. This latter factor normalises f_n such that its flux density normal to the shared edge is unity, ensuring continuity of current normal to the edge.

3.3.2 The MoM formulation

The surface divergence of f_n, which is proportional to the surface charge density associated with the RWG basis function, is

$$\nabla_s \cdot f(n) = \begin{cases} \frac{l_n}{A_n^+}, & \boldsymbol{r} \text{ in } T_n^+ \\ \frac{l_n}{A_n^-}, & \boldsymbol{r} \text{ in } T_n^- \\ \mathbf{0}, & \text{otherwise.} \end{cases} \tag{3.3.7}$$

This result can be derived with the use of simplex coordinates [2]. (3.3.7) shows that the charge density is constant in each triangle, the total charge of the triangle pair T_n^+ and T_n^- is zero, and is approximated by a *pulse doublet*.

The surface current on S is approximated by

$$\mathbf{J} = \sum_{n=1}^{N} I_n f_n(\boldsymbol{r}) \tag{3.3.8}$$

where N indicates the number of interior edges. There are three basis functions defined on each non-boundary edge of a triangular face but at any given edge; the basis function associated with that edge has a normal component of current. (3.3.8) also shows that the basis functions are independent in each triangle since the current I_n, normal to edge n, is an independent quantity. The sum of the normal components of current $\boldsymbol{J}$ on surface boundary edges cancels because of current continuity. There is, therefore, no need to define basis functions on these edges.

The testing functions are chosen to be the same as the basis functions $\boldsymbol{f_n}$. The symmetric product presented in (3.2.4) is defined as

$$< \boldsymbol{f}, \boldsymbol{g} >= \int_S \boldsymbol{f} \cdot \boldsymbol{g} \mathrm{d}S, \tag{3.3.9}$$

(3.3.5) is tested with $\boldsymbol{f}_m$, $m = 1, 2, \ldots, N$, yielding

$$< \boldsymbol{E}^i, \boldsymbol{f}_m >= j\omega < \boldsymbol{A}, \boldsymbol{f}_m > + < \nabla\Phi, \boldsymbol{f}_m > . \tag{3.3.10}$$

Application of the gradient operator to the surface charge σ, the expansion of which is the pulse doublet of (3.3.7), in Φ is not advisable. With the use of a surface vector calculus identity and the properties of $\boldsymbol{f}_m$, the last term in (3.3.10) can be written as

$$< \nabla\Phi, \boldsymbol{f}_m >= -\int_S \Phi \nabla_S \cdot \boldsymbol{f_m} \mathrm{d}S. \tag{3.3.11}$$

The differential has now been moved to the testing function, which has the appropriate first order terms to obtain a finite result. With (3.3.7), the integral in (3.3.11) can now be written and approximated as follows:

$$\begin{aligned}\int_S \nabla\Phi_S \cdot \boldsymbol{f}_m \mathrm{d}S &= l_m\left(\frac{1}{A_m^+}\int_{T_m^+}\Phi \mathrm{d}S - \frac{1}{A_m^-}\int_{T_m^-}\Phi \mathrm{d}S\right) \\ &= l_m[\Phi(\boldsymbol{r}_m^{c+}) - \Phi(\boldsymbol{r}_m^{c-})].\end{aligned} \tag{3.3.12}$$

In (3.3.12), the average of Φ over each triangle is approximated by the value of Φ at the triangle centroid, where c^+ and c^- refer to the centroids of the $+$ and - triangles respectively. Similar approximations can be applied to the vector potential and incident field terms in (3.3.10) to obtain

$$\begin{aligned}\left\langle \begin{Bmatrix}\boldsymbol{E}^i \\ \boldsymbol{A}\end{Bmatrix}, \boldsymbol{f}_m \right\rangle &= l_m\left[\frac{1}{2A_m^+}\int_{T_m^+}\begin{Bmatrix}\boldsymbol{E}^i \\ \boldsymbol{A}\end{Bmatrix}\cdot\boldsymbol{\rho}_m^+ \mathrm{d}S + \frac{1}{2A_m^-}\int_{T_m^-}\begin{Bmatrix}\boldsymbol{E}^i \\ \boldsymbol{A}\end{Bmatrix}\cdot\boldsymbol{\rho}_m^- \mathrm{d}S\right] \\ &= \frac{l_m}{2}\left[\begin{Bmatrix}\boldsymbol{E}^i(r_m^{c+}) \\ \boldsymbol{A}(r_m^{c+})\end{Bmatrix}\cdot\boldsymbol{\rho}_m^+ + \begin{Bmatrix}\boldsymbol{E}^i(r_m^{c-}) \\ \boldsymbol{A}(r_m^{c-})\end{Bmatrix}\cdot\boldsymbol{\rho}_m^-\right],\end{aligned} \tag{3.3.13}$$

where the integral over each triangle is eliminated by approximating $\boldsymbol{E}^i$ (or $\boldsymbol{A}$) by its value at the triangle centroid. With (3.3.11)-(3.3.13), (3.3.10) becomes

$$\begin{aligned}j\omega l_m[\boldsymbol{A}(r_m^{c+})\cdot\frac{\boldsymbol{\rho}_m^{c+}}{2} + \boldsymbol{A}(r_m^{c-})\cdot\frac{\boldsymbol{\rho}_m^{c-}}{2}] + l_m[\Phi(r_m^{c-}) - \Phi(r_m^{c+})] \\ = l_m[\boldsymbol{E}^i(r_m^{c+})\cdot\frac{\boldsymbol{\rho}_m^{c+}}{2} + \boldsymbol{E}^i(r_m^{c-})\cdot\frac{\boldsymbol{\rho}_m^{c-}}{2}],\end{aligned} \tag{3.3.14}$$

which is the equation enforced at each triangle edge, $m = 1, 2, \cdots, N$. The testing procedure reduces the differentiation requirements on (3.3.5) by integrating $\nabla\Phi$ first. (3.3.12) and (3.3.13) eliminate the surface integrals of the potential quantities and allow a double surface integral to be approximated by a quantity containing a single surface integral. This reduces the computational cost of moment matrix elements as this is computed numerically, using quadrature. The integrations are thus performed only over the source elements. This is an approximate implementation of the Galerkin method [6]. This approach does not yield a symmetrical matrix as would be expected with the Galerkin formulation. This approximation also admits another interpretation. If a "razor-blade" testing function is defined along the line connecting triangle centroids; approximating that integral with the integrands evaluated at centroids, the result is identical [6].

3.3.3 Matrix equation entries derivation

Substituting the current expansion of (3.3.8) into (3.3.14) yields the system of $N \times N$ linear equations of the MoM formulation, written as

$$V = ZI \tag{3.3.15}$$

where $Z = [Z_{mn}]$ is an $N \times N$ matrix; $I = [I_n]$ and $V = [V_m]$ are column vectors of length N. The elements of Z and V are given by

$$Z_{mn} = l_m \left[j\omega \left(\boldsymbol{A}^+_{mn} \cdot \frac{\boldsymbol{\rho}^{c+}_m}{2} + \boldsymbol{A}^-_{mn} \cdot \frac{\boldsymbol{\rho}^{c-}_m}{2} \right) + \Phi^-_{mn} - \Phi^+_{mn} \right] \tag{3.3.16}$$

$$V_m = l_m \left(\boldsymbol{E}^+_m \cdot \frac{\boldsymbol{\rho}^{c+}_m}{2} + \boldsymbol{E}^-_m \cdot \frac{\boldsymbol{\rho}^{c-}_m}{2} \right) \tag{3.3.17}$$

where

$$\boldsymbol{A}^\pm_{mn} = \frac{\mu}{4\pi} \int_S \boldsymbol{f}_n(\boldsymbol{r'}) \frac{e^{-jkR^\pm_m}}{R_m} \mathrm{d}S \tag{3.3.18}$$

$$\Phi^\pm_{mn} = -\frac{1}{4\pi j\omega\epsilon} \int_S \nabla'_S \cdot \boldsymbol{f}_n(\boldsymbol{r'}) \frac{e^{-jkR^\pm_m}}{R_m} \mathrm{d}S \tag{3.3.19}$$

$$R^\pm_{mn} = |\boldsymbol{r}^{c\pm}_m - \boldsymbol{r'}| \tag{3.3.20}$$

and

$$\boldsymbol{E}^\pm_m = \boldsymbol{E}^i(\boldsymbol{r}^{c\pm}_m). \tag{3.3.21}$$

For a plane incidence, the electric field is set to

$$\boldsymbol{E}^i(\boldsymbol{r}) = (E_\theta \hat{\theta}_0 + E_\phi \hat{\phi}_0) e^{-j\boldsymbol{k}\cdot\boldsymbol{r}} \tag{3.3.22}$$

with the propagation vector $\boldsymbol{k}$ given by

$$\boldsymbol{k} = k(\sin\theta_0 \cos\phi_0 \hat{\boldsymbol{x}} + \sin\theta_0 \sin\phi_0 \hat{\boldsymbol{y}} + \cos\theta_0 \hat{\boldsymbol{z}}) \tag{3.3.23}$$

and the quantities $\hat{\theta}_0$ and $\hat{\phi}_0$ denote the angle of arrival of the plane wave in spherical coordinates.

Once the elements of the MoM matrix and the V vector are determined, the resulting system of linear equations may be solved for the unknown vector I in (3.3.15). The computation of the elements of Z_{mn} requires the computation of (3.3.18)-(3.3.20), an efficient numerical computation scheme of these elements is presented in the original RWG formulation [2]. It must be noted that the Green's function in (3.3.18) contains the distance the between the source point and testing point, R_m. This integral can become singular when the source and test point are collocated or sufficiently close together. The resulting self term, Z_{mm} can be handled via various singularity evaluation schemes. The simplest and often most encountered scheme is the avoidance of the singularity term by ensuring the source and test points are not at the same location. In this work, a singular scheme which transforms the triangular points into a quadrilateral region where the singularity is integrable using Gaussian quadrature rules.

To obtain the scattered fields, the resulting currents on each triangle can be integrated over the region of the surface using the radiation integrals in [5].

A more commonly used approach to determine the scattered field, valid when the resolution of the mesh triangles is much smaller than a wavelength, is the dipole approximation. With this technique, each triangle pair is considered as a small dipole, having a dipole moment directed between the triangle centroids. The total scattered field is then obtained as a sum of all the contributions of these dipoles. The dipole moment is a product of an effective dipole current and dipole length given by [5]:

$$\boldsymbol{m}_n = l_n I_n (\boldsymbol{r}_n^{c-} - \boldsymbol{r}_n^{c+}). \tag{3.3.24}$$

The electric field due to a dipole at the origin is

$$\begin{aligned}\boldsymbol{E}_n(\boldsymbol{r}) = \frac{\eta_o e^{-jkr}}{4\pi}\Big\{\Big[\frac{\boldsymbol{r}\cdot\boldsymbol{m}_n}{r^2} - \boldsymbol{m}_n\Big]\Big(\frac{jk}{r} + \frac{1}{r^2}\Big[1 + \frac{1}{jkr}\Big]\Big) \\ + 2\Big(\frac{\boldsymbol{r}\cdot\boldsymbol{m}_n}{r^2}\Big)\frac{1}{r^2}\Big[1 + \frac{1}{jkr}\Big]\Big\}\end{aligned} \tag{3.3.25}$$

where $\boldsymbol{r}$ is the vector from the dipole centre to the observation point and η_o is the free space impedance. (3.3.25) is represents the exact scattered field without any far field approximations. The practical limitation of this formulation is that it is restricted by the size of the RWG element. When the observation distance is in the order of the RWG element length, the dipole approximation performs poorly.

3.3.4 Application of the RWG MoM formulation

The developed RWG MoM formulation is demonstrated using a square perfectly conducting flat plate in and a dihedral corner reflector.

The currents on the 1λ square flat plate are illustrated in Figure 3.2. These currents are generated for a mesh resolution of $\lambda/10$. Good agreement is shown between the developed technique and the reference results. This reference result is obtained from the EM simulation package *FEKO*. The slight differences observed between the results can be attributed to the difference in singularity handling schemes that are used in this formulation and the theoretical formulation. More accurate singularity integration schemes can yield better results.

Figure 3.3 illustrates the monostatic scattering cross section off the plate. Good agreement is again observed between the MoM and the reference solution. As the size of the mesh resolution is varied, the resulting scattering cross section also varies as illustrated in Figure 3.4. In this figure, the mesh resolution is varied from $\lambda/10$ to $\lambda/6$. Nonetheless, good agreement is still observed between this technique and the reference solution because the dipole approximation is still valid. The slight discrepancies between the reference results and this technique can again be attributed to the difference in integration

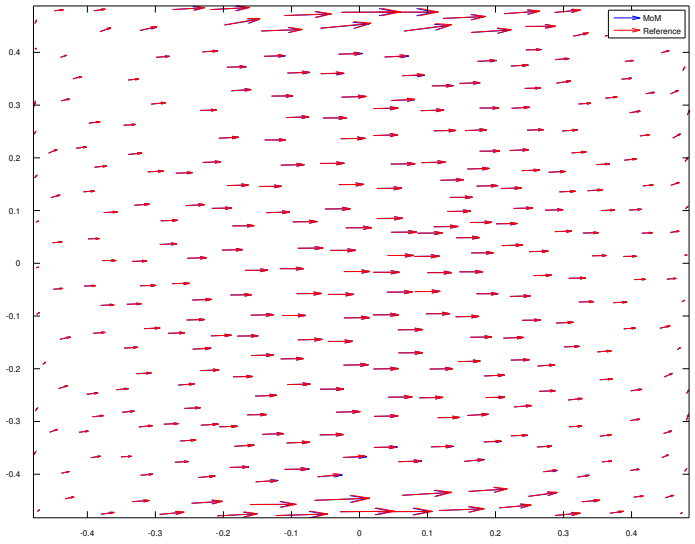

Figure 3.2: Current density on λ square plate

schemes used. This formulation makes use of a six point Gaussian quadrature integration scheme.

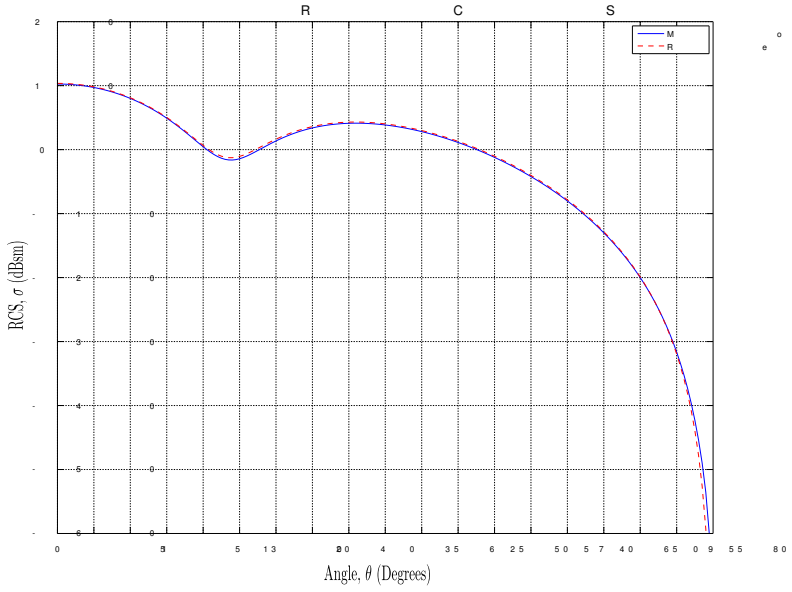

Figure 3.3: Monostatic radar cross section of λ square plate

The dihedral corner reflector of Figure 3.5 is simulated with an incident field that varies from $\theta = 0°$ to $\theta = 90°$, for fixed $\phi = 0°$. The scattered field

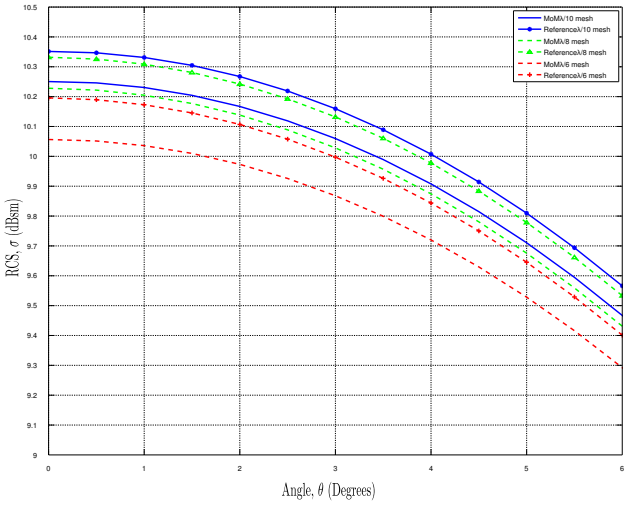

Figure 3.4: Monostatic radar cross section of λ square plate as mesh resolution is varied

obtained with the dipole approximation is illustrated in Figure 3.6. Again, good agreement is observed between this formulation and the reference result. The slight asymmetry between the two results can be attributed to the different geometrical mesh models used for the two results.

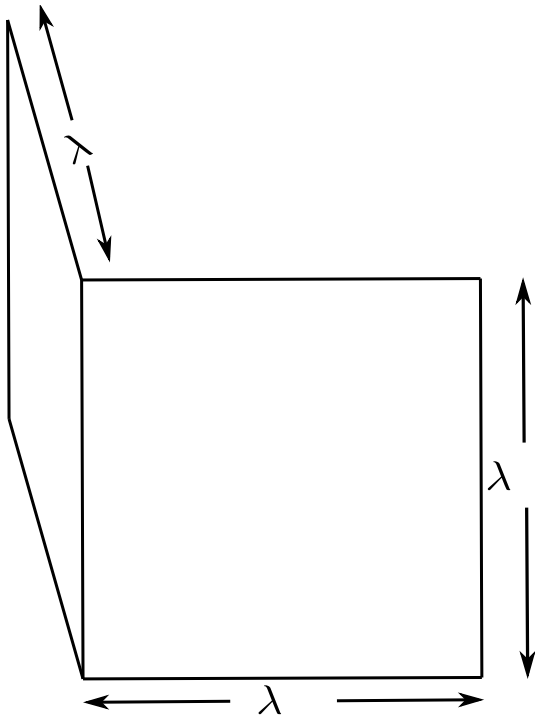

Figure 3.5: $\lambda \times \lambda \times \lambda$ dihedral corner reflector

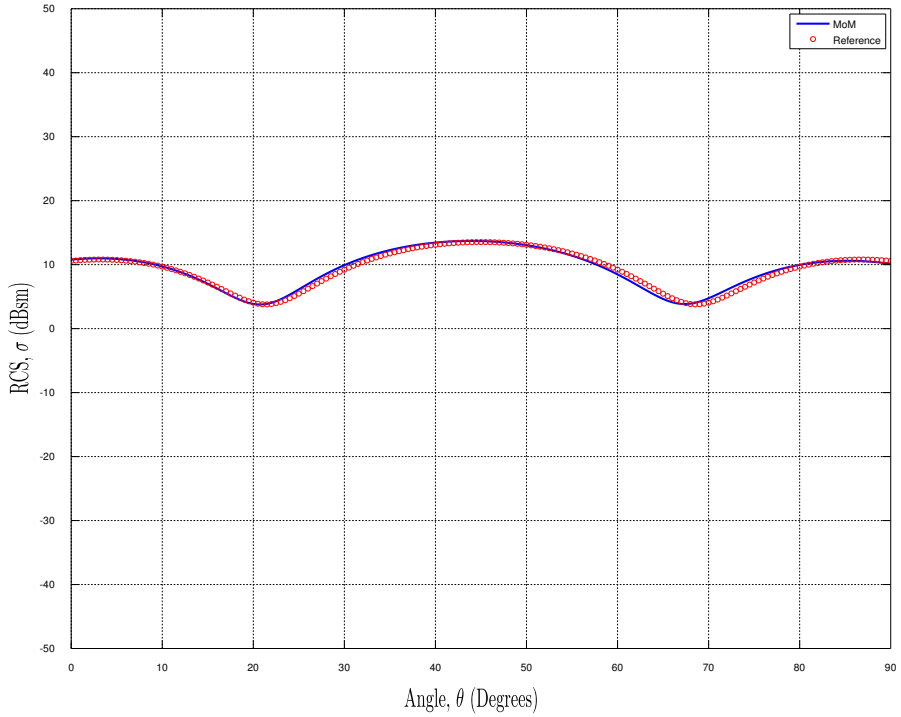

Figure 3.6: Monostatic radar cross section of dihedral corner reflector

3.4 Physical Optics (PO)

In this section, the development in [5] is followed. The *Physical Optics approximation* provides an estimate for an unknown current on an electrically large body, S. The current in the illuminated part of the body is approximated with the *Geometrical Optics* current whilst no current exists in the shadowed part as follows:

$$\boldsymbol{J}_S \approx \begin{cases} 2\hat{n} \times \boldsymbol{H}^i, & \text{for the illuminated portion} \\ 0, & \text{for the shadowed portion} \end{cases} \tag{3.4.1}$$

where $\boldsymbol{H}^i$ is the incident magnetic field intensity at the surface S and $\hat{n}$ in the local surface normal unit vector. The PO is an approximation of the magnetic field integral equation (MFIE) and can be seen as an application of the equivalence principle.

3.4.1 Scattering from a rectangular plate with the PO

Consider the rectangular plate with sides a and b in Figure 3.7.

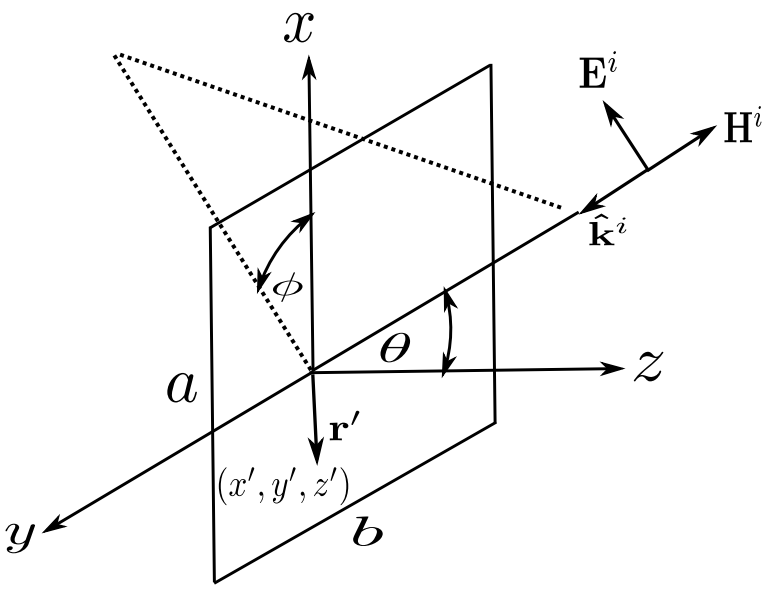

Figure 3.7: Rectangular plate with incident plane wave [5]

$\boldsymbol{E}^i$ represents the planar incident electric field with arbitrary polarisation incident from an angle (θ_0, ϕ_0). The wave polarisation is determined by the constants E_θ and E_ϕ in

$$\boldsymbol{E}^i = (E_\theta \hat{\theta}_0 + E_\phi \hat{\phi}_0) e^{-j\boldsymbol{k}\cdot\boldsymbol{r}}. \tag{3.4.2}$$

When the wave is propagating towards the origin, the propagation vector $\hat{\boldsymbol{k}} = -\hat{\boldsymbol{r}}$, the vector to the incident field point, and the magnetic field intensity is given by

$$\boldsymbol{H}^i = \frac{-\hat{\boldsymbol{r}} \times \boldsymbol{E}^i}{\eta} = -(E_\theta \hat{\theta}_0 - E_\phi \hat{\phi}_0) \frac{e^{-j\boldsymbol{k}\cdot\boldsymbol{r}}}{\eta}, \tag{3.4.3}$$

where the above equation (3.4.3) assumes that the plate is located in a medium with intrinsic impedance η. The current on the plate can therefore be approximated, using (3.4.1), by

$$\boldsymbol{J}_S \approx -2\hat{\boldsymbol{z}} \times (E_\theta \hat{\theta}_0 - E_\phi \hat{\phi}_0) \frac{e^{-j\boldsymbol{k}\cdot\boldsymbol{r}}}{\eta} \tag{3.4.4}$$

where the vectors and products are defined by

$$\boldsymbol{r'} = \text{position vector for a point}(x', y', z')\text{on the surface} = \hat{\boldsymbol{x}}x' + \hat{\boldsymbol{y}}x' \tag{3.4.5}$$

$$-\hat{\boldsymbol{k}}^i = \hat{\boldsymbol{x}}\sin\theta\cos\phi + \hat{\boldsymbol{y}}\sin\theta\sin\phi + \hat{\boldsymbol{z}}\cos\theta \tag{3.4.6}$$

$$-\boldsymbol{k}^i \cdot \boldsymbol{r} = k(x'\sin\theta\cos\phi + y'\sin\theta\sin\phi) \tag{3.4.7}$$

$$\hat{z} \times \hat{\theta} = -\hat{\boldsymbol{x}}\cos\theta\sin\phi + \hat{\boldsymbol{y}}\cos\theta\cos\phi \tag{3.4.8}$$

$$\hat{z} \times \hat{\phi} = -\hat{\boldsymbol{x}}\cos\phi - \hat{\boldsymbol{y}}\sin\phi. \tag{3.4.9}$$

Using the equations (3.4.5)-(3.4.9) in (3.4.4), the approximation for the current can be written as

$$\boldsymbol{J}_S \approx \frac{-2e^{jkh}}{\eta}[\hat{\boldsymbol{x}}(E_\theta\cos\phi - E_\phi\cos\theta\sin\phi) + \hat{\boldsymbol{y}}(E_\theta\sin\phi + E_\phi\cos\theta\cos\phi)], \tag{3.4.10}$$

where the quantity $h = x'\sin\theta\cos\phi + y'\sin\theta\sin\phi$. (3.4.10) can now be used as the approximate surface current on the rectangular plate S.

3.4.2 Application of the PO

The PO is illustrated using a perfectly conducting plate of with side λ. For this formulation, the RWG functions are used to calculate the PO since this is just a projection of the incident magnetic field onto the RWG basis functions. The mesh resolution is set to $\lambda/10$ for each triangular edge length. Figure 3.8 illustrates the currents on the plate for a normally incident plane wave, compared with a reference result from *FEKO*. Again, good agreement is observed between the PO currents and the reference solution. It must be noted, however, that the difference between the current results at the edges of the plate is due to the zero normla component of current in this formulation. In the reference result, the normal component of current is assumed not to be zero for the PO to be valid in this region. Physically, this is an approximation and is incorrect as the normal component of the current will be zero here. The effect of these currents is noticeable in the scattering cross section result of Figure 3.9.

The difference in the scattered field result between this PO implementation and the reference solution is as a result of the plate edge currents. To minimise the effect of these currents, the mesh resolution is increased to $\lambda/40$ and the result is illustrated in Figure 3.10. This result illustrates that this formulation converges towards the reference result as the effect of the edge currents is minimised.

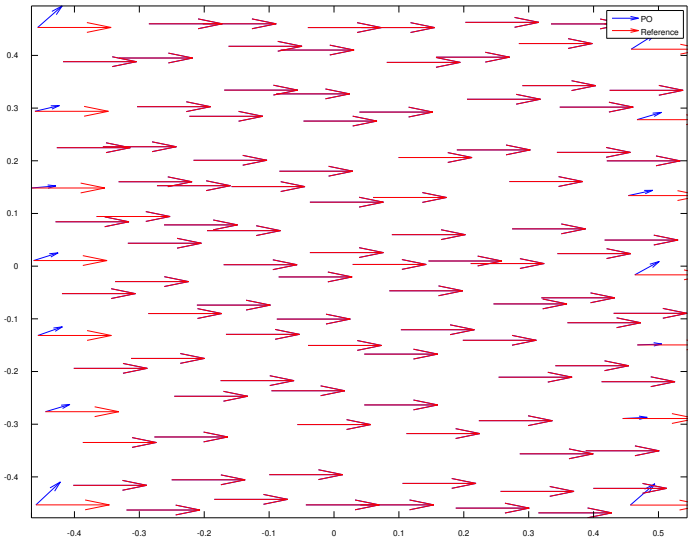

Figure 3.8: Current density on λ square plate

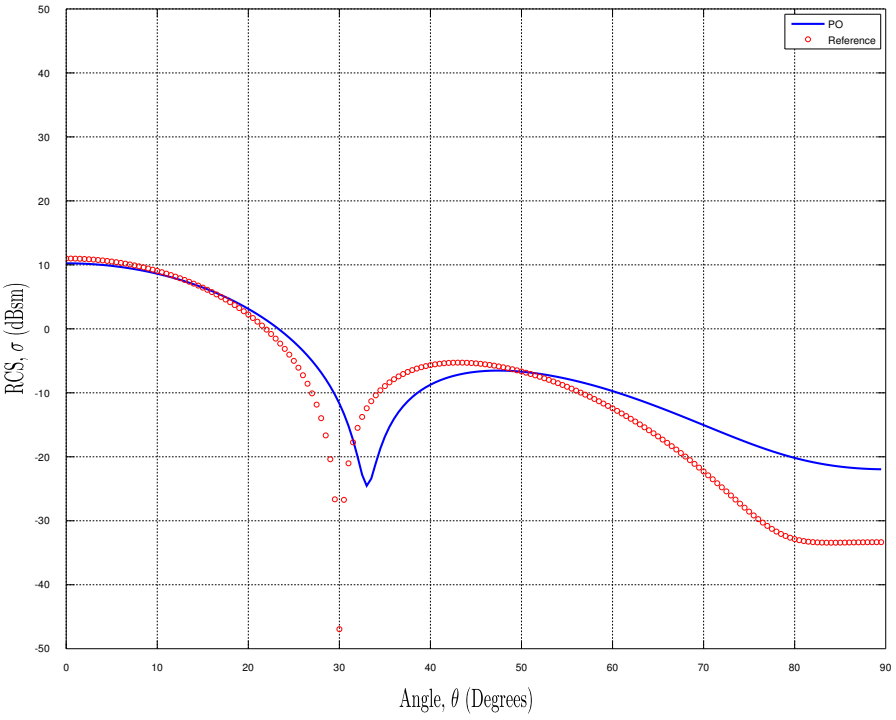

Figure 3.9: Monostatic RCS for PO on λ square plate

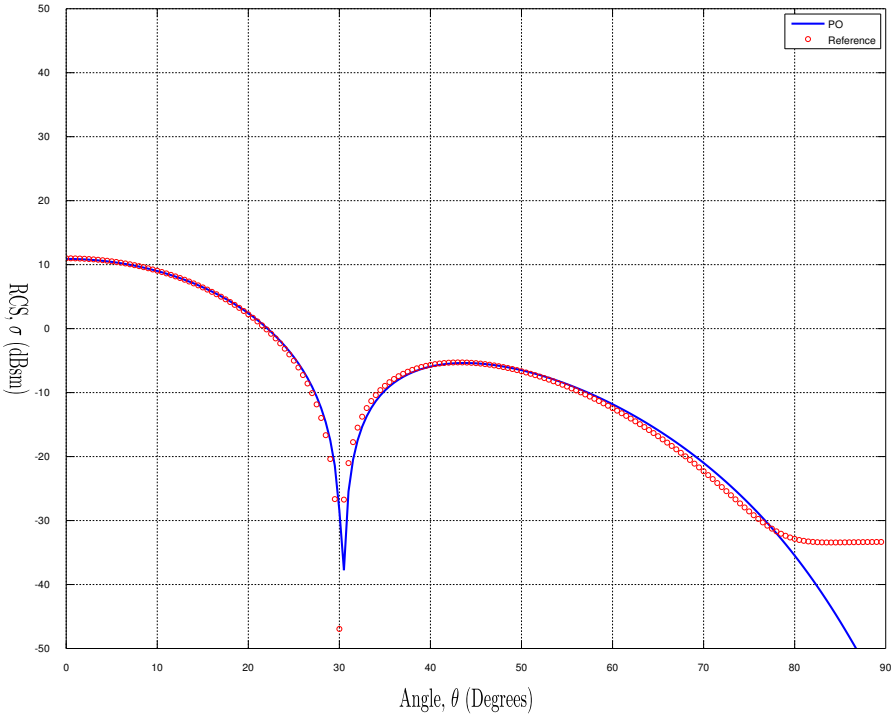

Figure 3.10: Effect of minimised edge current effects on monostatic RCS

3.5 Conclusion

In this chapter, the electric field integral equation application of the Method of Moments and the Physical Optics were presented. The Method of Moments, although providing a rigorous full wave solution for EM scattering applications, demands an increase in computer memory in the order of n^2 with an increase in the electrical size of the problem. The Physical Optics provides an approximate solution for electrically large problems. This method works well when the size of the object is much bigger than the wavelength. The PO currents in the current formulation are set to zero normal to the boundaries of edge geometries, this results in discrepancies between the scattered field and requires that the edge current effects be minimised.

In the following chapter, the development of the Method of Moments/Physical Optics hybrid is presented in the context of finding solutions for electrically large problems.

Chapter 4

Hybrid Technique Development

4.1 Introduction

In the previous chapter, the mathematical development of the Method of Moments and Physical Optics were presented. In this chapter, the development of the hybrid Method of Moments/Physical Optics (MoM/PO) technique is presented. A comparison of the performance of the Method of Moments and Physical Optics is presented, followed by the hybridisation of the two techniques. Finally, a modification to this hybridised MoM/PO method, that allows the use of large triangular mesh elements in the PO region, is presented.

4.2 Comparison between the MoM and PO

Although the MoM is a numerically rigorous method, it can be computationally costly for electrically large scatterers. In comparison, the PO works well for electrically large problems at the expense of numerical accuracy. The MoM computational requirements are in the order $O(N^2)$ for storage of the matrix entries and $O(N^3)$ for the solution, where N is the number of unknowns. N is directly related to the size of the scatterer and a density of 50-200 unknowns per square wavelength of the surface area is widely used.

For Radar Cross Section (RCS) analysis, electrically large scatterers are often encountered due to the high operating frequencies of some radar systems. Thus, use of the MoM can be computationally costly when analysing some radar targets. The PO is well suited to these types of problems but cannot model complex detail.

The following example serves to illustrate the computational cost and accuracy of the MoM and PO. EM phenomenon that is exhibited by radar targets includes diffraction, refraction, creeping waves and travelling waves. The missile model in Figure 4.1 is an example of such a target. Missiles often have additional effects such as curvature discontinuity returns, tip diffraction, interaction echoes and cavity returns [99]. The missile body has a length of $1m$ with

a spherical cap of $70mm$ diameter. The front fins of the missile are approximated with a square plate of side $30mm$ while the rear fins are approximated with a square plate of side $50mm$.

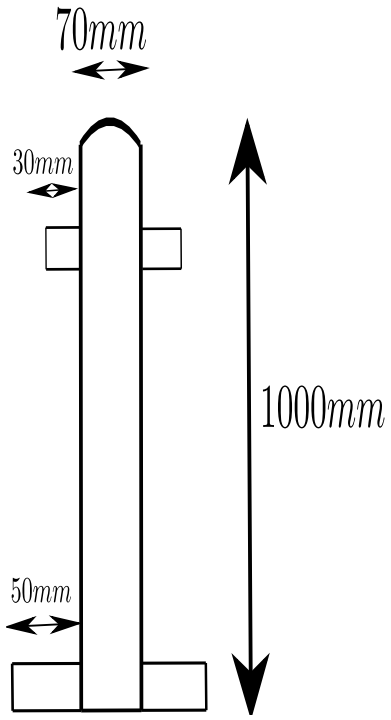

Figure 4.1: Simplistic missile model in millimetres

For this example, the computational requirements of the MoM and PO are obtained from the EM modelling and simulation package *FEKO*. The missile is simulated at the typical radar X-band frequency of 10GHz. It is simulated on a 64 bit machine with 2 *Intel* Xenon X5550 CPUs and 4 hyper threaded cores. The machine has a 2.67GHz processor and a total of 48GB RAM. It is found that for this model, the MoM requires a peak memory usage of 222 GB of memory while the PO requires only 560.656 MB. As a result, it was not possible to complete the simulation for the MoM. Use of the Multilevel Fast Multipole Method requires 1.275 GB of memory, using the combined field integral equation formulation to achieve faster matrix convergence. The monostatic scattering result in the plane $\phi = 0°$ for the PO and MLFMM result is illustrated in Figure 4.2.

Although the PO does not place stringent memory requirements on the computer, the PO solution does not account for some of the complex scattering phenomenon on the missile. In theory, the incident wave on the missile travels around the spherical cap and should be diffracted by the fins along the body of the missile. This diffracted wave at the missile fins will also be re-radiated at these points. The PO does not account for the coupling between the fins and

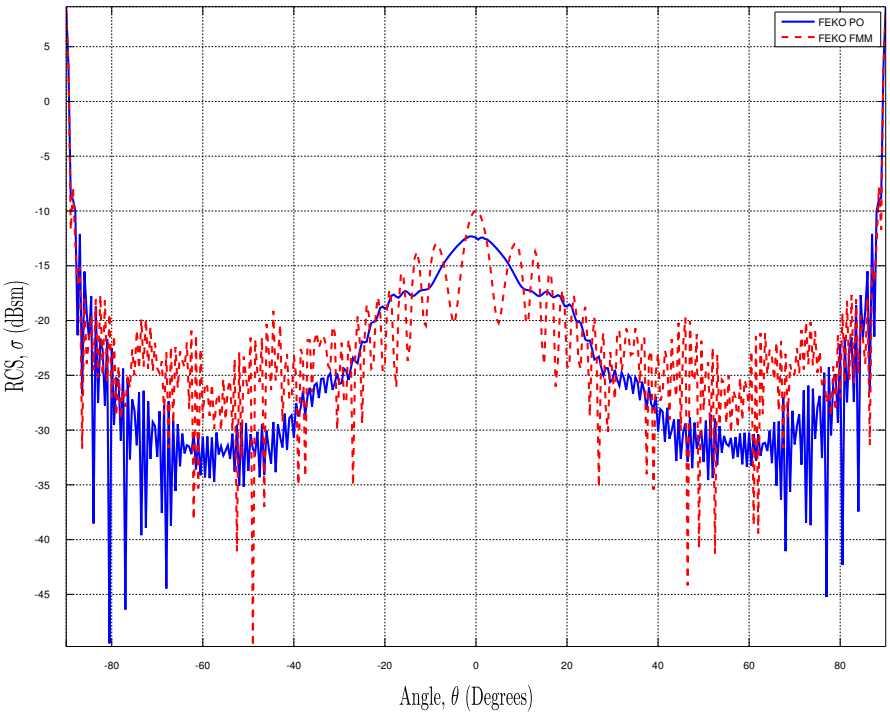

Figure 4.2: Monostatic radar cross section of simple missile model

the body, as seen in the fluctuations of the scattered RCS achieved with the MLFMM, but treats each as independent objects. Ideally, a rigorous solution of this problem, such as the solution achieved with the MLFMM, is required with the computational efficiency of the PO. With the use of a hybrid technique, the complex detail such as the spherical cap of the missile, the missile fins and immediate surrounding area can be modelled using the MoM and the remainder of the problem using the PO. This would ensure that complex EM phenomenon is accounted for by the MoM and a reduction in the number of MoM unknowns is achieved with the use of the PO. As demonstrated, a complete evaluation of this problem with the MoM would require the use of a machine capable of solving problems of this magnitude.

4.3 Hybrid MoM/PO development

The hybrid method development follows the notation in [3]. The hybrid method aims to decrease the number of unknowns in the Method of Moments. The advantage of using the PO for hybridisation with the MoM is that, unlike most asymptotic methods, the PO is current based. This leads to a seamless hybridisation process between the two techniques.

Consider the surface in Figure 4.3, the scattering surface is divided into a MoM region and a PO region. The MoM is applied to small, resonant structures and near edges whilst the PO can be applied to large smooth surfaces. It is advisable to assign the MoM and PO region taking into account the physical properties of the scattering surface in order to allow for an efficient hybrid method.

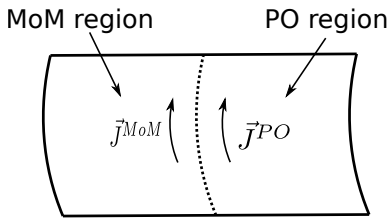

Figure 4.3: Subdivision of the scattering surface [3]

In the general method of moments, the scattered fields are due to currents on surfaces ($\boldsymbol{J}^{MoM}$) and wires. These currents are expanded according to the standard method of moments basis functions:

$$\boldsymbol{J}^{MoM} = \sum_{n=1}^{N_J^{MoM}} \alpha_n \cdot \boldsymbol{f}_n \tag{4.3.1}$$

where the widely used RWG [2] surface vector basis functions

$$\boldsymbol{f}_n(r) = \begin{cases} \frac{l_n}{2A_n^+}\boldsymbol{\rho}_n^+, & \boldsymbol{r} \text{ in } T_n^+ \\ \frac{l_n}{2A_n^-}\boldsymbol{\rho}_n^-, & \boldsymbol{r} \text{ in } T_n^- \\ 0, & \text{otherwise,} \end{cases} \tag{4.3.2}$$

are employed. The current along wires in (**??**) can be expanded according to triangular basis functions γ_n. In the PO region, the surface current density $\boldsymbol{J}^{PO}$ is also expanded according to the basis functions $\boldsymbol{f}_n$ in (4.3.2) as

$$\boldsymbol{J}^{PO} = \sum_{n=N_J^{MoM}+1}^{N_J^{MoM}+N_J^{PO}} \gamma_n \cdot \boldsymbol{f}_n. \tag{4.3.3}$$

The $\boldsymbol{f}_n$ are the RWG basis functions and the γ_n are the unknown coefficients. These N_J^{PO} coefficients are not obtained with the solution of a system of linear equations as in the MoM. These are obtained through an application of the PO and the hence, the matrix size remains N_J^{MoM}. For any given surface subdivided into triangular patches, N_J basis functions are usually required from the MoM. With this hybrid technique, an arbitrary subset of N_J^{MoM} selected basis functions can be assigned to the MoM region. The remaining $N_J^{PO} = N_J - N_J^{MoM}$ basis functions now represent the PO region. Due to

the fact that the basis functions overlap, there is no sharp boundary between the MoM and the PO region. This is one advantage of hybridising the two current methods as this allows for a continuous current flow over the surface of the scatterer. Compared to the conventional MoM, the size of the matrix is reduced from N_J to $N_J - N_J^{PO}$.

In the PO region, the current is given by (using linear operator notation):

$$\boldsymbol{J}^{PO}(r) = 2\delta_i \cdot \hat{n} \times \boldsymbol{H}^i(r) + \sum_{n=1}^{N_J^{MoM}} 2\alpha_n \delta_{J,n} \cdot \hat{n} \times \boldsymbol{\mathcal{L}}_J^H \boldsymbol{f}_n \tag{4.3.4}$$

The first term in (4.3.4) represents the PO current due to the impressed magnetic field $\boldsymbol{H}^i$, $\hat{n}$ represents the normal vector on the surface and δ_i accounts for shadowing effects. When the observation point on the surface is shadowed from the incident field, δ_i must be set to zero; else it is set to ± 1 depending on the direction of incidence with respect to the orientation of $\hat{n}$.

The second and third terms in (4.3.4) represents the effect of the currents in the MoM region. A summation takes place over the basis function $\boldsymbol{f}_n$ with coefficient α_n. The linear operator $\boldsymbol{\mathcal{L}}_J^H$ yields the magnetic field strength due to the function $\boldsymbol{f}_n$. The PO current density is again given by the vector product $2\hat{n}\times$ where $\delta_{J,n}$ accounts for shadowing effects on the observation point r in the PO region with respect to the basis function $\boldsymbol{f}_n$ acting as a source.

The formulation (4.3.4) is analogous to the magnetic field integral equation (MFIE) formulation [5]. The first term represents the scattered magnetic field as a result of the incident magnetic field and the second term represents the field scattered on the surface triangle elements. In this MoM/PO hybrid, however, the magnetic field scattered by triangular elements in the PO region is ignored. Special treatment of the $\boldsymbol{\mathcal{L}}_J^H \boldsymbol{f}_n$ operator acting on the basis functions in the MoM region is required in order to evaluate (4.3.4). The evaluation of this term is derived directly from the evaluation of the MFIE in [100]. The MFIE is expressed as:

$$\boldsymbol{J}(r) = 2\hat{n} \times \boldsymbol{H}^i(r) + 2\hat{n} \times \int \boldsymbol{J}(\boldsymbol{r'}) \times [\nabla' G(\boldsymbol{r}, \boldsymbol{r'})] \mathrm{d}S, \tag{4.3.5}$$

where $\boldsymbol{J}(r')$ represents the surface current density, $\boldsymbol{H}^i$ the incident magnetic field, $\hat{n}$ the unit outward normal, $G = e^{-jkR}/4\pi R$ is the free-space Green's function with R as the distance between source point r' and observation point r and $k = \frac{2\pi}{\lambda}$ represents the wave number. Treatment of the $\boldsymbol{\mathcal{L}}_J^H \boldsymbol{f}_n$ operator in (4.3.4) requires the evaluation of integral on the right of (4.3.5). This integral is complicated by the presence of the cross product of the Green's function. The $\nabla' G(\boldsymbol{r}, \boldsymbol{r'})$ can be re-written as

$$\nabla' G(\boldsymbol{r}, \boldsymbol{r'}) = \left(jk + \frac{1}{R}\right) \frac{e^{-jkR}}{4\pi R} \hat{\boldsymbol{R}}, \tag{4.3.6}$$

with $\boldsymbol{R} = \boldsymbol{r} - \boldsymbol{r'}$ and $\hat{\boldsymbol{R}} = \boldsymbol{R}/R$. The simplification of this term allows the scattered magnetic field integral to be written as

$$\boldsymbol{H}^s(\boldsymbol{r}) = -\frac{1}{4\pi} \int \left(jk + \frac{1}{R}\right) \hat{\boldsymbol{R}} \times \boldsymbol{J}(\boldsymbol{r'}) \frac{e^{-jkR}}{4\pi R} \mathrm{d}S. \tag{4.3.7}$$

When the surface current is expanded using the RWG basis functions of (4.3.2), this integral can be written, considering the contribution from a single triangle, as

$$\boldsymbol{H}_i(\boldsymbol{r}) = \frac{1}{8\pi A} \boldsymbol{R}_i \int \boldsymbol{\rho}_i \frac{(1 + jkR)e^{-jkR}}{R^3} \mathrm{d}S. \tag{4.3.8}$$

This accomplishes the goal of moving the cross product outside of the integral. This equation also facilitates the extraction of the singular behaviour of (4.3.8). The i is a reference to the node of the triangle. This integral can be evaluated using the numerical integration scheme presented in [2]. The integral is then first mapped to simplex coordinates and evaluated using Gaussian quadrature formulas in [101]. It is noted that when the PO and MoM regions are separated in the MoM/PO hybrid, singularity evaluation techniques are not required for the evaluation of this integral since the PO region is always removed from the MoM region. The potential integrals required for this integral will always be evaluated with the source point on a MoM triangle and a field point on a PO triangle. In the case that the MoM and PO overlap, a singularity scheme is required because an MoM element will be sufficiently close to a PO element at the MoM/PO boundary. A singularity extraction scheme is provided in [100] for the interested reader. The MoM/PO hybrid is, therefore, a special case of general EFIE/MFIE hybridisation.

In (4.3.3), the PO current is expressed in terms of the RWG basis functions $\boldsymbol{f}_n$. Even though the basis functions $\boldsymbol{f}_n$ do not form an orthogonal basis, the coefficients of the basis functions, γ_n, can be obtained without solving the system of linear equations. Consider the two triangular elements in Figure 4.4, two unit vectors $\hat{t}_n^{\pm}$ are introduced in the middle of the nth edge at $\boldsymbol{r}_n = \frac{1}{2}(\boldsymbol{a}_{1,n} + \boldsymbol{a}_{2,n})$ perpendicular to the nth edge in the plane of triangles $T_n^{\pm}$. These vectors represent the RWG basis function that is constant normal to the edge between two triangles. f_n has a component of unity across the nth edge and this component vanishes across edges k with $k \neq n$, a point $\boldsymbol{r}_k$ in the middle of the kth edge is obtained

$$\boldsymbol{f}_n(\boldsymbol{r}_k) \cdot \hat{t}_k^{\pm} = \begin{cases} 1 & \text{for } k = n \\ 0 & \text{for } k \neq n \ . \end{cases} \tag{4.3.9}$$

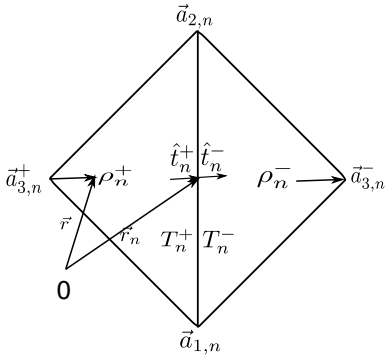

Figure 4.4: Edge n with adjacent triangles T_n^+ and T_n^- [3]

Multiplying both sides of (4.3.3) with $\hat{t}_k^{\pm}$ and adding the resulting two equations leads to

$$\gamma_k = \frac{1}{2}(\hat{t}_k^+ + \hat{t}_k^-) \cdot \boldsymbol{J}^{PO}(r_k) \tag{4.3.10}$$

for $k = N_J^{MoM} + 1 \cdots N_J^{MoM} + N_J^{PO}$. Inserting (4.3.4) into (4.3.10) results in

$$\gamma_k = \tau_{i,k} + \sum_{n=1}^{N_J^{MoM}} \alpha_n \cdot \tau_{J,n,k} \tag{4.3.11}$$

where

$$\tau_{i,k} = (\hat{t}_k^+ + \hat{t}_k^-) \cdot \delta_i \cdot \hat{n} \times \boldsymbol{H}^i \tag{4.3.12}$$

$$\tau_{J,n,k} = (\hat{t}_k^+ + \hat{t}_k^-) \cdot \delta_{J,n} \cdot \hat{n} \times \boldsymbol{\mathcal{L}}_J^H \boldsymbol{f}_n. \tag{4.3.13}$$

Using linear operator notation to represent the Method of Moments formulation and an application of the EFIE to the MoM region yields

$$(\boldsymbol{\mathcal{L}}_J^E \boldsymbol{J}^{MoM})_{tan} + (\boldsymbol{\mathcal{L}}_J^E \boldsymbol{J}^{PO})_{tan} = -\boldsymbol{E}^i_{tan}. \tag{4.3.14}$$

In (4.3.14), two coupling mechanisms between the MoM and the PO region are expressed. The magnetic field due to the currents in the MoM region contributes to the PO current via (4.3.4) and the electric field radiated by the PO currents is expressed in (4.3.14). The PO radiated electric field is taken into account when constraining the EFIE boundary condition.

Inserting (4.3.1) and (4.3.3) with n replaced by k and with γ_k according to (4.3.11) into (4.3.14) results in

$$\sum_{n=1}^{N_J^{MoM}} \alpha_n \cdot \left[(\mathcal{L}_J^E \boldsymbol{f}_n)_{tan} + \sum_{k=N_J^{MoM}+1}^{N_J^{MoM}+N_J^{PO}} \tau_{J,n,k} \cdot (\mathcal{L}_J^E \boldsymbol{f}_k)_{tan} \right]$$
$$= -\boldsymbol{E}_{tan}^i - \sum_{k=N_J^{MoM}+1}^{N_J^{MoM}+N_J^{PO}} \tau_{i,k} \cdot (\mathcal{L}_J^E \boldsymbol{f}_k)_{tan}). \quad (4.3.15)$$

With the use of appropriate weighting functions, (4.3.15) can be transformed into a system of linear equations for the method of moments coefficients α_n. It is worth noting that in (4.3.15), additional calculations have to take place for the coupling of the currents between the MoM and the PO region. The integration is, therefore, time consuming and the $\mathcal{O}(f^6)$ dependence of the MoM is reduced although the PO dependence is still $\mathcal{O}(f^2)$.

4.3.1 Application of the hybrid technique

To illustrate this technique, results are obtained for the perfectly conducting hollow square plate of Figure 4.5 and the two plates of Figure 4.6. The plate has sides of 5λ and the hollow region is a square of side length 1λ. The region around the vicinity of the hollow region is modelled according to the MoM whilst the remainder is modelled according to the PO as illustrated in the figure. The MoM region is 1λ in size from the edges of the hollow region. The monostatic Radar Cross Section (RCS) of the plate is calculated for an incident field that varies from $\theta_0 = 0°$ to $90°$, in the plane $\phi_0 = 0°$.

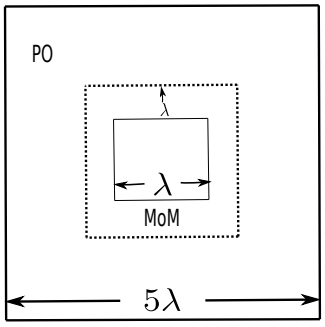

Figure 4.5: Perfectly conducting hollow plate

For the two conducting plates, one plate is modelled using the MoM whilst the other plate is modelled using the PO. This example is chosen to illustrate the coupling between the two regions. The MoM plate is made up of sides 2.5λ whilst the PO plate is made of sides 5λ. The two plates are parallel with the PO plate lying on the xy-plane and the MoM plate elevated along the z-axis. The plates are separated by a distance of $4m$ to ensure that each plate is in the

far field region of the other plate. The monostatic scattering cross section of the plates is obtained for an incident plane wave that is varied from $\theta_0 = 60°$ to 120°, in the plane $\phi_0 = 0°$.

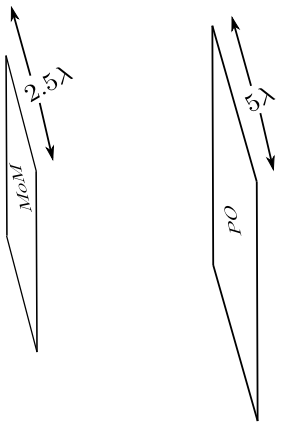

Figure 4.6: Perfectly conducting flat plates

Results for the (RCS) of the plate of Figure 4.5 are presented in Figure 4.7. The results are compared to those of the MoM and PO obtained using *FEKO* for the same setup. There is good agreement between the MoM result and the hybrid technique expanded according to the RWG basis functions. The number of basis functions in the simulation is reduced from 7790 for the conventional method of moments to 2286 for the method of moments region for the hybrid method. 5504 basis functions are used in the PO region. Ultimately, the system of linear equations that has to be solved for the MoM is reduced by a factor of 3. The discrepancy between the MoM and PO result is a result of the erroneous PO currents around the plate edges. The edge effects around the plate are not taken into account by the PO.

Figure 4.8 illustrates the monostatic RCS for the two plate setup. Reference results of the MoM and a hybrid technique implemented in *FEKO* are also presented in this figure. This figure illustrates there is quite a discrepancy between the reference MoM and the hybrid solution. The effects of the PO edge currents on the larger plate are present across the scattered field result. The effect of these currents is noticeable at grazing angles. This error is also compounded by the singularity handling scheme in this technique. The resulting scattered field is also not symmetrical because the field is first incident on the PO plate and then finally on the MoM plate.

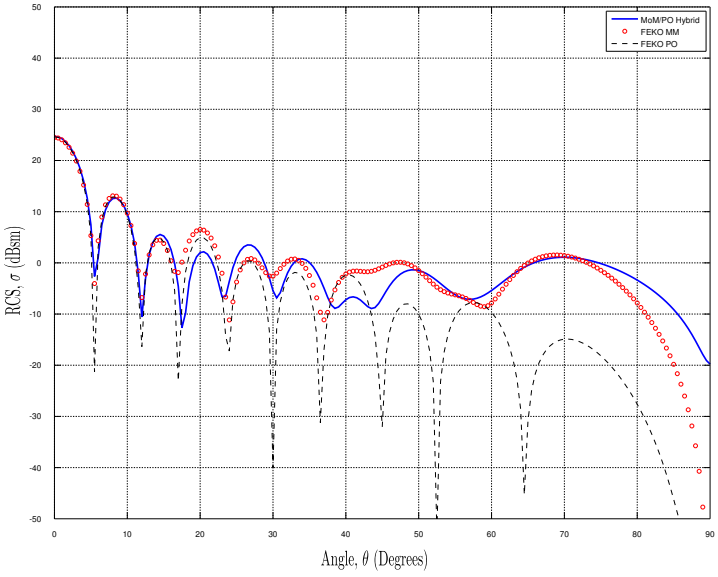

Figure 4.7: Monostatic RCS for the 5λ flat plate with 1λ hollow region

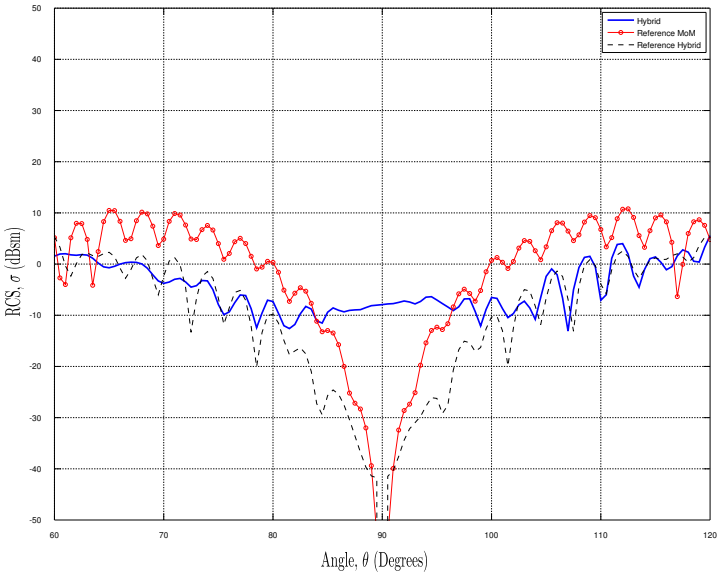

Figure 4.8: Monostatic RCS for the two plate setup

4.4 Incorporation of large element PO through current phase interpolation

The current in the MoM/PO hybrid method is modelled using the RWG basis functions. For these functions, the surface divergence can be determined

analytically. These functions are also free of fictitious charges. A drawback of these functions is the inability to represent any arbitrary linear current distribution on two connected triangles because each base has one vector direction. The functions also do not model phase and this restricts triangle edge length size to the widely accepted $\lambda/10$ in order to accurately sample phase variations.

For a scatterer with large, smooth surfaces, the PO portion of the hybrid method can be modelled using large triangular edge elements. This is achieved by incorporating asymptotic solutions to predict the rapid phase dependence of the unknown current distribution. This leaves a slowly varying residual function that can be represented by a coarse density of unknowns. This is aking to an arbitrary field incident on a planar surface, where the phase of the induced current on the surface can be approximated from the phase of the incident field. For the RWG basis functions, a linear phase term can be added to the functions following the formulation in [102]. The advantage of this new linearly-phased RWG (LP-RWG) function is that it allows the dominant phase variation of the current to be included in the functions; thereby allowing the use of fewer unknowns to represent the slowly varying residual current. The phase dependence of this basis function is determined from a combination of a PO current and the Fourier spectrum of a low frequency MoM solution.

The LP-RWG basis function is defined on a pair of adjacent triangular faces $T_n^{\pm}$, using the same notation as in [2], as

$$f(n) = \begin{cases} \Lambda_n^+(\boldsymbol{r}) e^{-j\boldsymbol{k}_n \cdot (\boldsymbol{\rho}_n^+ - \boldsymbol{\rho}_{nc}^+)}, & \boldsymbol{r} \text{ in } T_n^+ \\ \Lambda_n^-(\boldsymbol{r}) e^{-j\boldsymbol{k}_n \cdot (\boldsymbol{\rho}_n^- - \boldsymbol{\rho}_{nc}^-)}, & \boldsymbol{r} \text{ in } T_n^- \\ 0, & \text{otherwise,} \end{cases} \tag{4.4.1}$$

where $\Lambda_n^{\pm}$ are the normal RWG vector basis functions given by

$$\Lambda_n^{\pm}(\boldsymbol{r}) = \begin{cases} \frac{l_n}{2A_n^+} \boldsymbol{\rho}_n^+, & \boldsymbol{r} \text{ in } T_n^+ \\ \frac{l_n}{2A_n^-} \boldsymbol{\rho}_n^-, & \boldsymbol{r} \text{ in } T_n^- \\ 0, & \text{otherwise.} \end{cases} \tag{4.4.2}$$

The geometrical parameters of this new basis function, $f(n)$ are illustrated in Figure 4.9. l_n represents the length of the common edge, $A_n^{\pm}$ the area of the triangles $T_n^{\pm}$, $\boldsymbol{\rho}_n^{\pm}$ is the vector from the free vertex of triangles $T_n^{\pm}$ to points $\boldsymbol{r}$ on the triangles and $\boldsymbol{\rho}_{nc}^{\pm}$ is the vector from the free vertex to the mid-point of the common edge. The vector $\boldsymbol{k}$ is the vector wave number associated with the current density phase on the function. Since the additional term on RWG functions is an approximate function for the phase of the current induced by the incident field, the direction of $\boldsymbol{k}$ must be chosen to be in the direction of current flow. In this particular instance, this is in the dirction of the incident field i.e. perpendicular to the free edge between two triangles directed from the positive triangle to the negative triangle.

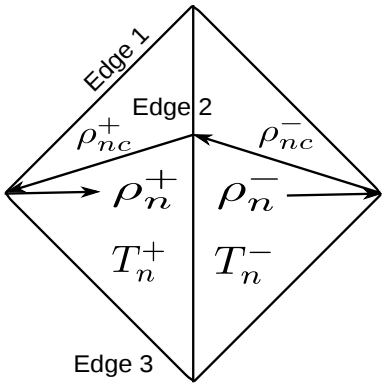

Figure 4.9: The LP-RWG basis function on a common edge between triangles T_n^+ and T_n^-

The first term in the LP-RWG basis function is the conventional RWG basis function. This function provides a linear distribution for the current and also represents its polarisation. The exponential term provides a progressive linear variation of the current density, given by the vector wave number $\boldsymbol{k}_n$. This term assumes the current is modelled by a function in space and the phase of the current is sampled at equal intervals.

The divergence of the basis function, which is also proportional to the surface charge density distribution, is given by

$$\nabla_s \cdot f(n) = \begin{cases} \frac{l_n e^{-j\boldsymbol{k}_n\cdot(\boldsymbol{\rho}_n^+ - \boldsymbol{\rho}_{nc}^+)}}{A_n^+}(1 - j\frac{\boldsymbol{k}_n\cdot\boldsymbol{\rho}_n^+}{2}), & \boldsymbol{r} \text{ in } T_n^+ \\ \frac{l_n e^{-j\boldsymbol{k}_n\cdot(\boldsymbol{\rho}_n^- - \boldsymbol{\rho}_{nc}^-)}}{A_n^-}(1 - j\frac{\underline{\mathrm{k}}_n\cdot\boldsymbol{\rho}_n^-}{2}), & \boldsymbol{r} \text{ in } T_n^- \\ \mathbf{0}, & \text{otherwise.} \end{cases} \tag{4.4.3}$$

The LP-RWG basis function maintains the desirables properties of the original RWG basis function. The current is continuous across the edge connecting two triangles and the net charge associated with the function is zero. The additional linear phase term added to the RWG function only ensures that the phase of the current is sampled at regular intervals and hence the physical properties of the RWG function are not changed. This effectively ensures the fulfilment of the continuity equation without the presence of line charges.

4.4.1 The use of LP-RWG functions in the MoM/PO hybrid

In order to make use of the advantages offered by the LP-RWG basis function, it is incorporated into the MoM/PO hybrid method presented earlier in section 4.3. For large, smooth regions of the surface S, the current shall be expanded according to the LP-RWG basis functions in order to allow the use of larger triangular elements. The surface, S, can be divided into a MoM re-

gion where the current is modelled according to the ordinary RWG functions (4.3.2). The rest of S is modelled according to the PO.

In the portions of S that are modelled with the PO, the surface is further subdivided into a portion that is modelled with the ordinary RWG functions (RWG-PO) in (4.3.2) and a portion modelled with the LP-RWG functions (LP-RWG-PO) in (4.4.1). The subdivision of the PO region ensures a gradual transition between the MoM and the PO region. This, in turn, ensures the continuity of current for neighbouring triangular elements close to the MoM region. In the region surrounding the MoM, the current is modelled with the RWG-PO functions and the LP-RWG-PO functions are used further from this region. The size of triangular mesh elements will increase with increasing distance from the MoM region. Following the notation in [63], the RWG-PO region is designated PO_1 and the LP-RWG-PO region is designated PO_2. This procedure reduces the amount of unknowns that are usually required for the PO region, effectively extending the class of problems the hybrid can be applied to.

In the LP-RWG-PO region, the current is modelled by substituting (4.4.1) into (4.3.3), as

$$\boldsymbol{J}^{PO} = \sum_{n=1}^{N_{PO_{2tot}}} \gamma_n \cdot \boldsymbol{f}_n e^{-j\boldsymbol{k}_n \cdot (\boldsymbol{\rho}_n^{\pm} - \boldsymbol{\rho}_{nc}^{\pm})}, \tag{4.4.4}$$

where $N_{PO_{2tot}}$ is the number of the degrees of freedom, free common edges between two triangles, in the PO_2 region. Due to the fact that larger elements are employed in the PO_2 region, the sampled current phase will be approximately continuous. In the PO_2 region, the current will now be

$$\begin{aligned} \boldsymbol{J}^{PO_2}(r) = {} & 2\delta_i \cdot \hat{n} \times \boldsymbol{H}^i(r) \\ & + \sum_{n=1}^{N_J^{MoM}} 2\alpha_n \delta_{J,n} \cdot \hat{n} \times \boldsymbol{\mathcal{L}}_J^H \boldsymbol{f}_n, \end{aligned} \tag{4.4.5}$$

where the first term represents the PO current due to the incident field and the second term represents the PO current due to the currents in the MoM region. For the PO_1 region, the current is given by (4.3.4). The coefficients δ_i, $\delta_{J,n}$ account for shadowing effects.

Using the same procedure as in section 4.3, the PO_2 coefficients are determined without solving a system of linear equations. The two unit vectors $\hat{t}_n^{\pm}$ are introduced in the PO_2 region at the middle of the nth edge. These unit vectors are again perpendicular to the nth edge and lie in the plane of the triangles $T_n^{\pm}$. The direction of the unit vectors is chosen in accordance with that of the current. Due to the similarity of the LP-RWG function to the RWG function, $\boldsymbol{f}_n e^{-j\boldsymbol{k}_n \cdot (\boldsymbol{\rho}_n^{\pm} - \boldsymbol{\rho}_{nc}^{\pm})}$ will now have a normal component of unity across the nth edge that vanishes across edges a in the PO_2 region as

$$\boldsymbol{f}_n e^{-j\boldsymbol{k}_n\cdot(\boldsymbol{\rho}_n^{\pm}-\boldsymbol{\rho}_{nc}^{\pm})}(\boldsymbol{r}_k)\cdot\hat{t}_k^{\pm}=\begin{cases}1 & \text{for } a=n\\ 0 & \text{for } a\neq n\end{cases}, \tag{4.4.6}$$

multiplying both sides of (4.4.5) with $\hat{t}_a^{\pm}$ results in (4.3.10), for k replaced by a. The unknown coefficients in the PO_2 region can now be obtained with the use of (4.3.11). Applying the surface EFIE to the MoM region will now result in

$$(\mathcal{L}_J^E\boldsymbol{J}^{MoM})_{tan}+(\mathcal{L}_J^E\boldsymbol{J}^{PO_1})_{tan}+(\mathcal{L}_J^E\boldsymbol{J}^{PO_2})_{tan}=-\boldsymbol{E}_{tan}^i. \tag{4.4.7}$$

In this new equation, four different coupling mechanisms can be found. The currents in the MoM region contribute to the currents in the PO_1 and PO_2 regions. The currents in the PO_1 and PO_2 regions similarly contribute to the currents in the MoM region through the potential integrals. The advantage of this new hybrid MoM/PO is that the number of unknowns is further reduced by the employment of large triangular elements in the PO region. The solution of the unknowns in the MoM region are now obtained through the closed form equation

$$\begin{aligned}\sum_{n=1}^{N_J^{MoM}}\alpha_n\cdot\Bigg[&(\mathcal{L}_J^E\boldsymbol{f}_n)_{tan}+\sum_{k=N_J^{MoM}+1}^{N_J^{MoM}+N_J^{PO_1}}\tau_{J,n,k}\cdot(\mathcal{L}_J^E\boldsymbol{f}_k)_{tan}\\&+\sum_{a=N_J^{MoM}+1}^{N_J^{MoM}+N_J^{PO_2}}\tau_{J,n,a}\cdot(\mathcal{L}_J^E\boldsymbol{f}_a e^{-j\boldsymbol{k}_a\cdot(\boldsymbol{\rho}_a^{\pm}-\boldsymbol{\rho}_{ac}^{\pm})})_{tan}\Bigg]\\&=-\boldsymbol{E}_{tan}^i-\sum_{k=N_J^{MoM}+1}^{N_J^{MoM}+N_J^{PO_1}}\tau_{i,k}\cdot(\mathcal{L}_J^E\boldsymbol{f}_k)_{tan}\\&-\sum_{k=N_J^{MoM}+1}^{N_J^{MoM}+N_J^{PO_2}}\tau_{i,a}\cdot(\mathcal{L}_J^E\boldsymbol{f}_a e^{-j\boldsymbol{k}_a\cdot(\boldsymbol{\rho}_a^{\pm}-\boldsymbol{\rho}_{ac}^{\pm})})_{tan}.\end{aligned} \tag{4.4.8}$$

By applying the appropriate weighting functions, the unknown MoM coefficients can be solved with a system of matrix equations. The coefficients of the PO region can then be obtained via a straightforward substitution of the MoM coefficients. This efficient hybrid method allows the application of the MoM/PO hybrid to electrically very large problems due to the removal of the requirement to mesh the PO region at $\lambda/10$.

4.5 Conclusion

In this chapter, the hybrid MoM/PO was introduced and extended to allow the use of large triangular mesh elements. The MoM/PO hybrid allows a reduction in the size of unknowns that are required for the solution of a system of linear equations in the MoM. The MoM/PO hybrid requires the use of the conventional $\lambda/10$ triangular mesh elements to sample the phase of the current.

The MoM/PO hybrid was extended by incorporating a linear phase term into the conventional RWG basis functions. The improved hybrid allows the use of larger triangular elements, reducing the requirement for high meshing resolution.

In the following chapter, numerical results are presented for the improved hybrid MoM/PO method.

Chapter 5

Numerical Results

5.1 Introduction

In the previous chapter, an improved hybrid MoM/PO method was presented. This was developed by including a linear phase term, in the standard RWG basis function, to sample the current. This new technique allows the incorporation of large triangular elements into the MoM/PO hybrid.

In this chapter, numerical results are presented for the improved MoM/PO hybrid for selected geometries under plane wave illumination. The aim of this chapter is to illustrate the efficiency and accuracy of the improved hybrid technique. As a result, three geometries are to be considered in this chapter; a conducting flat plate, a conducting plate with a cavity and a dihedral corner reflector. The flat plate is chosen to exhibit edge diffraction, the flat with the cavity is chosen as a problem that contains some complex geometry elements and the dihedral corner reflector demonstrates the coupling calculation of the hybrid. For all the results considered in this section, reference solutions are simulated using *FEKO*. Monostatic RCS results are presented for all the test cases for a scan of the incident wave from $\theta_0 = 0^\circ$ to $\theta_0 = 90^\circ$, with a fixed $\phi_0 = 0^\circ$.

5.2 Flat plate

The first example considered for this work is the perfectly conducting flat plate in Figure 5.1. The largest mesh element of the plate is varied in order to evaluate the effectiveness of the improved hybrid technique. This results in three mesh setups for the flat plate. Square plates of lengths 5λ and 10λ, respectively, are considered.

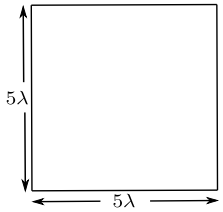

Figure 5.1: Perfectly conducting $5\lambda \times 5\lambda$ flat plate

5.2.1 5λ Flat plate

The surface current density distribution on the plate in Figure 5.2 for a normally incident plane wave is shown in Figure 5.3 for both the improved hybrid and the normal hybrid technique.

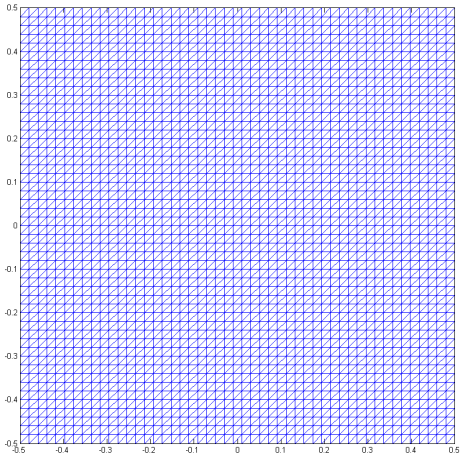

Figure 5.2: Perfectly conducting $5\lambda \times 5\lambda$ flat plate with $\lambda/10$ triangular mesh edge length

The uniform triangular mesh elements on the plate have a anedge length of $\lambda/10$. For both hybrid techniques, the MoM region is set to a size of 1λ from the edges of the plate. At the edges of the plate, the incident field will experience diffraction and the PO formulation does not account for this phenomenon. In the improved hybrid technique, the PO_1 region is set to size of $\lambda/2$ from the edge of the MoM region. The current on the remaining portion, PO_2, of the plate is modelled using the LP-RWG functions.

Figure 5.3 illustrates good agreement between the improved hybrid and normal hybrid currents. The slight variations in current between the two techniques can be attributed to the integration scheme used with the linear phase term in the improved hybrid. The integration scheme used in this technique is

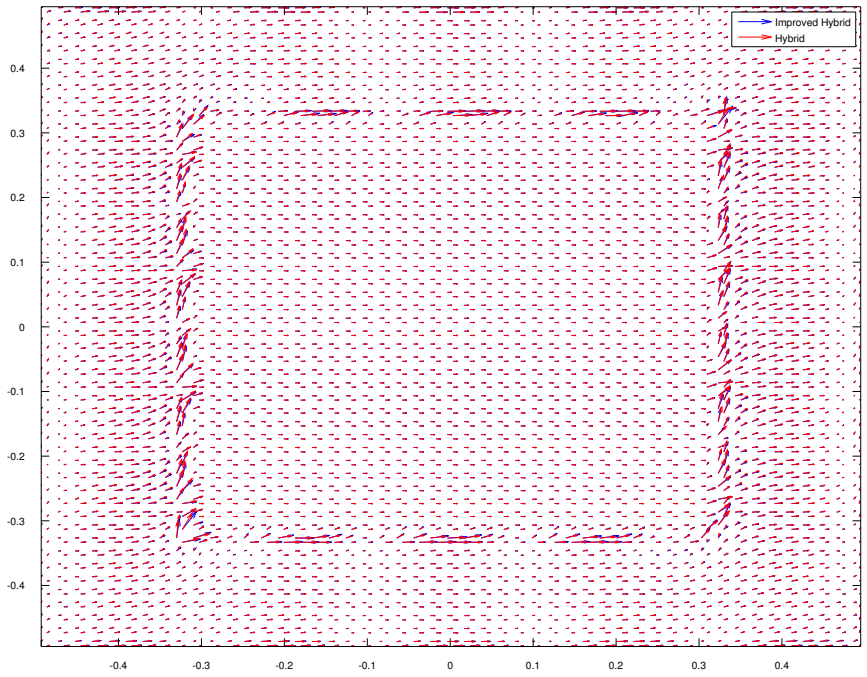

Figure 5.3: Surface current density distribution on 5λ flat plate

the simple scheme implemented in [2]. For the improved hybrid, the new integral contains the phase term which is effectively multiplied with the Green's function to results in a "modified" Green's function.

At the edges of the plate, treated with the MoM, charge accumulates and the normal component of current is zero. On the boundary between the MoM and the PO, charges from the MoM region appear to accumulate on the boundary. This effect is not present in the boundary between the PO regions in the improved hybrid. The use of RWG basis functions ensures that the normal component of current is continuous across this boundary. The tangential component of current is, however, not continuous at either side of this boundary and the magnitude of the current on triangles lying on each side of this boundary is not uniform. The sinusoidal variation of the current is not present in the region treated with the PO as in the region treated with the MoM. It is noted that the PO is an approximate technique and results in an average current value over a mesh element. The variations on the current in the MoM region are due to the mutual interactions between all elements in the MoM.

The Radar Cross Section (RCS) of the plate is considered for both uniform and non-uniform triangular mesh elements on the plate. For all configurations, the minimum triangular edge length on the plate is $\lambda/10$ over the MoM region. The RCS for the uniform mesh in Figure 5.2 with a triangular edge

length set at $\lambda/10$ is illustrated in Figure 5.4. Good agreement is observed

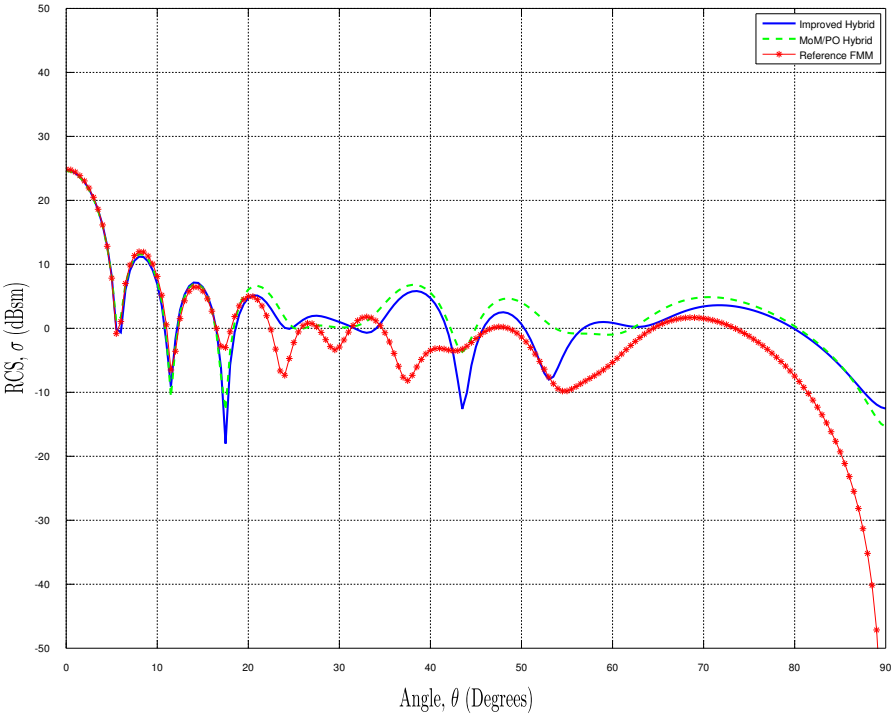

Figure 5.4: Monostatic radar cross section of 5λ plate with $\lambda/10$ largest triangular edge length

between the reference MoM solution and the dominant component of the RCS for both the MoM/PO and the improved hybrid. The results of both the MoM/PO and improved hybrid differ from the reference MoM solution away from normal incidence. The lobes of the scattering pattern, for both hybrid techniques, occur at different angles in comparison to the reference solution. These misplaced lobes are a result of the incorrect current values between the MoM and PO regions. The PO portion of the hybrid is also incorrect away from normal incidence. The difference in result between the improved hybrid and the MoM/PO hybrid can be attributed to the integration scheme of the new linear phase RWG element.

Characteristics of the two techniques are summarised in Table 5.1. The conventional MoM and the hybrid MoM/PO require the use of 7251 RWG basis functions on the surface of the flat plate. The improved MoM/PO hybrid only requires the use of 5664 RWG basis functions (MoM and PO_1), a 20% reduction in the use of RWG functions. This shows the reduction in mesh storage that can be achieved with the use of hybrid techniques. This can be particularly valuable for very large geometries.

Table 5.1: Unknowns and cost for uniform $\lambda/10$ triangular edge length mesh

Method	N_{MoM}	N_{PO_1}	N_{PO_2}	Matrix Memory(MB)
MoM	7251	–	–	420
MoM/PO	4338	2913	–	301
Improved MoM/PO	4338	1326	1587	301

The RCS of the non-uniform mesh of the plate in Figure 5.5, with largest triangular mesh edge length $\lambda/6$, is illustrated in Figure 5.6. The MoM region is again set at the outer edges of the plate. In the PO region, the mesh is gradually increased in size.

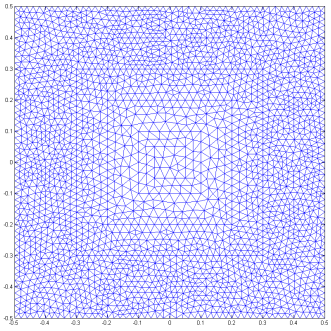

Figure 5.5: Perfectly conducting $5\lambda \times 5\lambda$ flat plate with $\lambda/6$ largest triangular edge length

Good agreement is observed between the reference MoM solution and both hybrid techniques for the dominant component, as expected. It is noted, however, that the error between the reference result and both hybrid techniques increases away from normal incidence. For the RWG function, the phase is assumed to be constant and therefore the phase is more accurately modelled with smaller mesh elements. As the mesh size is increased, the phase is no longer modelled correctly. This is worse at angles away from normal incidence because the phase of the current is no longer continuous over the plate. For the improved hybrid, the phase is modelled incorrectly away from normal incidence. This suggests that the phase of the current between two adjacent elements is not continuous. As the plate is rotated, the phase of the current varies considerably and more integration points are required to approximate the phase integral correctly. For these simulations, a six point Gaussain quadrature scheme is used. To approximate the phase corretly then, finer elements or more accurate integration schemes are required as the plate is rotated.

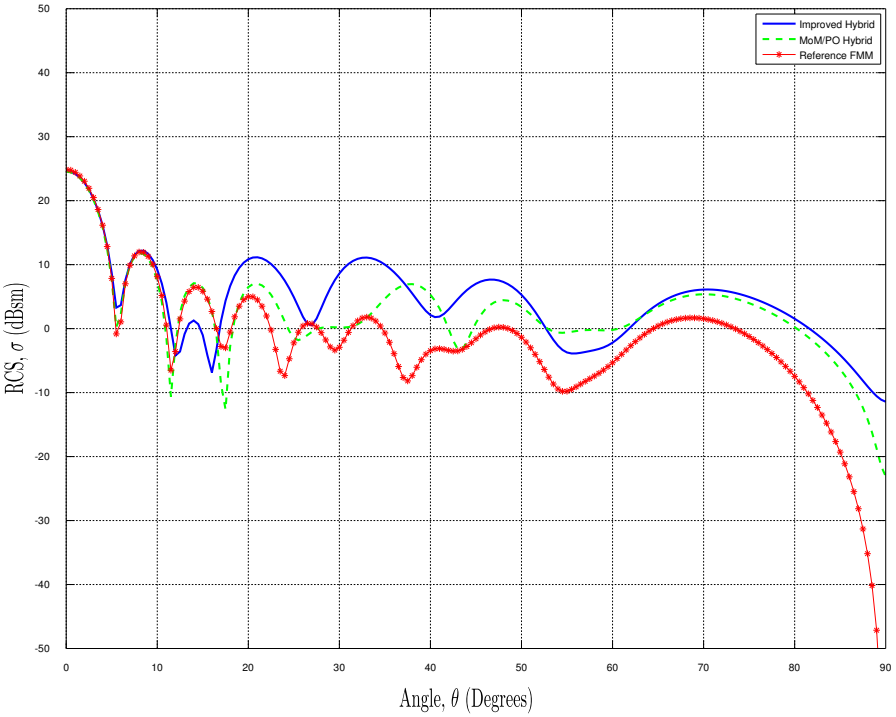

Figure 5.6: Monostatic radar cross section of 5λ plate with $\lambda/6$ largest triangular edge length

Characteristics of the two techniques are summarised in Table 5.2. The conventional MoM requires the use of 7577 RWG functions, the MoM/PO 7577 RWG functions, and the improved MoM/PO 6482 RWG functions. This translates to a 14% reduction in RWG functions. Note that the non-uniform mesh in Figure 5.5, however, has more elements than the mesh in Figure 5.2. This suggests efficient mesh generation algorithms are required to realise the full power of the improved hybrid technique.

Table 5.2: Unknowns and cost for non-uniform mesh with $\lambda/6$ largest triangular edge length

Method	N_{MoM}	N_{PO_1}	N_{PO_2}	Matrix Memory(MB)
MoM	7577	–	–	459
MoM/PO	5206	2371	–	433
Improved MoM/PO	5206	1276	1095	433

The RCS of the plate, with a non-uniform mesh, in Figure 5.7 is illustrated in Figure 5.8. This mesh is generated with the largest triangular edge length set to $\lambda/2$.

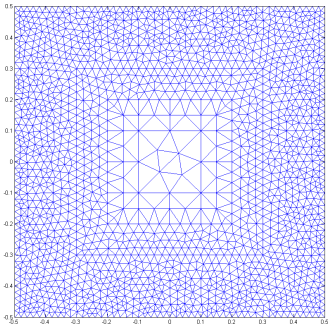

Figure 5.7: Perfectly conducting $5\lambda \times 5\lambda$ flat plate with $\lambda/2$ largest triangular edge length

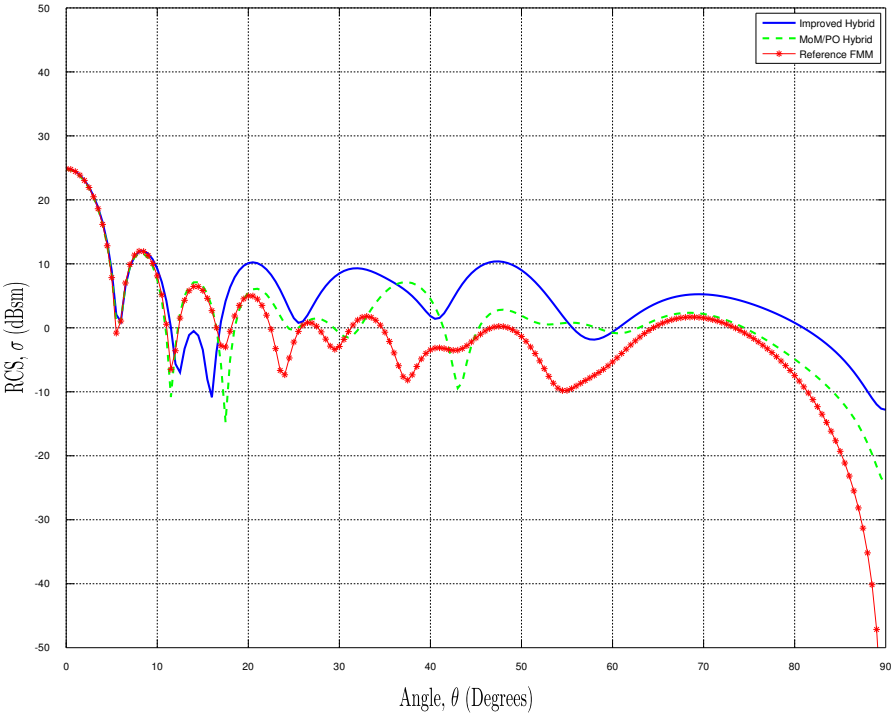

Figure 5.8: Monostatic radar cross section of 5λ plate with $\lambda/2$ largest triangular edge length

Good agreement is observed between the reference MoM solution and both hybrid techniques for the dominant component of the scattered field. Again, the results of the hybrid techniques, however, degrade considerably as the largest triangular edge length is increased. The increase in the scattered field away from normal incidence for the improved technique shows that the approximated phase is no longer valid.

Characteristics of the two techniques are illustrated in Table 5.3. The conventional MoM and the hybrid MoM/PO require 5417 RWG functions while the improved hybrid method requires 4889 RWG basis functions. This translates to a 10% reduction in the number of RWG functions. This table suggests that the value of the hybrid can be realised in the reduction in the number of matrix and mesh elements as opposed to the two mesh configurations already presented for this setup. This advantage, however, needs to be considered against the loss in accuracy of the hybrid.

Table 5.3: Unknowns and cost for non-uniform mesh with $\lambda/2$ largest triangular edge length

Method	N_{MoM}	N_{PO_1}	N_{PO_2}	Matrix Memory(MB)
MoM	5417	–	–	234
MoM/PO	4080	1337	–	133
Improved MoM/PO	4080	819	518	133

Figure 5.9 and Figure 5.10 illustrate the accuracy of the the presented mesh resolutions for the improved hybrid and normal hybrid respectively. Figure 5.9 illustrates that the accuracy of the improved hybrid varies considerably. Away from normal incidence, the true phase of the current is sampled incorrectly. The phase between two triangular elements is not continuous. This is due to the approximate integration scheme used in this technique. The six point Gaussian scheme is used as the plate is rotated. Also, the PO currents are invalid for angles away from normal incidence. Figure 5.10 illustrates the phase of the current is also sampled incorrectly with the RWG functions as the mesh of the largest triangular element is increased. These images suggest that both hybrid techniques are valid up to 15° away from normal incidence.

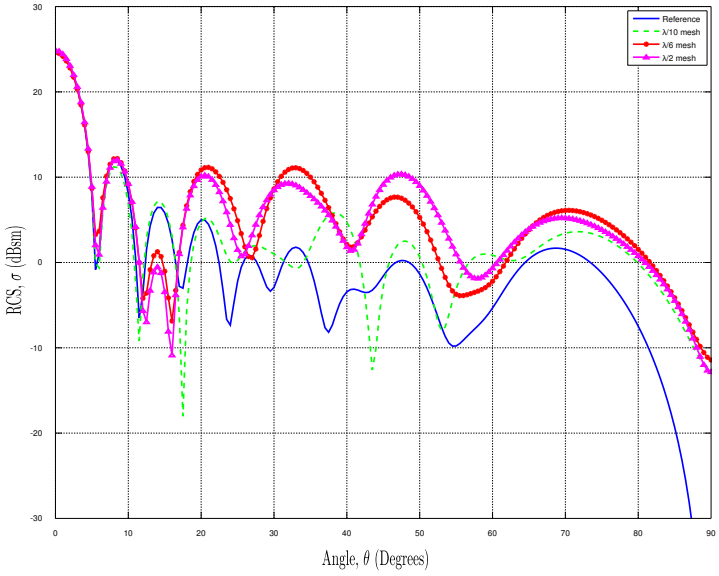

Figure 5.9: Monostatic radar cross section accuracy for linear phase formulation

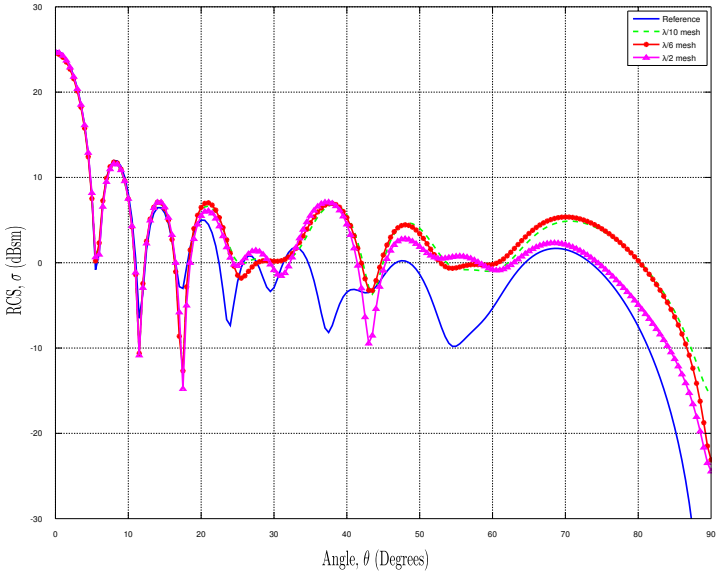

Figure 5.10: Monostatic radar cross section accuracy for hybrid formulation

5.2.2 10λ Flat plate

The lengths of the sides of the square flat plate are increased to 10λ. In all the cases considered, the MoM region is set to $\lambda/2$ from the edges of the flat plate. For all simulations conducted with the improved hybrid, the PO_2 region is set to a size of λ from the MoM region.

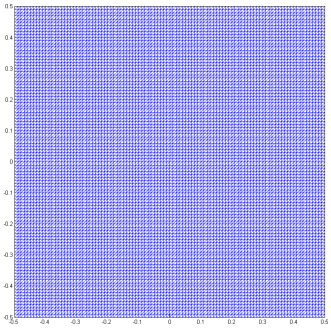

Figure 5.11: Perfectly conducting $10\lambda \times 10\lambda$ flat plate with $\lambda/10$ triangular mesh edge length

The RCS of the plate in Figure 5.11, with uniform mesh of triangular edge length $\lambda/10$, is shown in Figure 5.12. Good agreement is observed between the reference MoM solution and the dominant component of the RCS for both the MoM/PO and the improved hybrid. Again, the scattered field of both the MoM/PO and improved hybrid differ from the reference MoM solution away from normal incidence. The PO current approximation away from normal incident improves in contrast to the 5λ example presented previously as a result of the increase in accuracy of the PO with increasing electrical size. At grazing angles, there is noticeable difference in the scattered field between the improved hybrid and the normal hybrid. The improved hybrid performs poorly at these incident angles.

Characteristics of the two techniques are summarised in Table 5.4. The conventional MoM and the hybrid MoM/PO require the use of 29800 RWG basis functions on the surface of the flat plate. The improved MoM/PO hybrid only requires the use of 13664 RWG basis functions. This improved technique requires 54% less RWG functions than the original hybrid.

The RCS of the plate in Figure 5.13, with largest triangular mesh edge length $\lambda/6$, is illustrated in Figure 5.14 for both the hybrid and the improved hybrid method. Good agreement is observed between the reference MoM solution and the improved hybrid for the dominant component of scattering.

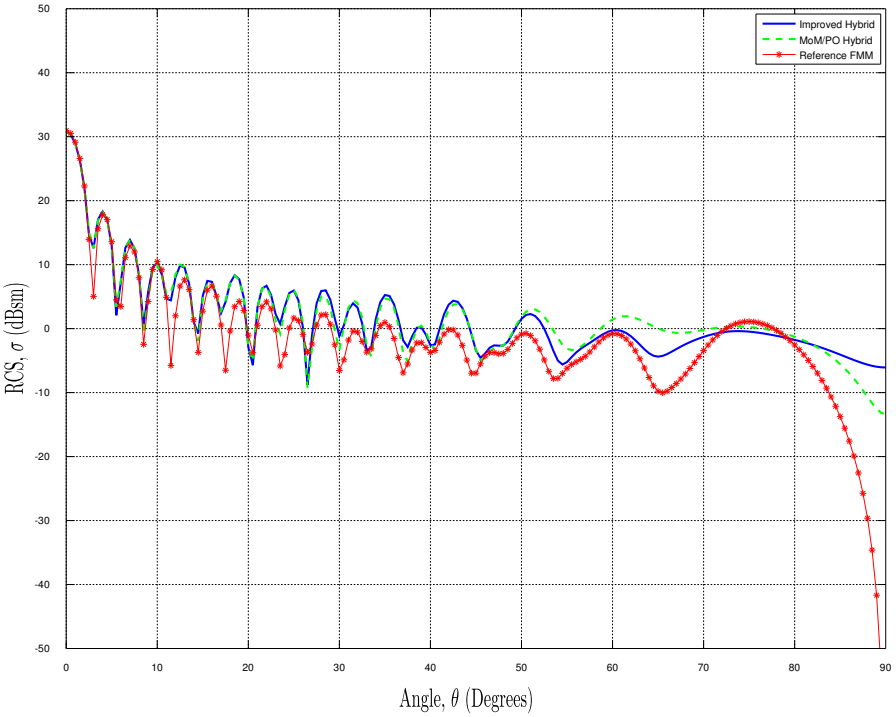

Figure 5.12: Monostatic radar cross section of 10λ plate with $\lambda/10$ largest triangular edge length

Table 5.4: Unknowns and cost for uniform $\lambda/10$ triangular edge length mesh

Method	N_{MoM}	N_{PO_1}	N_{PO_2}	Matrix Memory(MB)
MoM	29800	–	–	7.10×10^3
MoM/PO	4592	25208	–	337
Improved MoM/PO	4592	9072	16136	337

The accuracy of the results degrades away from normal incidence as a result of the PO, as expected. Also, as the mesh elements are increased, the phase of the current in the MoM/PO hybrid is sampled erroneously. The phase of the current in the linear phase basis functions is also sampled incorrectly at angles away from normal incidence. This is a result of the integration schemes used in this formulation. The integral is overestimated in this case.

Characteristics of the two techniques are summarised in Table 5.5. The conventional MoM and the hybrid MoM/PO require the use of 23065 RWG functions. The improved MoM/PO makes use of 14474 RWG functions, 63% of the conventional MoM.

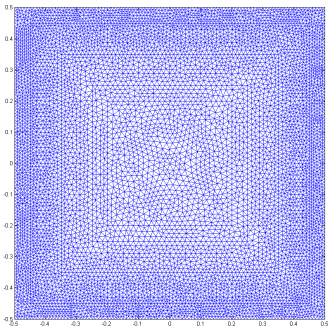

Figure 5.13: Perfectly conducting $10\lambda \times 10\lambda$ flat plate with $\lambda/6$ largest triangular edge length

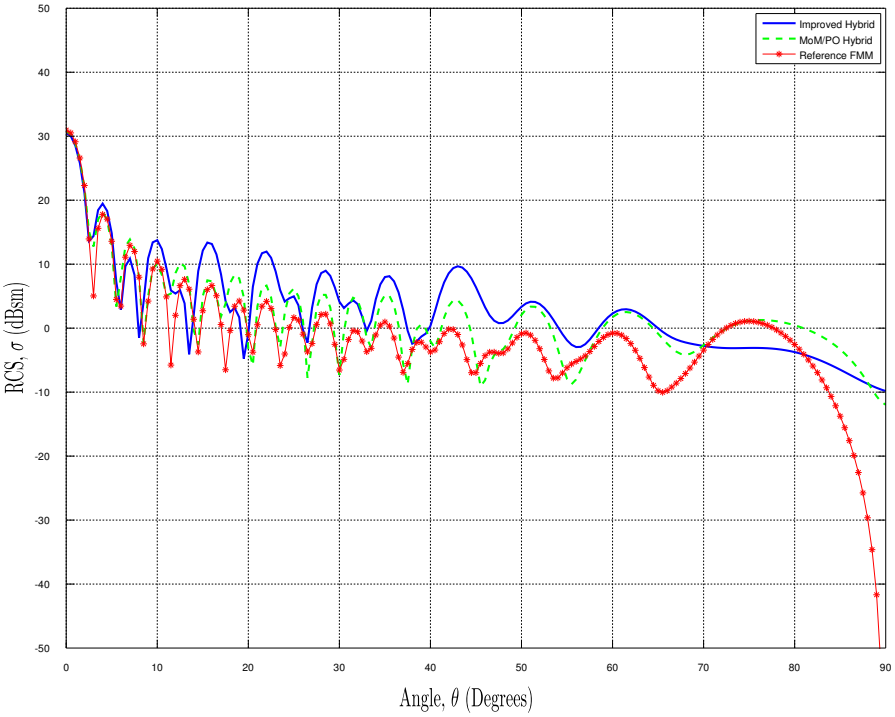

Figure 5.14: Monostatic radar cross section of 10λ plate with $\lambda/6$ largest triangular edge length

The RCS of the plate in Figure 5.15, with largest mesh edge length $\lambda/2$, is illustrated in Figure 5.16. The non-uniform mesh is generated with all the PO elements away from the MoM region on the edges of the plate.

The figure illustrates that good agreement is observed between the reference MoM solution and the improved hybrid technique for the dominant compo-

Table 5.5: Unknowns and cost for non-uniform mesh with $\lambda/6$ largest triangular edge length

Method	N_{MoM}	N_{PO_1}	N_{PO_2}	Matrix Memory(MB)
MoM	23065	–	–	4.25×10^3
MoM/PO	5961	17104	–	568
Improved MoM/PO	5961	8513	8591	568

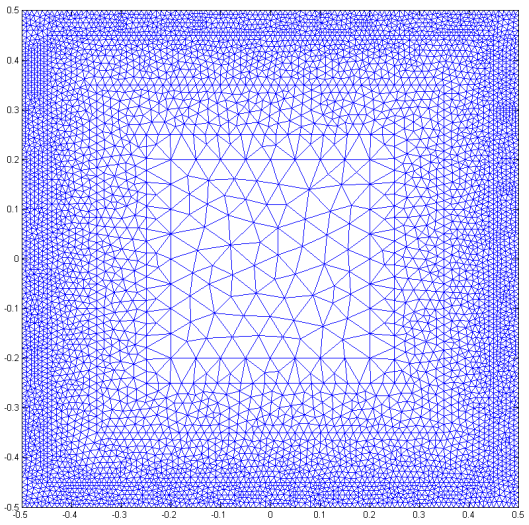

Figure 5.15: Perfectly conducting $10\lambda \times 10\lambda$ flat plate with $\lambda/2$ largest triangular edge length

nent of the scattered field. Again, away from normal incidence the improved hybrid is seen to overestimate the scattered field. At this mesh resolution, the approximated scattered field becomes invalid as the phase of the current is no longer approximated correctly. This effect, coupled with the integration scheme in this technique, accounts for the poor performance of the improved hybrid for this setup. The results for the hybrid MoM/PO also degrade away from normal incidence.

Characteristics of the two techniques are summarised in Table 5.6. The conventional MoM and hybrid MoM/PO require the use of 16327 RWG functions whilst the improved hybrid reduces these functions by 23% to 12514. The computational mesh storage requirements are drastically reduced with this non-uniform mesh. In comparison to the $\lambda/10$ largest mesh element setup, this formulation is more efficient for an approximate answer to the EM solution of the plate.

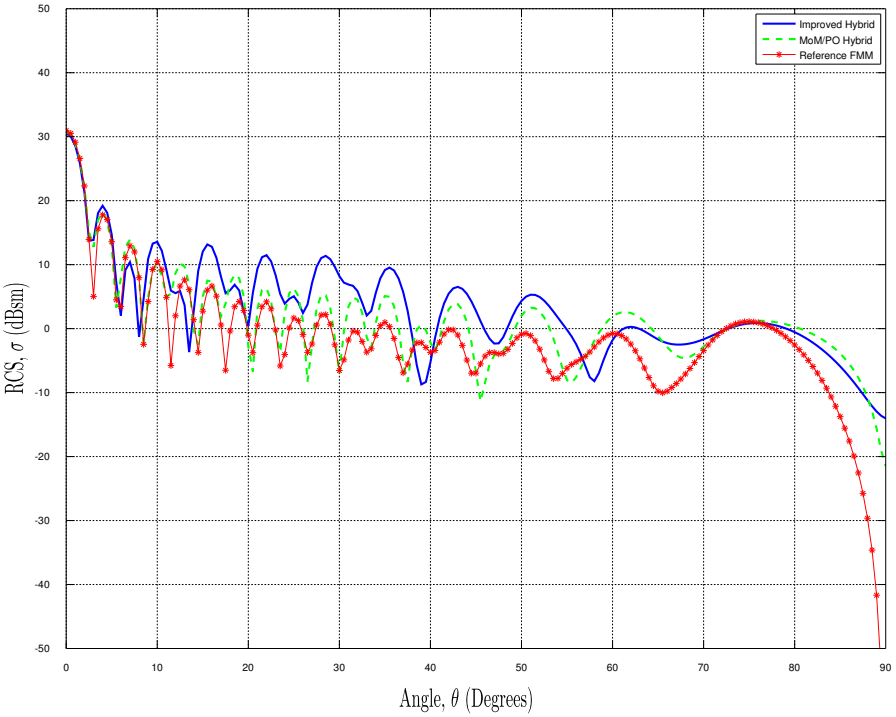

Figure 5.16: Monostatic radar cross section of 10λ plate with $\lambda/2$ largest triangular edge length

Table 5.6: Unknowns and cost for non-uniform mesh with $\lambda/2$ largest triangular edge length

Method	N_{MoM}	N_{PO_1}	N_{PO_2}	Matrix Memory(MB)
MoM	16327	–	–	2.13×10^3
MoM/PO	5987	10340	–	573
Improved MoM/PO	5987	6527	3813	573

The accuracy of the hybrid techniques for the 10λ plate is illustrated in Figure 5.17 and Figure 5.18 for the improved hybrid and original hybrid technique. There is a lot of variation in the improved hybrid results off normal incidence as a result of the incorrect phase of the current. In comparison to the results for the 5λ plate, the improvement in accuracy of the PO can be seen as the frequency of the incident field is increased.

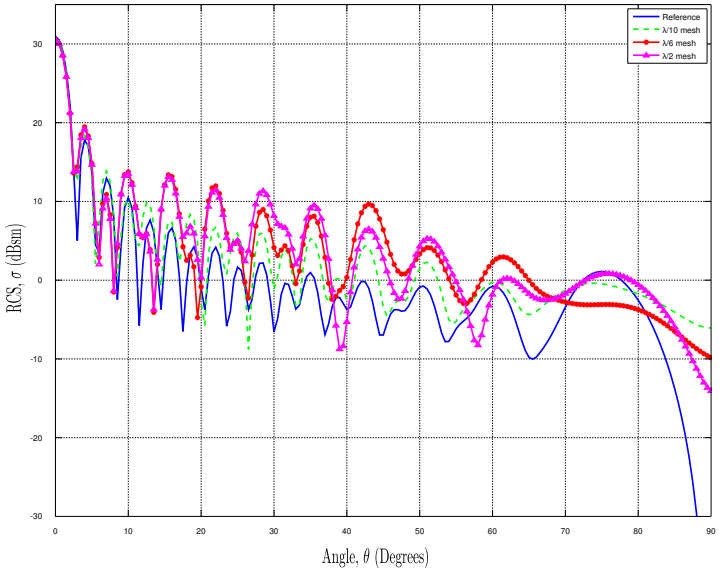

Figure 5.17: Monostatic radar cross section accuracy for linear phase formulation

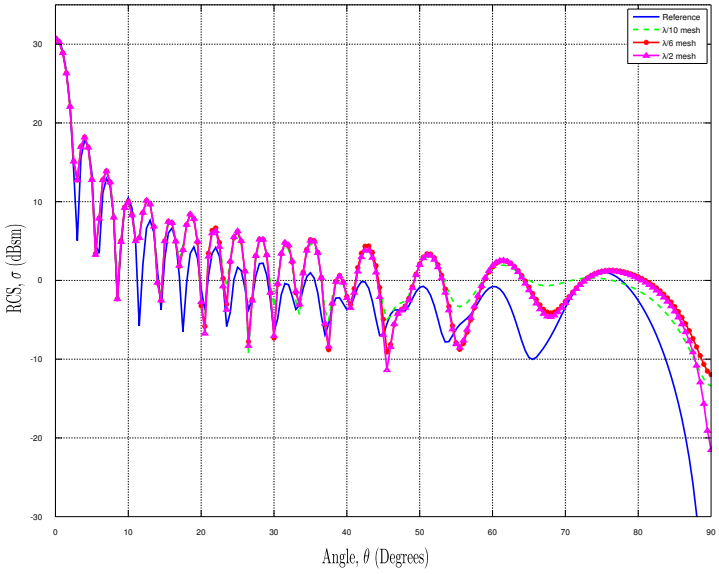

Figure 5.18: Monostatic radar cross section accuracy for hybrid formulation

5.2.3 Summary

Good agreement is achieved for the dominant component of the scattered field using both the hybrid MoM/PO and the improved hybrid. Continuity of the tangential component of current on the boundary between the MoM and PO region is not enforced. This results in differing current values on opposite sides of this boundary. The magnitude of the observed scattered field away from normal incidence is affected by this current on the boundary and distorts the location of the lobes of the scattered field. This is also affected by the fact that the PO formulation is inherently inaccurate for angles away from normal incidence. The inaccurate result improves as the frequency of the incident field is increased.

The hybrid techniques also demonstrate that as the largest edge length of a triangular element is increased in the mesh, the phase of the current is sampled incorrectly. This is compounded by the integration schemes used in the improved hybrid formulation.

The memory required for the storage of the mesh, and by and large computational time is reduced by the hybrid techniques. Memory requirements are reduced due to fewer MoM matrix elements required by both hybrid techniques. This reduction, in effect, reduces the computational time that any given simulation would take to fill the MoM matrix. It is noted, however, that additional calculations are required with the use of the hybrid and in some situations it may be that the hybrid requires more time than the MoM formulation, for example small geometries. The additional calculations in the hybrid occur as a result of (4.3.15).

The number of unknowns can be significantly reduced, depending on the construction of the mesh. This is demonstrated by the 5λ flat plate with largest triangular mesh edge set to $\lambda/2$. The improved hybrid in this case requires the use of 4080 unknowns in the MoM matrix in comparison with the original MoM/PO hybrid which requires the use of 4338 unknowns. It is also shown that the opposite can occur, when increased unknowns are required for the improved hybrid. Efficient mesh generation algorithms, complemented with the improved hybrid, will lead to efficient use of the improved hybrid.

5.3 Flat plate with cavity

The flat plate with a cavity, illustrated in Figure 5.19, is considered in this section. The flat plate has dimensions $10\lambda \times 10\lambda$. The cavity is cubic with dimensions $1\lambda \times 1\lambda \times 0.5\lambda$. This example adds complexity to the flat plate simulated in the previous section. Within the cavity, the incident wave will experience multiple bounces and this effect cannot be solved with the pure PO. This example is chosen to demonstrate a complex, electrically small problem (cavity) within an electrically large area (plate).

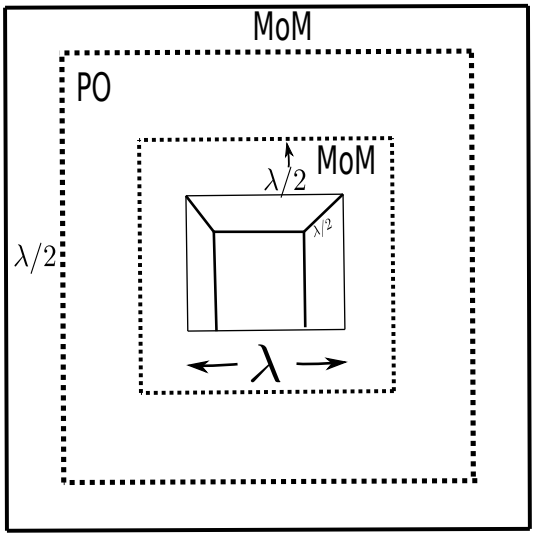

Figure 5.19: Perfectly conducting $10\lambda \times 10\lambda$ plate with cavity

The PO is not suited to obtaining the solution for this problem. The PO will not account for both multiple bounces within the cavity and edge diffraction effects on the plate. The currents within the cavity and on the planar region in the immediate vicinity of the cavity can be modelled with the MoM. The currents on the edges of the plate are also modelled with the MoM whilst the currents on the remaining planar area of the plate are modelled with the PO. Two MoM regions are defined for this problem; the first at $\lambda/2$ from the edges of the cavity and the second at $\lambda/2$ from the edges of the plate as shown in Figure 5.19. This now results in two boundaries between the MoM and PO where there will be a slight jump in the current density. For all the improved hybrid simulations, the PO_1 region is set at 1λ from the MoM region.

Scattering solutions for the plate with the cavity are obtained for differing meshes. Both the uniform and non-uniform mesh sizes that were generated for the flat plate in the previous section are used. The meshes generated for this setup vary from a uniform mesh with triangular edge length $\lambda/10$ to non-uniform meshes with largest triangular edge length $\lambda/6$ and $\lambda/2$ respectively.

The plate of uniform mesh with triangular edge length $\lambda/10$ is shown in Figure 5.20. The RCS of the plate is illustrated in Figure 5.21 using both the hybrid MoM/PO and the improved hybrid technique.

Reasonable agreement is observed for the main lobe of the reference solution and both hybrid techniques. This agreement degrades away from normal incidence. As the incident field is rotated through θ_0, better convergence is now noted between both the original hybrid and the improved hybrid. It is also noted that there are now two boundaries between the MoM and the PO region; the effect of which is noticeable in the displacement of the maxima and minima values of the scattered field in comparison to the reference solution.

Characteristics of the hybrid techniques are summarised in Table 5.7. The

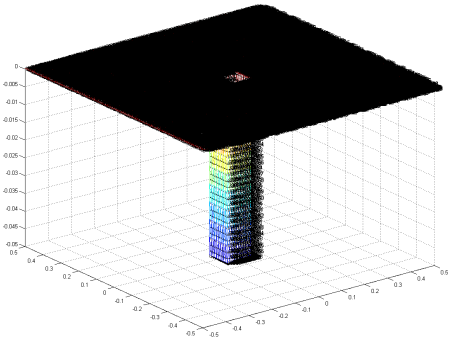

Figure 5.20: Mesh for perfectly conducting $10\lambda \times 10\lambda$ plate with cavity

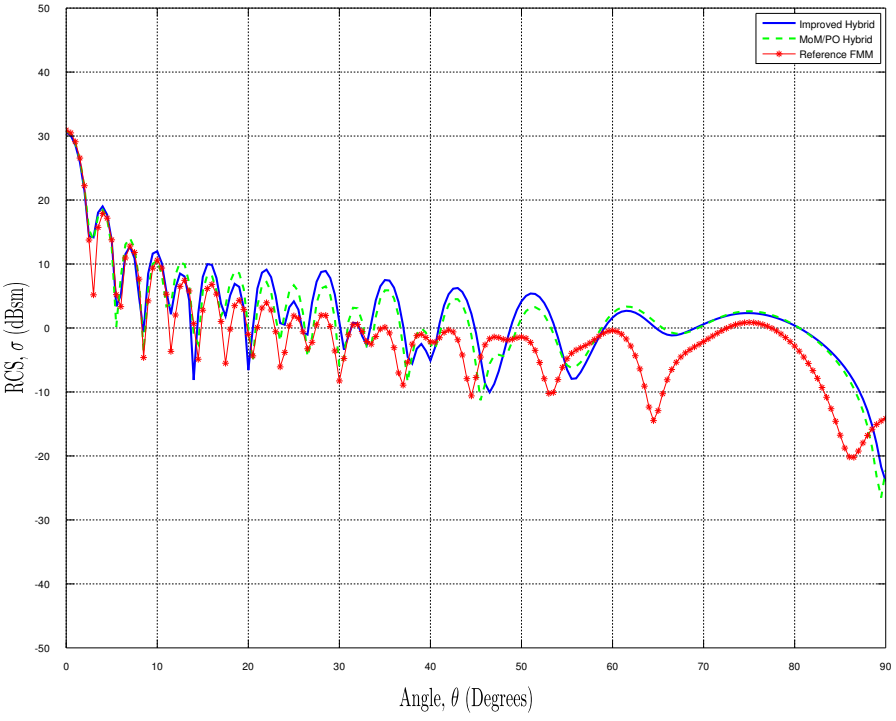

Figure 5.21: Monostatic radar cross section of 10λ plate with $\lambda/10$ largest triangular edge length

conventional MoM and hybrid MoM/PO require the use of 35449 RWG functions whilst the improved hybrid reduces these functions by 31% to 24497. Note that this problem results in a large number of unknowns due to the cavity. Nonetheless, the hybrid techniques are more memory efficient in the solution of this problem.

Table 5.7: Unknowns and cost for uniform $\lambda/10$ triangular edge length mesh

Method	N_{MoM}	N_{PO_1}	N_{PO_2}	Matrix Memory(MB)
MoM	35449	–	–	10.05×10^3
MoM/PO	10073	25376	–	1.62×10^3
Improved MoM/PO	10073	14424	10952	1.62×10^3

The non-uniform mesh of Figure 5.22 with largest triangular edge length $\lambda/6$ is simulated. In comparison to Figure 5.20, only the top view of the plate is displayed to illustrate the mesh elements in the PO region. The RCS of the plate is illustrated in Figure 5.23. Good agreement is observed between the main lobe of the reference solution and the improved hybrid technique. The first null of the scattered field in the hybrid techniques does not occur at the same point as the reference solution due to the additional boundary between the MoM and PO solutions now present. The combination of incorrect current phase effects and poor PO results is observed away from normal incidence. In addition, the hybrid MoM/PO results degrade as the largest mesh element is increased in size due to inaccurate current phase sampling.

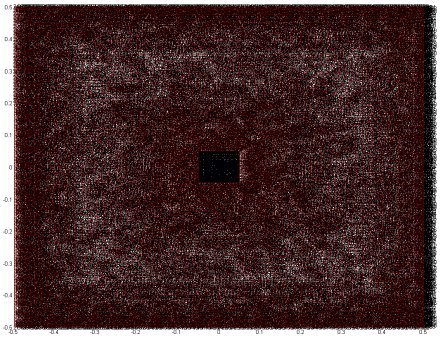

Figure 5.22: Mesh for perfectly conducting $10\lambda \times 10\lambda$ plate with cavity, using $\lambda/6$ largest triangular edge length

Characteristics of the techniques are summarised in Table 5.8. The conventional MoM and hybrid MoM/PO require the use of 20194 RWG functions whilst the improved hybrid reduces these functions by 25% to 15210. The number of unknowns is reduced as the largest mesh element is increased in comparison to the previous example. The memory required for storage of the matrix is also reduced considerably.

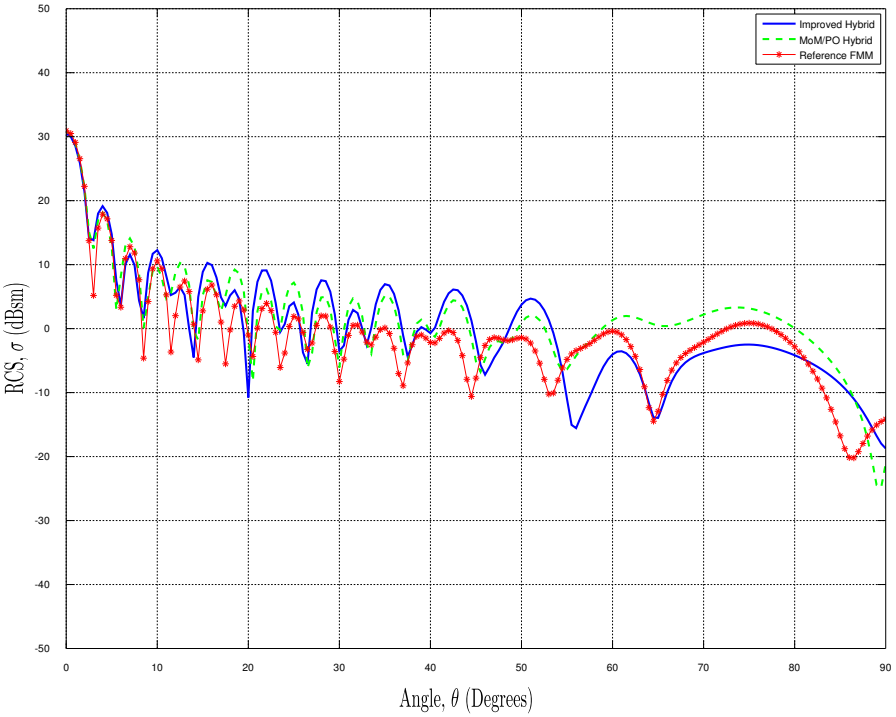

Figure 5.23: Monostatic radar cross section of 10λ plate with $\lambda/6$ largest triangular edge length

Table 5.8: Unknowns and cost for non-uniform mesh with $\lambda/6$ largest triangular edge length mesh

Method	N_{MoM}	N_{PO_1}	N_{PO_2}	Matrix Memory(MB)
MoM	20194	–	–	3.26×10^3
MoM/PO	7560	12634	–	914
Improved MoM/PO	7560	7650	4984	914

The final example considered is the plate with largest triangular mesh edge element set to $\lambda/2$, illustrated in Figure 5.24.

The RCS of the plate is illustrated in Figure 5.25. Again, the effect of the additional MoM/PO boundary is observed at the first null in the scattered field result. Nonetheless, good agreement is again observed for the dominant component of the scattered field. The scattered field results appear to degrade due to the increase in the mesh elements. Poor agreement is again noticeable at all angles away from normal incidence. At grazing incidence, the normal hybrid technique is very poorly behaved because the PO current calculation is incorrect. This suggests the linear phase term samples the current more

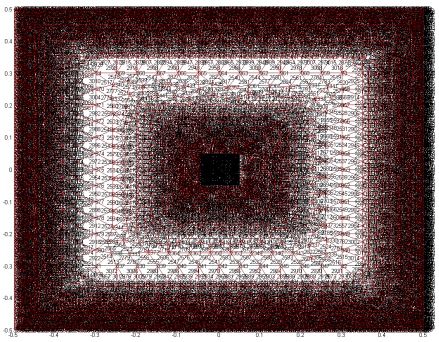

Figure 5.24: Mesh for perfectly conducting $10\lambda \times 10\lambda$ plate with cavity, using $\lambda/2$ largest triangular edge length

accurately at these angles for this particular setup.

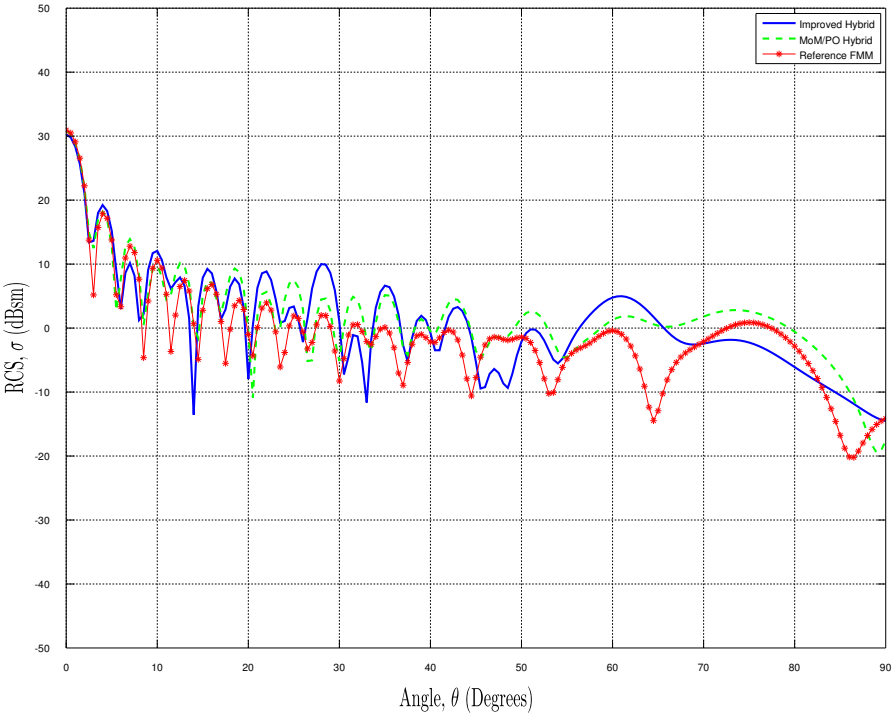

Figure 5.25: Monostatic radar cross section of 10λ plate with $\lambda/2$ largest triangular edge length

Characteristics of the techniques are summarised in Table 5.9. The conventional MoM and hybrid MoM/PO require the use of 13963 RWG functions

whilst the improved hybrid reduces these functions by 8% to 12848. The number of unknowns is further reduced due to the increase in the largest mesh element. This is not a large reduction in the number of RWG elements, in comparison to the previous example. Nonetheless, this demonstrates that an efficiently generated mesh will use less RWG elements.

Table 5.9: Unknowns and cost for non-uniform mesh with $\lambda/2$ largest triangular edge length mesh

Method	N_{MoM}	N_{PO_1}	N_{PO_2}	Matrix Memory(MB)
MoM	13963	–	–	3.26×10^3
MoM/PO	7108	6855	–	914
Improved MoM/PO	7108	5740	1115	914

5.3.1 Summary

This example demonstrates the ability of the improved hybrid method to solve electrically large problems with small complex detail. It must be noted, however, that the planar surface region that is modelled with the PO can be extended. The extent to which the dimensions of the plate can be increased is dependent on the computational resources available to process the MoM and PO data. In this example, the MoM is large due to the number of edges contained in the cavity. This example can be easily increased to become very large whilst still utilising the efficiency of the improved hybrid technique.

It is also seen that the additional MoM/PO boundary has an adverse effect on the scattered field. This results in incorrect lobing patterns in the scattered field even within the dominant component of the scattered field. Additionally, the effects of the incorrect PO current phase on the normal RWG element is noticeable at grazing incidence.

The improved hybrid does reduce memory requirements considerably. To take advantage of the improved hybrid, the mesh with largest triangular element can be used due to the memory saving of the mesh. However, the accuracy of the desired result must be taken into account when considering this route.

5.4 Dihedral Corner Reflector

The last example considered is the dihedral corner reflector of Figure 5.26. The corner reflector is built up of two square flat plates, each of side length 2.5λ. In this example, coupling effects between the two plates of the dihedral

are investigated. In the previous examples, the PO region was in the shadow of the MoM region and this simplified the coupling calculation of the hybrid method. In this example, however, the PO region is no longer in the shadow of the MoM region. On one side of the dihedral, the MoM region is chosen to be along the edges of the plate while the other plate is modelled with the MoM as illustrated in Figure 5.26.

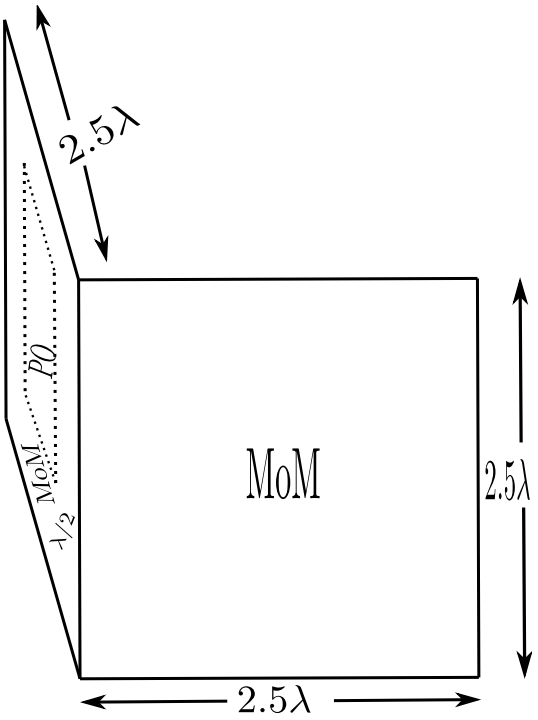

Figure 5.26: $2.5\lambda \times 2.5\lambda \times 2.5\lambda$ Dihedral Corner Reflector

For the sake of simplicity, a uniform mesh with triangular edge length $\lambda/8$ is simulated. This is chosen because the improved hybrid has been proven, in the previous examples, to produce results within the same level of accuracy as the original hybrid for a uniform mesh. In this example, the scattered field from the dihedral corner reflector is calculated.

The simulated dihedral plate is shown in Figure 5.27. It is noted that for the scattered field calculation, monostatic RCS results are obtained for a scan of the incident field from $\theta_0 = 0°$ to $\theta_0 = 90°$. At $\theta_0 = 0°$, the field illuminates the MoM plate of the dihedral and as it is scanned, it illuminates both plates. At $\theta_0 = 90°$, the field illuminates the plate with the MoM/PO region. The MoM region is designated as the $\lambda/2$ away from the edges of the second plate as in Figure 5.26. The PO_1 region is designated to be λ away from the MoM region for the improved hybrid simulation.

The RCS of the dihedral is illustrated in Figure 5.28. This result shows that the forward reflected field in the hybrid techniques is not correct. This

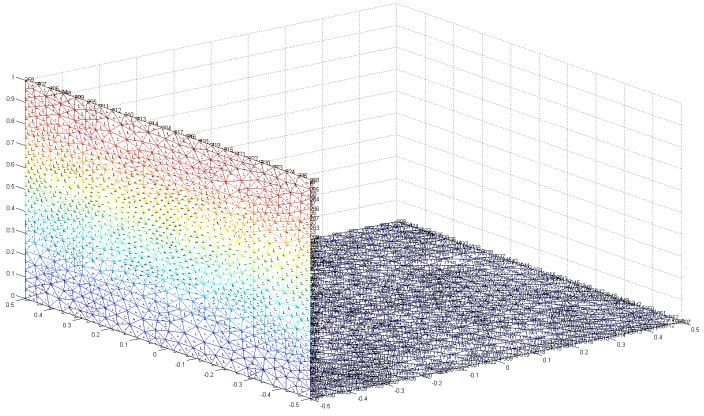

Figure 5.27: Dihedral Corner Reflector with $\lambda/8$ uniform mesh

field returns to the source out of phase due to grazing incidence on the PO portion of the second plate. Between $\theta_0 = 10°$ and $\theta_0 = 80°$, the phase of the current on the PO portion of the hybrid plate is calculated incorrectly. The PO currents are also inaccurate at these angles. The integral of the currents is then underestimated in this region. The effect of the MoM/PO boundary currents are noticeable when the field is incident at normal angles to the MoM/PO plate in the dihedral. In essence, in the coupled region, the integral of the surface current is underestimated due to the phase of the incident field on the PO portion of the hybrid.

Characteristics of the techniques are summarised in Table 5.10. The conventional MoM and hybrid MoM/PO requires the use of 3555 RWG functions whilst the improved hybrid reduces these functions to 3471.

Table 5.10: Unknowns and cost for uniform mesh with $\lambda/8$ triangular edge length

Method	N_{MoM}	N_{PO_1}	N_{PO_2}	Matrix Memory(MB)
MoM	3555	–	–	169
MoM/PO	2905	650	–	135
Improved MoM/PO	2917	554	108	136

5.4.1 Summary

The monostatic scattering results of the improved hybrid MoM/PO agree with those of the main lobe of the reference result. Poor results are observed away from normal incidence because of the inaccurate PO currents and the incorrect

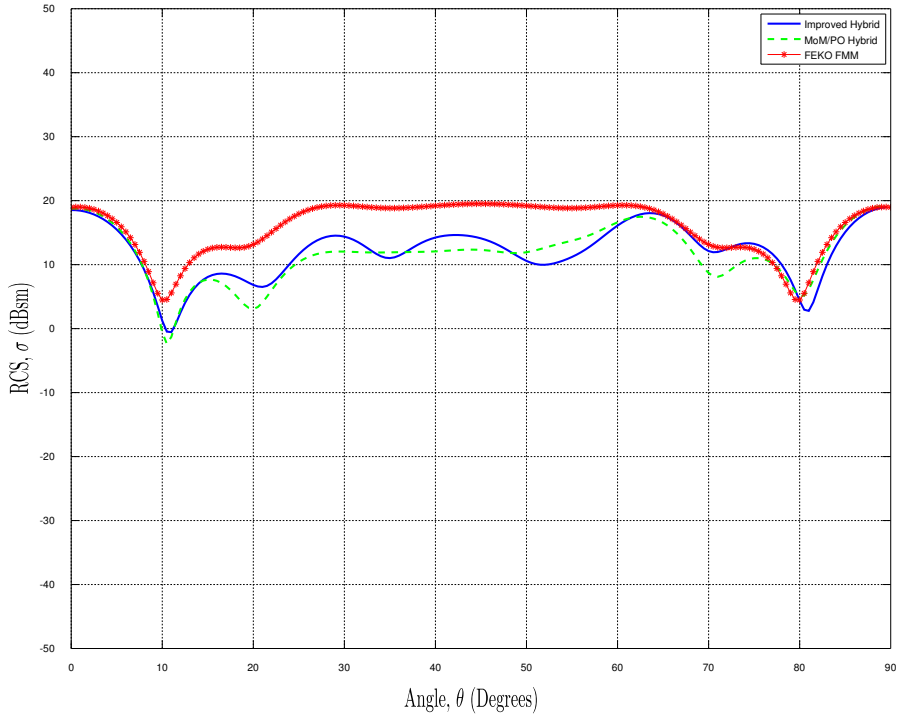

Figure 5.28: Monostatic radar cross section of 2.5λ corner reflector with $\lambda/8$ uniform mesh

phase of the incident wave on the PO plate. This is also compounded by the incorrect PO current approximation at angles away from normal incidence. The coupling effect between the MoM and PO is also visible, compared to the reference solution.

The improved hybrid does reduce computational requirements. This is observed in the reduction of the number of unknowns in the simulation. The corollary of this is the reduction in the matrix storage and improved run time.

5.5 Conclusion

In this chapter, numerical results were presented for the improved hybrid technique developed in this work. The improved hybrid was proven to produce results in agreement with those of the hybrid MoM/PO. The current distribution on the flat plate revealed that the tangential component of current is not continuous across the MoM/PO boundary. Although the hybrid is more efficient than a rigid MoM solution, it does require additional calculations in order to account for the coupling between the MoM and PO regions. The phase of the current was also observed to be incorrect as the size of the mesh

size is increased. This applied to both the normal hybrid and the improved hybrid.

For all the results, a six point Gaussian quadrature scheme was used to approximate the potential integrals on the surface of the mesh elements. At normal incidence, the phase of the incident field is flat and the integration scheme suffices to approximate the surface current. As the geometry is rotated, the phase of the incident field fluctuates and the integration scheme in use is no longer suited to approximating the phase. This requires that either finer mesh elements are used as the geometry is rotated or a more accurate integration scheme is applied.

The flat plate with the cavity was an example of an electrically large problem with electrically small complex detail. This example demonstrated the adverse effects of an additional MoM/PO boundary on the accuracy of the calculated scattered field. This was also compounded by the PO currents that are inaccurate away from normal incidence due to PO assumptions.

The coupling between the PO and MoM region is accounted for by the improved hybrid technique. The accuracy of the coupling term was also affected by the phase of the field incident on the PO region. For the improved hybrid, more accurate integration schemes are required to handle the additional phase term in the RWG function.

To fully realise the power of the improved hybrid, it is important to generate the mesh such that the number of MoM edges are minimised. Nonetheless, in all the examples presented in this section the PO_2 region represents the potential of the improved hybrid to present large savings in computation because it can be increased. When this is the case, however, the accuracy of the solution degrades considerably.

In the following chapter, concluding remarks for this work are presented.

Chapter 6

Conclusion

6.1 Summary of findings

The aim of this work was to develop a technique to obtain a general solution for electrically large problems with complex, electrically small, detail. This was achieved as follows:

- The current based hybrid methods were identified as suitable techniques for the solution of electrically large problems with complex detail in the literature. The current based hybrids take advantage of the benefits offered by the full wave methods whilst utilising the computational efficiency of the asymptotic techniques.
- The MoM and the PO formulation was presented. Both formulations were verified with the calculation of the current density on simple test objects.
- The mathematical formulation behind the MoM/PO hybrid was presented. This hybrid formulation was implemented numerically and verified with a simple flat plate test. The coupling effect of this hybrid was then verified with two flat plates. This hybrid technique was used as a base from which to develop the technique proposed in this work.
- An improved hybrid MoM/PO was developed by extending the current MoM/PO to include a linear phase term to model the surface current on a triangle. This new technique allows the use of a non-uniform surface mesh to model the geometry of interest. This is achieved with a linear phase function to approximate the phase of the current on the non-uniform mesh elements.
- Simulation results were presented to demonstrate the newly developed improved hybrid MoM/PO. These results show the applicability of the improved hybrid technique. Electromagnetic scattering results were calculated from the currents approximated with the improved technique.

These results compared the accuracy and efficiency of the improved hybrid technique to the original MoM/PO hybrid.

6.2 Conclusion

The work focussed on the development of a MoM/PO hybrid technique that allows the use of large mesh elements in the PO region. It was found that:

- The improved hybrid was demonstrated to produce accurate results for the dominant component of the scattered field. The monostatic scattering results obtained with this method demonstrated that the numerical accuracy of the improved hybrid matches that of the original MoM/PO hybrid.
- The integration schemes used in the improved hybrid formulation approximate the phase of the current incorrectly as mesh elements are increased. The phase between two triangular elements is no longer continuous when the mesh element is increased due to the integration scheme used in this work. This effect is worse at grazing incidence.
- The improved hybrid technique allows the use of a non-uniform mesh to model the currents for the problem of interest. This is made possible by the application of linear phase basis functions on the non-uniform elements of the mesh.
- The tangential component of current across the method of moments-physical optics boundary was not continuous. This results in a non-uniform current density across this boundary.
- Both the MoM/PO and improved hybrid techniques require additional calculations for the coupling effect between the MoM and PO region. This results in additional computation time for the calculations presented by the hybrid.
- Care has to be taken in generating a mesh for use with the improved hybrid method. The mesh generation algorithm has to ensure that the number of MoM mesh elements are minimised to take full advantage of the power of the improved hybrid.
- Although good agreement is obtained between the improved hybrid and the MoM for the dominant component of current, this is not true away from grazing angles and especially with increased mesh elements. This is due to the rapid variation of the projected phase of the current on the geometry.

6.3 Summary of contributions

Several contributions were made to the field of current based hybrid techniques. The contributions are listed below:

- An improved current based MoM/PO hybrid was developed. The technique demonstrated that it is possible to obtain first order approximate solutions for electrically large problems with complex detail in an efficient manner using large triangular elements. This improved hybrid method would be suited to Radar detection problems as opposed to tracking and imaging because the resulting solution degrades away from normal incidence.
- The phase of the current is modelled incorrectly for an incident field away from normal incidence. This is a result of the integration schemes used in the present formulation.
- An improvement in the memory utilisation for mesh storage and the MoM matrix is achieved with the use of the improved MoM/PO. This is true as the mesh resolution is decreased. Care should, however, be taken when utilising this improved hybrid because as the mesh resolution is decreased, this is traded off for accuracy.
- The improved hybrid incorporates the linear phase triangular basis functions into the original MoM/PO hybrid computation. This improved hybrid algorithm presents a closed form equation for the solution as opposed to an iterative algorithm.
- The current density on the boundary between the MoM and PO regions adversely affects the accuracy of the improved hybrid.

6.4 Suggestions for future research

In this work, two findings justify further investigation. These are:

- The current magnitude at the MoM-PO boundary. The MoM/PO hybrid technique presented in this study only enforces the normal component of current to be continuous across the MoM-PO boundary. This results in differences in the current density values on opposite sides of the MoM/PO boundary. This warrants a further investigation into the definition of basis functions to smooth the transition of currents on opposite sides of the MoM-PO boundary.
- Singular term integration schemes. The singularity cancellation scheme used in this study is a simple integration schemes used to avoid the source and observation point occurring at the same point. Numerous singularity

handling schemes have been investigated in the literature and use of one these schemes can improve the accuracy of the MoM result.

- Linear phase integration scheme. The linear phase term was integrated using the scheme in the original RWG MoM formulation. An investigation into a better integration scheme for this term is warranted by the effect of the current integration scheme on the phase of the resulting current.

Bibliography

[1] E. F. Knott, "A Progression of High-Frequency RCS Prediction Techniques," *Proceedings of the IEEE*, vol. 73, no. 2, pp. 252–264, 1985.

[2] S. Rao, D. Wilton, and A. Glisson, "Electromagnetic Scattering by Surfaces of Arbitrary Shape," *IEEE Transactions on Antennas and Propagation*, vol. 30, no. 3, pp. 409–418, 1982.

[3] U. Jakobus and F. M. Landstorfer, "Improved PO-MM Hybrid Formulation for Scattering from Three-Dimensional Perfectly Conducting Bodies of Arbitrary Shape," *IEEE Transactions on Antennas and Propagation*, vol. 43, no. 2, pp. 162–169, 1995.

[4] E. F. Knott, J. Shaeffer, and M. Tuley, *Radar Cross Section*, 2nd ed. SciTech, 2004.

[5] D. Jenn, *Radar and Laser Cross Section Engineering*, 2nd ed. AIAA, 2005.

[6] D. Davidson, *Computational Electromagnetics for RF and Microwave Engineering*, 2nd ed. Cambridge University Press, 2011.

[7] E. Miller, L. Medgyesi-Mitschang, and E. H. Newman, *Computational Electromagnetics: Frequency Domain Method of Moments*, L. Shaw, Ed. IEEE Press, 1992.

[8] R. Harrington, "Origin and Development of the Method of Moments for Field Computation," *IEEE Magazine on Antennas and Propagation*, vol. 32, no. 3, pp. 31–35, 1990.

[9] K. Mei and J. Van Bladel, "Scattering by Perfectly-Conducting Rectangular Cylinders," *IEEE Transactions on Antennas and Propagation*, vol. 11, no. 2, pp. 185–192, 1963.

[10] N. Engheta, W. D. Murphy, V. Rokhlin, and M. S. Vassiliou, "The Fast Multipole Method (FMM) for Electromagnetic Scattering Problems," *IEEE Transactions on Antennas and Propagation*, vol. 40, no. 6, pp. 634–641, 1992.

[11] J. Song, C.-C. Lu, and W. C. Chew, "Multilevel Fast Multipole Algorithm for Electromagnetic Scattering by Large Complex Objects," *IEEE Transactions on Antennas and Propagation*, vol. 45, no. 10, pp. 1488–1493, 1997.

[12] A. Manyas, O. Ergul, and L. Gurel, "Hybridizing Physical Optics with MLFMA for Efficient Scattering Computations of Three-Dimensional Complex Targets," in *Proc. Computational Electromagnetics Int. Workshop CEM 2009*, 2009, pp. 69–72.

[13] D. Tonungrueng and E. H. Newman, "The Multiple Sweep Method of Moments (MSMM) Analysis of Electrically Large Bodies," *IEEE Transactions on Antennas and Propagation*, vol. 45, no. 8, pp. 1252–1258, 1997.

[14] D. Colak and E. H. Newman, "The Multiple Sweep Method of Moments (MSMM) Design of Wide-Band Antennas," *IEEE Transactions on Antennas and Propagation*, vol. 46, no. 9, pp. 1365–1371, 1998.

[15] V. Prakash and R. Mittra, "Characteristic Basis Function Method: A New Technique for Efficient Solution of Method of Moments Matrix Equations," *Microwave and Optical Technology Letters*, vol. 36, pp. 95–100, 2003.

[16] G. Tiberi, A. Monorchio, G. Manara, and R. Mittra, "A Spectral Domain Integral Equation Method Utilizing Analytically Derived Characteristic Basis Functions for the Scattering From Large Faceted Objects," *IEEE Transactions on Antennas and Propagation*, vol. 54, no. 9, pp. 2508–2514, 2006.

[17] E. Lucente, G. Tiberi, A. Monorchio, G. Manara, and R. Mittra, "The Characteristic Basis Function Method CBFM: A Numerically Efficient Strategy for Solving Large Electromagnetic Scattering Problems," *Turkish Journal of Electrical Engineering*, vol. 16, pp. 41–56, 2008.

[18] C. Su and T. K. Sarkar, "A Multiscale Moment Method for Solving Fredholm Integral Equation of the First Kind," *Progress in Electromagnetics Research*, vol. 17, pp. 237–264, 1997.

[19] ——, "Electromagnetic Scattering from Coated Strips Utilizing the Adaptive Multiscale Moment Method," *Progress in Electromagnetics Research*, vol. 18, pp. 173–208, 1998.

[20] ——, "Scattering from Perfectly Conducting Strips by Utilizing an Adaptive Multiscale Moment Method," *Progress in Electromagnetics Research*, vol. 19, pp. 173–197, 1998.

[21] ——, "Adaptive Multiscale Moment Method (AMMM) for Analysis of Scattering from Perfectly Conducting Plates," *IEEE Transactions on Antennas and Propagation*, vol. 48, no. 6, pp. 932–939, 2000.

[22] ——, "Adaptive Multiscale Moment Method (AMMM) for Analysis of Scattering from Three-Dimensional Perfectly Conducting Structures," *IEEE Transactions on Antennas and Propagation*, vol. 50, no. 4, pp. 444–450, 2002.

[23] E. Bleszynski, M. Bleszynski, and T. Jaroszewics, "AIM: Adaptive Integral Method for Solving Large-Scale Electromagnetic Scattering and Radiation Problems," *Radio Science*, vol. 31, pp. 1225–1251, 1996.

[24] L.-W. Li, W.-B. Ewe, and C.-S. Chang, "Adaptive Integral Method for Electromagnetic Scattering and Antenna Radiation," in *Proc. Asia-Pacific Conf. Applied Electromagnetics APACE 2005*, 2005, pp. 1–7.

[25] O. S. Kim and P. Meincke, "Adaptive integral method for Higher-Order Hierarchical Method of Moments," in *Proc. First European Conf. Antennas and Propagation EuCAP 2006*, 2006, pp. 1–4.

[26] ——, "Adaptive Integral Method for Higher Order Method of Moments," *IEEE Transactions on Antennas and Propagation*, vol. 56, no. 8, pp. 2298–2305, 2008.

[27] C. C. Ioannidi and H. T. Anastassiu, "Circulant Adaptive Integral Method (CAIM) for Electromagnetic Scattering From Large Targets of Arbitrary Shape," *IEEE Transactions on Magnetics*, vol. 45, no. 3, pp. 1308–1311, 2009.

[28] M.-F. Wu, G. Kaur, and A. E. Yilmaz, "A Multiple-Grid Adaptive Integral Method for Multi-Region Problems," *IEEE Transactions on Antennas and Propagation*, vol. 58, no. 5, pp. 1601–1613, 2010.

[29] C. Brennan, P. Cullen, and M. Condon, "A Novel Iterative Solution of the Three Dimensional Electric Field Integral equation," *IEEE Transactions on Antennas and Propagation*, vol. 52, no. 10, pp. 2781–2785, 2004.

[30] W.-D. Li, W. Hong, and H.-X. Zhou, "Integral Equation Based Overlapped Domain Decomposition Method for the Analysis of Electromagnetic Scattering of 3D Conducting Objects," *Microwave and Optical Technology Letters*, vol. 49, pp. 265–274, 2007.

[31] ——, "An IE-ODDM-MLFMA Scheme With DILU Preconditioner for Analysis of Electromagnetic Scattering From Large Complex Objects,"

IEEE Transactions on Antennas and Propagation, vol. 56, no. 5, pp. 1368–1380, 2008.

[32] E. Garcia, C. Delgado, I. G. Diego, and M. F. Catedra, "An Iterative Solution for Electrically Large Problems Combining the Characteristic Basis Function Method and the Multilevel Fast Multipole Algorithm," *IEEE Transactions on Antennas and Propagation*, vol. 56, no. 8, pp. 2363–2371, 2008.

[33] K. Umashankar, S. Nimmagadda, and A. Taflove, "Application of Integral Equation and Method of Moments for Electrically Very Large Scatterers Using Spatial Decomposition Technique," in *Proc. AP-S Antennas and Propagation Society Int. Symp. Merging Technologies for the 90's. Digest*, 1990, pp. 76–79.

[34] B. D. Braaten, R. M. Nelson, and M. A. Mohammed, "Electric Field Integral Equations for Electromagnetic Scattering Problems With Electrically Small and Electrically Large Regions," *IEEE Transactions on Antennas and Propagation*, vol. 56, no. 1, pp. 142–150, 2008.

[35] M. Lashab, C. Zebiri, and F. Benabdelaziz, "Wavelet-Based Moment Method and Physical Optics Use on Large Reflector Antennas," *Progress in Electromagnetics Research*, vol. 2, pp. 189–200, 2008.

[36] E. Jorgensen, J. L. Volakis, P. Meincke, and O. Breinbjerg, "Higher Order Hierarchical Legendre Basis Functions for Electromagnetic Modeling," *IEEE Transactions on Antennas and Propagation*, vol. 52, no. 11, pp. 2985–2995, 2004.

[37] L. Sun, J. P. Webb, and W. Hong, "Edge Elements and The Decomposition Projective Method to Solve Scattering Problems of Electrically Large Objects," in *Proc. 14th Biennial IEEE Conf. Electromagnetic Field Computation (CEFC)*, 2010, p. 1.

[38] D. P. Bouche, F. A. Molinet, and R. Mittra, "Asymptotic and Hybrid Techniques for Electromagnetic Scattering," *Proceedings of the IEEE*, vol. 81, no. 12, pp. 1658–1684, 1993.

[39] R. G. Kouyoumjian, "Asymptotic High-Frequency Methods," *Proceedings of the IEEE*, vol. 53, no. 8, pp. 864–876, 1965.

[40] J. Keller, "Geometrical Theory of Diffraction," *Journal of the Optical Society of America*, vol. 52, pp. 116–130, 1962.

[41] P. Ufimtsev, "Method of Edge Waves in the Physical Theory of Diffraction," 1971, translation prepared by the U.S. Air Force Foreign Technology Division.

[42] P. Pathak, "High Frequency Techniques for Antenna Analysis," *Proceedings of the IEEE*, vol. 80, no. 1, pp. 44–65, 1992.

[43] P. Y. Ufimtsev, "Improved Physical Theory of Diffraction: Removal of the Grazing Singularity," *IEEE Transactions on Antennas and Propagation*, vol. 54, no. 10, pp. 2698–2702, 2006.

[44] H. Ling, S.-W. Lee, and R.-C. Chou, "High-frequency RCS of open cavities with rectangular and circular cross sections," *IEEE Transactions on Antennas and Propagation*, vol. 37, no. 5, pp. 648–654, 1989.

[45] H. Ling, R.-C. Chou, and S.-W. Lee, "Shooting and bouncing rays: calculating the RCS of an arbitrarily shaped cavity," *IEEE Transactions on Antennas and Propagation*, vol. 37, no. 2, pp. 194–205, 1989.

[46] R. Mittra, Y. Rahmat-Samii, and W. Ko, "Spectral Theory of Diffraction," *Applied Physics A: Materials science and processing*, vol. 10, pp. 1–13, 1976.

[47] Y. Rahmat-Samii and R. Mittra, "A Spectral Domain Interpretation of High Frequency Diffraction Phenomena," *IEEE Transactions on Antennas and Propagation*, vol. 25, no. 5, pp. 676–687, 1977.

[48] G. A. Thiele, "Overview of Selected Hybrid Methods in Radiating System Analysis," *Proceedings of the IEEE*, vol. 80, no. 1, pp. 66–78, 1992.

[49] L. N. Medgyesi-Mitschang and D.-S. Wang, "Hybrid Methods for Analysis of Complex Scatterers," *Proceedings of the IEEE*, vol. 77, no. 5, pp. 770–779, 1989.

[50] L. Medgyesi-Mitschang and D.-S. Wang, "Hybrid Solutions for Scattering from Perfectly Conducting Bodies Of Revolution," *IEEE Transactions on Antennas and Propagation*, vol. 31, no. 4, pp. 570–583, 1983.

[51] ——, "Hybrid Solutions for Scattering from Large Bodies Of Revolution with Material Discontinuities and Coatings," *IEEE Transactions on Antennas and Propagation*, vol. 32, no. 7, pp. 717–723, 1984.

[52] Z. Shen and J. L. Volakis, "A Hybrid Physical Optics-Moment Method for Large Nose Radome Antennas," in *Proc. IEEE Antennas and Propagation Society Int. Symp*, vol. 4, 1999, pp. 2554–2557.

[53] C. S. Kim and Y. Rahmat-Samii, "Low Profile Antenna Study Using the Physical Optics Hybrid Method (POHM)," in *Proc. AP-S Antennas and Propagation Society Int. Symp. Digest*, 1991, pp. 1350–1353.

[54] F. Obelleiro, J. Taboada, J. Rodriguez, J. Rubinos, and A. Arias, "Hybrid Moment-Method Physical-Optics Formulation for Modeling the Electromagnetic Behavior of On-Board Antennas," *Microwave and Optical Technology Letters*, vol. 27, pp. 88–93, 2000.

[55] A. Noga and A. Karwowski, "Analysis of Electrically Large Problems Using the Hybrid MM-PO Method," in *Proc. 17th Int. Conf. Microwaves, Radar and Wireless Communications MIKON 2008*, 2008, pp. 1–4.

[56] L. Medgyesi-Mitschang and J. Putnam, "Hybrid Formulation for Arbitrary 3-D Bodies," in *Annual Review of Progress in Computational Electromagnetics*, vol. 2. ACES, 1994, pp. 267–274.

[57] U. Jakobus and F. J. C. Meyer, "A Hybrid Physical Optics/Method of Moments Numerical Technique: Theory, Investigation and Application," in *Proc. IEEE AFRICON 4th AFRICON*, vol. 1, 1996, pp. 282–287.

[58] H. J. Bilow, "Scattering by an Infinite Wedge with Tensor Impedance Boundary Conditions-A Moment Method/Physical Optics Solution for the Currents," *IEEE Transactions on Antennas and Propagation*, vol. 39, no. 6, pp. 767–773, 1991.

[59] Z. Gong, B. Xiao, G. Zhu, and H. Ke, "Improvements to the Hybrid MoM-PO Technique for Scattering of Plane Wave by an Infinite Wedge," *IEEE Transactions on Antennas and Propagation*, vol. 54, no. 1, pp. 251–255, 2006.

[60] D.-S. Wang, "Current-Based Hybrid Analysis for Surface-Wave Effects on Large Scatterers," *IEEE Transactions on Antennas and Propagation*, vol. 39, no. 6, pp. 839–850, 1991.

[61] U. Jakobus and F. M. Landstorfer, "Application of Fock Currents for Curved Convex Surfaces Within the Framework of a Current-Based Hybrid Method," in *Proc. Third Int Computation in Electromagnetics Conf. (Conf. Publ. No. 420)*, 1996, pp. 415–420.

[62] ——, "A Combination of Current and Ray-Based Techniques for the Efficient Analysis of Electrically Large Scattering Problems," in *13th Annual Review of Progress in Applied Computational Electromagnetics*, vol. 1. ACES, 1997, pp. 748–755.

[63] J. Taboada, F. Obelleiro, and J. Rodriguez, "Improvement of the hybrid Moment-Method Physical-Optics Method through a Novel Evaluation of the Physical Optics Operator," *Microwave and Optical Technology Letters*, vol. 30, pp. 357–363, 2001.

[64] H.-D. Bruns, M. Sabielny, D. Leugner, and H. Singer, "Application and Limits of the MoM-PO-UTD Hybridization Technique," in *Proc. Int.Symp. Electromagnetic Compatibility EMC 2004*, vol. 2, 2004, pp. 672–677.

[65] B. M. Notaros, "Higher Order Frequency-Domain Computational Electromagnetics," *IEEE Transactions on Antennas and Propagation*, vol. 56, no. 8, pp. 2251–2276, 2008.

[66] E. Jorgensen, P. Meincke, and O. Breinbjerg, "A Hybrid PO-Higher-Order Hierarchical MoM Formulation Using Ccurvilinear Geometry Modeling," in *Proc. IEEE Antennas and Propagation Society Int. Symp*, vol. 4, 2003, pp. 98–101.

[67] M. Djordjevic and B. M. Notaros, "Higher Order Hybrid Method of Moments-Physical Optics Modeling Technique for Radiation and Scattering from Large Perfectly Conducting Surfaces," *IEEE Transactions on Antennas and Propagation*, vol. 53, no. 2, pp. 800–813, 2005.

[68] B. M. Notaros and M. Djordjevic, "Hybrid Numerical-Asymptotic Modeling of Electrically Large EM Structures," in *22nd Annual Review of Progress in Applied Computational Electromagnetics*, 2006, pp. 150–153.

[69] A. Noga and A. Karwowski, "Wide-Band Hybrid MM-PO Computational Electromagnetics Technique Using [Z] Matrix Interpolation and Adaptive Frequency Sampling," in *Proc. IEEE Int. Symp. Electromagnetic Compatibility EMC 2007*, 2007, pp. 1–4.

[70] X. An and Z.-Q. Lu, "An Integral Equation Fast-Fourier Transform-Based Hybrid Method for Analysis of Wire-Surface Configurations on Electrically Large Platforms," *Microwave and Optical Technology Letters*, vol. 51, pp. 486–490, 2009.

[71] W. Wang and J. Xunew, "Analyzing Wide-band Behavior of Wire Antennas on Large Platforms with Fast PO-MoM Techniques," in *Proc. Asia-Pacific Microwave Proceedings APMC 2005*, vol. 3, 2005.

[72] E. H. Newman, "An Overview of the Hybrid MM/Green's Function Method in Electromagnetics," *Proceedings of the IEEE*, vol. 76, no. 3, pp. 270–282, 1988.

[73] Y. Shifman and Y. Leviatan, "Scattering by a Groove in a Conducting Plane-a PO-MoM Hybrid Formulation and Wavelet Analysis," *IEEE Transactions on Antennas and Propagation*, vol. 49, no. 12, pp. 1807–1811, 2001.

[74] T. Kim and G. Thiele, "A Hybrid Diffraction Technique–General Theory and Applications," *IEEE Transactions on Antennas and Propagation*, vol. 30, no. 5, pp. 888–897, 1982.

[75] M. Kaye, P. Murthy, and G. Thiele, "An Iterative Method for Solving Scattering Problems," *IEEE Transactions on Antennas and Propagation*, vol. 33, no. 11, pp. 1272–1279, 1985.

[76] R. E. Hodges and Y. Rahmat-Samii, "An Iterative Current-Based Hybrid Method for Complex Structures," *IEEE Transactions on Antennas and Propagation*, vol. 45, no. 2, pp. 265–276, 1997.

[77] B. Andres-Garcia, D. Gonzalez-Ovejero, C. Craeye, L. E. Garcia-Munoz, and D. Segovia-Vargas, "An Iterative MoM-PO Method Based on a MBF/Krylov Approach," in *Proc. Fourth European Conf. Antennas and Propagation (EuCAP)*, 2010, pp. 1–4.

[78] J. Edlund, "A Parallel, Iterative Method of Moments and Physical Optics Hybrid Solver for Arbitrary Surfaces," Uppsala University, Tech. Rep., 2001.

[79] H. Zhai and C. Liang, "A Simple Iterative Method for Considering Multibounce in PO region of MoM," *Microwave and Optical Technology Letters*, vol. 40, pp. 10–112, 2004.

[80] A. Sullivan and L. Carin, "Scattering from Complex Bodies Using a Combined Direct and Iterative Technique," *IEEE Transactions on Antennas and Propagation*, vol. 47, no. 1, pp. 33–39, 1999.

[81] D.-H. Han, A. C. Polycarpou, and C. A. Balanis, "Hybrid Analysis of Reflector Antennas Including Higher Order Interactions and Blockage Effects," *IEEE Transactions on Antennas and Propagation*, vol. 50, no. 11, pp. 1514–1524, 2002.

[82] P. Murthy, K. Hill, and G. Thiele, "A Hybrid-Iterative Method for Scattering Problems," *IEEE Transactions on Antennas and Propagation*, vol. 34, no. 10, pp. 1173–1180, 1986.

[83] L. Medgyesi-Mitschang and D.-S. Wang, "Hybrid Methods in Computational Electromagnetics: A Review," *Computer Physics Communication*, vol. 68, pp. 76–94, 1991.

[84] G. Thiele and T. Newhouse, "A Hybrid Technique for Combining Moment Methods with the Geometrical Theory of Diffraction," *IEEE Transactions on Antennas and Propagation*, vol. 23, no. 1, pp. 62–69, 1975.

[85] E. Newman and D. Pozar, "Electromagnetic Modeling of Composite Wire and Surface Geometries," *IEEE Transactions on Antennas and Propagation*, vol. 26, no. 6, pp. 784–789, 1978.

[86] ——, "Correction to "Electromagnetic Modeling of Composite Wire and Surface Geometries"," *IEEE Transactions on Antennas and Propagation*, vol. 27, no. 4, 1979.

[87] L. Medgyesi-Mitschang and J. Putnam, "Formulation for Wire Radiators on Bodies of Translation With and Without End Caps," *IEEE Transactions on Antennas and Propagation*, vol. 31, no. 6, pp. 853–862, 1983.

[88] W. Burnside, C. Yu, and R. Marhefka, "A Technique to Combine the Geometrical Theory of Diffraction and the Moment Method," *IEEE Transactions on Antennas and Propagation*, vol. 23, no. 4, pp. 551–558, 1975.

[89] J. Sahalos and G. Thiele, "On the Application of the GTD-MM Technique and Its Limitations," *IEEE Transactions on Antennas and Propagation*, vol. 29, no. 5, pp. 780–786, 1981.

[90] S. Hagdahl, "Hybrid Methods for Computational Electromagnetics in Frequency Domain," Ph.D. dissertation, KTH, 2005.

[91] F. Weinmann, "Ray Tracing with PO/PTD for RCS Modeling of Large Complex Objects," *IEEE Transactions on Antennas and Propagation*, vol. 54, no. 6, pp. 1797–1806, 2006.

[92] J. Lanoe, M. Ney, and S. Le Maguer, "Time-Domain Equivalent Edge Current (TED-EECs) Technique to Improve a TLM-Physical Optics Hybrid Procedure," in *2nd European Conference on Antennas and Propagation*, 2007, pp. 1–5.

[93] B. Usner, "Generalized Hybrid Methods for Modeling Complex Electromagnetic Structures," Ph.D. dissertation, Ohio State University, 2005.

[94] Z. Xie, O. Hassan, and K. Morgan, "A Parallel Implicit/Explicit Hybrid Time Domain Method for Computational Electromagnetics," *International Journal for Numerical Methods in Engineering*, vol. 80, pp. 1093–1109, 2009, available http://www.interscience.wiley.com.

[95] Z. Altman and R. Mittra, "A Technique for Extrapolating Numerically Rigorous Solutions of Electromagnetic Scattering Problems to Higher Frequencies and their Scaling Properties," *IEEE Transactions on Antennas and Propagation*, vol. 47, no. 4, pp. 744–751, 1999.

[96] S. Sefi and F. Bergholm, "Extrapolation and Modeling of Method of Moments Currents on a PEC Surface," in *Int. Conf. on Mathematical Modeling of Wave Phenomena*, 2005, pp. 1–25.

[97] D.-H. Kwon, R. J. Burkholder, and P. H. Pathak, "Efficient Method of Moments Formulation for Large PEC Scattering Problems Using Asymptotic Phasefront Extraction (APE)," *IEEE Transactions on Antennas and Propagation*, vol. 49, no. 4, pp. 583–591, 2001.

[98] M. F. Catedra, C. Delgado, S. Luceri, O. G. Blanco, and F. S. de Adana, "Physical Optics Analysis of Multiple Interactions in Large Scatters Using Current Modes," *IEEE Transactions on Antennas and Propagation*, vol. 54, no. 3, pp. 985–994, 2006.

[99] M. Skolnik, *Radar Handbook*. McGraw-Hill, 2007.

[100] R. E. Hodges and Y. Rahmat-Samii, "The Evaluation of MFIE Integrals With the Use of Vector Triangle Basis Functions," *MIcrowave and Optical Technology Letters*, vol. 14, pp. 9–14, 1997.

[101] D. Dunavant, "High Degree Efficient Symmetrical Gaussian Quadrature Rules for the Triangle," *International Journal for Numerical Methods in Engineering*, vol. 21, pp. 1129–1148, 1985.

[102] J. Taboada, F. Obelleiro, J. Rodriguez, I. Garcia-Tunon, and L. Landesa, "Incorporation of Linear-Phase Progression in RWG Basis Functions," *Microwave and Optical Technology Letters*, vol. 44, pp. 106–112, 2005.